Search for Lightly Ionizing Particles in SuperCDMS and simulation of neutron backgrounds

By

SAMIR BANIK

PHYS11201504016

National Institute of Science Education and Research, Bhubaneswar

A thesis submitted
to the Board of Studies in
School of Physical Sciences

In partial fulfillment of requirements
For the Degree of

DOCTOR OF PHILOSOPHY

of

HOMI BHABHA NATIONAL INSTITUTE

October 07, 2021

Homi Bhabha National Institute

Recommendations of the Viva Voce Committee

As members of the Viva-Voce Committee, we certify that we have read the dissertation prepared by **Samir Banik** entitled **"Search for Lightly Ionizing Particles in SuperCDMS and simulation of neutron backgrounds"** and recommend that it may be accepted as fulfilling the thesis requirement for the award of Degree of Doctor of Philosophy.

Chairman - Prof. Sanjay Kumar Swain		**Date:** 7/10/2021
Guide / Convener - Prof. Bedangadas Mohanty		**Date:** 07/10/2021
Member 1 - Dr. Kartikeshwar Senapati		**Date:** 07/10/2021
Member 2 - Dr. Nishikanta Khandai		**Date:** 07/10/2021
Member 3 - Dr. Seema Bahinipati	Seema Bahinipati	**Date:**
External examiner - Prof. Jim Libby		**Date:** 7/10/2021

Final approval and acceptance of this thesis is contingent upon the candidate's submission of the final copies of the thesis to HBNI.

I/We hereby certify that I/We have read this thesis prepared under my/our direction and recommend that it may be accepted as fulfilling the thesis requirement.

Date : October 07, 2021
Place : Jatni

(Guide) 07/10/2021

STATEMENT BY THE AUTHOR

This dissertation has been submitted in partial fulfillment of requirements for an advanced degree at Homi Bhabha National Institute (HBNI) and is deposited in the library to be made available to borrowers under rules of the HBNI.

Brief quotations from this dissertation are allowable without special permission, provided that accurate acknowledgement of source is made. Requests for permission for extended quotation from or reproduction of this manuscript in whole or in part may be granted by the Competent Authority of HBNI when in his or her judgment the proposed use of the material is in the interests of scholarship. In all other instances, however, permission must be obtained from the author.

Date : October 07, 2021

Place : Jatni

(SAMIR BANIK)

DECLARATION

I hereby declare that the investigation presented in the thesis has been carried out by me. The work is original and has not been submitted earlier as a whole or in part for a degree/diploma at this or any other Institution/University.

Date : October 07, 2021

Place : Jatni

(SAMIR BANIK)

List of Publications arising from the thesis

Journal

Published

[1] S. Banik, V.K.S. Kashyap, M.H. Kelsey, et al. "Simulation of energy loss of fractionally charged particles using Geant4". *Nuclear Instruments and Methods in Physics Research Section A: Accelerators, Spectrometers, Detectors and Associated Equipment* 971 (2020), 164114.

[2] S. Banik, V. K. S. Kashyap, S. Ghosh, et al. "Simulation of neutron background for a dark matter search experiment at JUSL". *JINST* 16.06 (2021), P06022.

[3] I. Alkhatib, D. W. P. Amaral, T. Aralis, et al. "Constraints on Lightly Ionizing Particles from CDMSlite". *Phys. Rev. Lett.* 127 (8 2021), 081802.

Conferences

[1] S. Banik (for SuperCDMS collaboration). "Simulation of energy deposition of Lightly Ionizing Particles in GEANT4". *62nd DAE-BRNS Symposium on Nuclear Physics*. Vol. 62. 2017, 732–734.

[2] S. Banik (for SuperCDMS collaboration). "Search for fractionally-charged particles with CDMSlite". *New Perspectives 2020 (2.0)*. 2020.

[3] S. Banik, V. K. S. Kashyap, and B. Mohanty. "Simulation of cosmogenic neutron backgrounds for a dark matter search experiment at Jaduguda Underground Science Laboratory". *XXIV DAE-BRNS High Energy Physics Symposium*. 2020.

Other publications

[1] I. Alkhatib, D.W.P. Amaral, T. Aralis, et al. "Light Dark Matter Search with a High-Resolution Athermal Phonon Detector Operated Above Ground" (July 2020). arXiv: 2007.14289 [hep-ex].

[2] D. W. Amaral, T. Aralis, T. Aramaki, et al. "Constraints on low-mass, relic dark matter candidates from a surface-operated SuperCDMS single-charge sensitive detector". *Phys. Rev. D* 102 (9 2020), 091101.

[3] T. Aralis, T. Aramaki, I. J. Arnquist, et al. "Constraints on dark photons and axionlike particles from the SuperCDMS Soudan experiment". *Phys. Rev. D* 101 (5 2020). [Erratum: Phys.Rev.D 103, 039901 (2021)], 052008.

[4] R. Agnese, T. Aralis, T. Aramaki, et al. "Search for low-mass dark matter with CDMSlite using a profile likelihood fit". *Phys. Rev. D* 99 (6 2019), 062001.

[5] R. Agnese, T. Aralis, T. Aramaki, et al. "Production rate measurement of Tritium and other cosmogenic isotopes in Germanium with CDMSlite". *Astroparticle Physics* 104 (2019), 1–12.

[6] R. Agnese, T. Aralis, T. Aramaki, et al. "Energy loss due to defect formation from 206Pb recoils in SuperCDMS germanium detectors". *Applied Physics Letters* 113.9 (2018), 092101. eprint: https://doi.org/10.1063/1.5041457.

[7] R. Agnese, T. Aralis, T. Aramaki, et al. "First Dark Matter Constraints from a SuperCDMS Single-Charge Sensitive Detector". *Phys. Rev. Lett.* 121 (5 2018). [Erratum: Phys.Rev.Lett. 122, 069901 (2019)], 051301.

[8] R. Agnese, A.J. Anderson, T. Aramaki, et al. "Nuclear-recoil energy scale in CDMS II silicon dark-matter detectors". *Nuclear Instruments and Methods in Physics Research Section A: Accelerators, Spectrometers, Detectors and Associated Equipment* 905 (2018), 71–81.

[9] R. Agnese, T. Aramaki, I. J. Arnquist, et al. "Results from the Super Cryogenic Dark Matter Search Experiment at Soudan". *Phys. Rev. Lett.* 120 (6 2018), 061802.

Date : October 07, 2021

Place : Jatni

(SAMIR BANIK)

DEDICATED TO

my family and friends

ACKNOWLEDGEMENTS

I am thankful to many people for their support and guidance in completing this dissertation. I would like to thank my supervisor, Prof. Bedangadas Mohanty for providing me with the opportunity to work with his HEP group. His guidance throughout the Ph.D. period shaped the work presented in this thesis, and his moral support was instrumental in keeping me focused on my work. His dedication to science is always inspiring.

I am also thankful to the members of the NISER HEP group. I would like to express my gratitude to Dr. Varchaswi K. S. Kashyap for his help in almost all academic problems that I faced. I owe him a lot for all the programming skills and scientific knowledge I acquired while working with him. I am particularly indebted to Dr. Kashyap and Dr. Meghna K. K. for introducing me to the scientific tool of simulations. I also would like to thank Dr. Chitrasen Jena, Dr. Ranbir Singh, and Dr. Ajay Kumar Dash as I learnt many aspects of data analysis from them. It was a delight to have Debasish, Sourav, Vijay, Ashutosh, Dukhishyam, Ashish, Prottay, Swati and Mouli as my friends and colleagues. I have learnt a lot from all of you.

I am thankful to my doctoral committee members Dr. Sanjay Kumar Swain, Dr. Kartikeshwar Senapati, Dr. Nishikanta Khandai, and Dr. Seema Bahinipati. Their valuable feedback during annual evaluations of the Ph.D. program has improved my understanding of physics.

I would like to thank members of the SuperCDMS collaboration for the many discussions we have had during the course of the analysis. I am grateful to Rupak Mahapatra, Joel Sander, Amy Roberts, Priscilla Cushman, Belina von Krosigk, Patrick T Lukens, Matthew Fritts, Ruslan Podviianiuk, and Sudip Poudel for their valuable feedback on the work presented in this dissertation. I would like to express my sincere thanks to Dennis Wright and

Mike Kelsey for providing insightful comments in developing a simulation framework for fractionally charged particles. The simulation framework is a significant component of the dissertation.

I am thankful to all my teachers, since my childhood, who have encouraged me to continue in academia. I am thankful to my parents for everything that I am today. Their love and support always push me to be a better person. I am thankful to my late brother, Sanjeeb, for being there for me.

ABSTRACT

The Super Cryogenic Dark Matter Search (SuperCDMS) is a direct-detection dark matter search experiment that primarily aims to search for Weakly Interacting Massive Particles (WIMPs) using state-of-the-art solid-state detection technology. During its operation at the Soudan underground laboratory, germanium detectors were operated with a high bias voltage mode known as the CDMS low ionization threshold experiment (CDMSlite) to achieve below-keV thresholds. CDMSlite, for being able to measure small energy depositions in detectors, also provides sensitivity to Lightly Ionizing Particles (LIPs) with very small fractional charges. This thesis will discuss an analysis to search LIPs with the data acquired in CDMSlite mode. An important component for LIPs search is the expected energy-deposition distributions for LIPs falling on the CDMSlite detector. In this thesis, a simulation framework to calculate the energy-deposition distributions is developed. This thesis presents first direct-detection limits on the intensity of cosmogenic LIPs with electric charges smaller than $e/(3 \times 10^5)$ as well as the strongest limits for charges $\leq e/160$, with a minimum intensity of $1.36 \times 10^{-7}\,\mathrm{cm^{-2}s^{-1}sr^{-1}}$ at charge $e/160$.

In any rare-event search experiment, understanding background is crucial. Neutrons capable of mimicking dark matter signals are a major background for any dark matter search experiment. A simulation study to estimate the neutron background for an India-based dark matter search experiment at Jaduguda Underground Science Laboratory (JUSL) is performed. The experiment at JUSL will be the first phase of a proposed Dark matter search at India-based Neutrino Observatory (DINO). It will be a direct detection experiment with primary aims to search for WIMPs as dark matter candidates. In this thesis, we discuss the methodology of estimating neutron flux at JUSL and report the results. The total neutron flux reaching the laboratory above 1 MeV energy threshold is found to be

$5.76(\pm 0.69) \times 10^{-6}\,\mathrm{cm}^{-2}\mathrm{s}^{-1}$. The impact of neutron background on the sensitivity of the experiment to detect dark matter at JUSL is also discussed.

The thesis is organized as follows. Chapter 1 provides a brief introduction to the Lightly Ionizing Particle (LIPs). The analysis to search LIPs in SuperCDMS is briefly outlined in the chapter. This chapter also discusses the importance of neutron background estimates in a dark matter search experiment, more specifically, in the context of a proposed India-based dark matter search experiment at Jaduguda Underground Science Laboratory. In Chapter 2, the SuperCDMS experiment is introduced. In Chapter 3, the framework developed to perform simulations for Lightly Ionizing Particles is presented. In Chapter 4, the LIPs search analysis with the CDMSlite data and the results are discussed. In Chapter 5, the simulation of neutron background and the feasibility of dark-matter search at JUSL is discussed. Finally, conclusions from all the results discussed in this thesis are presented in Chapter 6.

Contents

List of Figures

List of Tables

Chapter 1

Introduction

There are several intriguing open ended questions in physics. Among them are the identity of dark matter (DM), and the possibility of freely existing fractionally charged particles (FCPs) in the universe. There are various experiments set up around the world to search and understand these exotic particles. The direct detection experiments for these particles are built on the principle of measuring the energy deposited by these particles in a target material. These particles are elusive to direct detection experiments due to their low interaction cross section with the target material [1]. The radioactive and cosmogenic backgrounds from various sources, like the uranium and thorium decay chains, cosmic rays and their secondaries like neutrons, add to the difficulty of identifying the weak signals from DM or FCPs over the aforementioned backgrounds. The combination of low interaction cross section of these particles with the detector material, and presence of other backgrounds make detecting these events rare. A thorough understanding of the backgrounds, and the detector response to the low energy depositions from exotic particles, are essential in these rare event searches. This thesis discusses two major topics related to rare event searches: a) FCP search in Super Cryogenic Dark Matter Search (SuperCDMS)

experiment, and b) an estimation of neutron backgrounds for a proposed dark matter search experiment at Jaduguda Underground Science Laboratory (JUSL).

The charged particles discovered to date are seen to carry charges that are integer multiples of $e/3$ (d-quark charge), and in the case of unconfined particles, the charge is integer multiples of the charge of an electron. While quantization of particle-charge does not naturally follow from the Quantum theory of Electrodynamics (QED), numerous theoretical models [2–12] allow the existence of particles with fractional electric charges.

There are a variety techniques to search for FCP productions in fixed-target accelerators [13–19], in colliders [20–27], in reactor-based experiments [28–30]. There are also several experiments searching for cosmogenic FCPs in direct-detection experiments [31–37] and in bulk-matter [38–47]. These experiments have put constraints on mass vs. charge or intensity vs. charge parameter space. Astrophysical and cosmological considerations also put constraints on the parameter space of FCPs [48]. Figure 1.1 in Section 1.4 shows constraints from various laboratory experiments, astrophysical and cosmological observations. However, it can be seen that a large region of the parameter space is yet to be explored and there is scope for improvement on the current limits. FCPs have charge $q = \pm fe$, where e is the charge of an electron, and f is a fractional number less than one. Since the mean energy loss per unit length or the stopping power goes as q^2, free FCPs with small electric charge are also called Lightly Ionizing Particles (LIPs). For the rest of this chapter, FCP and LIP are used interchangeably.

SuperCDMS is a direct-detection experiment (discussed in Chapter 2) that primarily searches for Weakly Interacting Massive Particles (WIMPs) as dark matter candidates. It is an underground experiment located in the Soudan mine of Minnesota, USA. The experiment used solid-state germanium detectors in a high bias-voltage mode known as CDMS low ionization threshold experiment (CDMSlite) [49] where sensitivity to measure

sub-keV energy depositions expected from small-charged LIPs is achieved. This thesis presents an analysis to search cosmogenically produced LIPs in the data acquired with CDMSlite mode. The data from the first period (February through July 2014) of the second CDMSlite run [49] is used. In the analysis presented in this thesis, upper limits on the intensity of LIPs are calculated for the events observed in the data spectrum. The limits are calculated for various charges between $e/100$ and $e/10^8$, masses between $5\,\mathrm{MeV}/c^2$ and $100\,\mathrm{TeV}/c^2$, and incident $\beta\gamma$[1] values between 0.1 and 10^6 [50].

One major component of the intensity limit calculation is the expected distribution of energy deposition of the incoming LIPs. A framework within the GEANT4 [51] simulation setup is developed (decribed in Chapter 3) to calculate the energy deposition of LIPs in typical detector materials [52]. GEANT4 is a Monte Carlo simulation toolkit widely used in many experiments starting from low energy nuclear physics to high energy particle physics experiments. The toolkit traditionally does not come with definitions for fractionally charged particles. The framework developed for LIPs in this thesis includes: a) definitions for positively and negatively charged LIPs, and b) a "physics list" where the physics processes for LIPs are specified. They are the two pivotal components to perform simulations for LIPs with GEANT4 under any experimental arrangements of detectors and shieldings. It is used to calculate the probability distribution of energy depositions for LIP interactions with the CDMSlite detector and also to calculate corrections to some LIP-selection efficiencies for the analysis reported in this thesis.

In any rare-event search experiment including the direct detection of dark matter, the understanding of backgrounds is crucial. A simulation study to estimate neutron backgrounds for an India-based dark matter search experiment at Jaduguda Underground Science Laboratory (JUSL) is performed [53]. Experiment at JUSL will be the first phase

[1] $\beta = \mathrm{v}/c$ and $\gamma = 1/\sqrt{1-\beta^2}$, where v is the velocity of LIP.

of a proposed Dark matter search at India-based Neutrino Observatory (DINO). It will be a direct detection experiment with a primary aim to search WIMPs. The experimental cavern at Jaduguda is located inside an existing mine under 555 m rock overburden. Neutron, as it easily mimics a dark matter signal, is an irreducible background for dark matter search experiments. Separating a WIMP signal from neutrons will be the greatest challenge at JUSL. It is therefore important to quantify the number of neutron backgrounds expected at the experimental cavern.

The thesis discusses LIPs search in SuperCDMS, and simulation of neutron backgrounds for a proposed dark matter search experiment at JUSL. The general motivation, various methods of LIPs search, and the current status is discussed in this chapter. This is followed by an introduction to dark matter searches which includes a description on the properties of dark matter, dark matter candidates and various search methods, and also a discussion on the possible backgrounds, including the importance of neutron background estimation, for a dark matter search experiment at JUSL. The remainder of the thesis describes various aspects of both the topics of the thesis. This includes a description of the SuperCDMS experiment, a discussion on the simulation framework developed for LIPs, the LIPs search analysis utilizing the simulation framework and the SuperCDMS data, and results. The simulation strategy to estimate the neutron backgrounds at JUSL and the results from the simulation are also discussed. Finally, the thesis concludes with a summary of the LIPs search analysis and simulation of neutron backgrounds.

1.1 Motivations for LIPs search

Maxwells equations relate divergence of electric fields to electric charge ($\nabla \cdot \mathbf{E} = \frac{\rho}{\epsilon_0}$), but magnetic fields are a divergence less ($\nabla \cdot \mathbf{B} = 0$) quantity. The introduction of magnetic

monopole into the equations would result in a symmetry between the electric and magnetic field components of the Maxwells equations [54]. Moreover, a calculation by Dirac suggested that the magnetic monopole would lead to quantization of electric charge [55]:

$$eg = \frac{n\hbar c}{2}, \tag{1.1}$$

where e and g are the electric and magnetic charge of a particle, c is the speed of light in vacuum, and n is an integer. For $g \neq 0$, the electric charge e has to be quantized. On the other hand, Polyakov [56] and 't Hooft [57] showed that any "Grand Unified Theory", which unifies strong, weak and electromagnetic interactions at extremely high energies into single guage interaction, naturally contain magnetic monopoles. It was later demonstrated by E. Witten that the magnetic monopoles, in the presence of CP violations, acquire an electric charge [58] in an effect called "Witten Effect" [59]. The acquired charge could have any value and as a result, the charge of the particle could be fractional.

Another major review on the subject of charge quantization/dequantization is by Foot, et al [60]. They have shown that the "minimal standard model (MSM)" Lagrangian[2] does not enforce the quantization of electric charge. The authors also noted that some extensions to the MSM, for example, the addition of three right-handed Majorana neutrinos however restores charge quantization. In summary, while some extensions to the standard model suggest mechanisms for enforcing quantization of charge [61, 62], some predict the existence of particles with a small fractional electric charge [63].

Though dark matter particles are thought to be neutral, there are compelling arguments for them to have small fractional charges, so small that they evade observational bounds [64]. Besides, a non-relativistic FCP has been proposed to explain the annual modulation signal

[2]The MSM is defined by its Lagrangian from Yang-Mills theory that describes the strong, weak and electromagnetic interactions [60].

observed by the DAMA/LIBRA [65] and CoGeNT [66] detectors [67, 68]. Therefore, the search for FCP dark-matter is crucial.

1.2 Search methods

There are a variety of methods, as described below, to search FCPs in experiments. In this section, the positively and negatively charged FCPs are symbollically expressed by F^{+q} and F^{-q}, respectively.

1.2.1 Accelerator fixed-target searches

FCPs can be produced in accelerators with fixed targets through the following processes.

$$\begin{aligned} p + N &\rightarrow F^{+q} + X, \\ \bar{p} + N &\rightarrow F^{+q} + X, \\ e + N &\rightarrow F^{+q} + X, \\ \mu + N &\rightarrow F^{+q} + X, \text{and} \\ \nu + N &\rightarrow F^{+q} + X, \end{aligned} \tag{1.2}$$

where N is a proton or a neutron, and X includes F^{-q} and other known particles. The conservations laws are assumed to hold in these processes. The choice of a process, of all those mentioned in Eqn. 1.2, in an experiment, depends on the availability of beams, detector equipment, and also on the properties assumed for F. If F is assumed to participate in the strong interaction, the $p + N \rightarrow F^{+q} + X$ and $\bar{p} + N \rightarrow F^{+q} + X$ are the most suitable. Similarly, if F participates in electro-magnetic interactions, $e + N \rightarrow F^{+q} + X$, and $\mu + N \rightarrow F^{+q} + X$ are used. Additionally, if F carries properties related to the lepton nature of e, μ, or ν, then the use of such beams is desirable.

The use of p or $\bar{p}$ beam has one major disadvantage that a huge number of ordinary particles (backgrounds) are also produced in the processes mentioned in Eqn. 1.2 making the analysis to search FCPs very difficult from overwhelming backgrounds. The background production is smaller in the case of other beams. The electron beams are commonly used as their availability is relatively easier in direct accelerator and electron-proton colliders.

The maximum mass of FCPs available in such search is given by

$$m_{F,max} = \sqrt{2 f m_N E}, \tag{1.3}$$

where m_N is the mass of the nucleon N of Eqn. 1.2, E is the beam energy, and f is a factor less than one to account for the fact that all of the beam energy is not available for FCP productions. Reviews on accelerator fixed-target searches can be found in Refs. [69, 70].

1.2.2 Searches in nucleus-nucleus collisions

Fractionally charged particles can be produced in high-energy nucleus-nucleus collisions where the confinement of quarks may not hold perfectly [71].

1.2.3 Electron-positron collider searches

The FCP production in electron-positron colliders can be symbolically expressed as

$$e^+ + e^- \rightarrow F^{+q} + X, \tag{1.4}$$

where $X = F^{-q}$ or $X = F^{-q}+$ other known SM particles. In the case of $X = F^{-q}$, the cross-section [72] of FCP production is known and is given by

$$\sigma = \left(\frac{2\pi\alpha^2}{3s}\right)\beta(3-\beta^2)\left(\frac{Q}{e}\right)^2, \tag{1.5}$$

where α is the fine structure constant, and $\beta = v/c$ with v being the velocity of FCP and c the speed of light in vacuum. The mass reach, in this case, is given by $m_{F,max} = E_{beam}$, where E_{beam} is the beam energy.

FCPs can be produced in Z^0 decays as well through the following process.

$$e^+ + e^- \rightarrow Z^0 \rightarrow F^{+q} + F^{-q}. \tag{1.6}$$

The mass of the FCPs produced in this process is given by $m_F = m_Z/2$, where m_Z is the mass of Z^0. Some electron-positron collider searches for FCPs can be found in Refs. [21–23, 25].

1.2.4 Proton-proton and proton-antiproton collider searches

The production of FCPs via proton-proton collision was explored at CMS in the LHC [27], and the same via proton-antiproton collision in the Tevatron collider [24].

1.2.5 Reactor based searches

Nuclear reactor cores are sources of gamma rays. The gammas from the reactor could convert into positively and negatively charged FCP pairs:

$$e^- + \gamma \rightarrow e^- + \gamma^* \rightarrow e^- + F^{+q} F^{-q} \tag{1.7}$$

The FCP pair thus produced can be detected in the detectors placed outside the reactor. Examples of reactor-based FCP-search can be found in Ref. [28–30].

1.2.6 Searches for FCPs in bulk-matter

The FCPs in bulk-matter could be produced in the early universe, or through interactions of ordinary cosmic rays with the earth's atmosphere [72]. A negatively charged FCP could be trapped in an atom by the Coulomb attraction of the nucleus. On the other hand, a positively charged FCP can act like a nucleus forming an atom. The Millikan liquid drop [38–41] and levitometer [42–47] methods are used to search FCPs in bulk matter.

1.2.7 Direct searches of LIPs

Cosmogenically produced LIPs can interact with detector materials producing events in the detector. The detectors in direct-detection experiments are kept at a low-background environment, typically underground, to reduce misidentification of non-FCP events as signal events. The FCPs in direct search could be produced in violent astrophysical processes such as supernovae, or through interactions of cosmic rays with the Earth's atmosphere. They could also be produced in the early universe and maybe a stable component of the materials in the present universe.

The direct detection of LIPs is particularly interesting because unlike collider and reactor-based searches, the method can search FCPs with masses inaccessible to the later search methods. The direct-detection experiments are sensitive to FCPs of any form of cosmic origin that are incident on the Earth. However, their sensitivity is limited by exposure and the amount of LIP flux that passes through the detector. There are a variety of direct searches conducted so far for FCPs including MACRO [34], Kamiokande [31, 32], LSD [33], CDMS II [35], MAJORANA [36] and TEXONO [37]. The experiments have excluded a large region of the intensity vs. charge parameter space of the particles.

1.3 Astrophysical and cosmological constraints

Astrophysical constraints on FCP mass vs. charge parameter-space come from the observations of red giants (RG) [48, 73–77], white dwarfs (WD) [48, 74] and supernova [78], and the cosmological constraints from the big-bang nucleosynthesis (BBN) [48], and cosmic microwave background (CMB) [79].

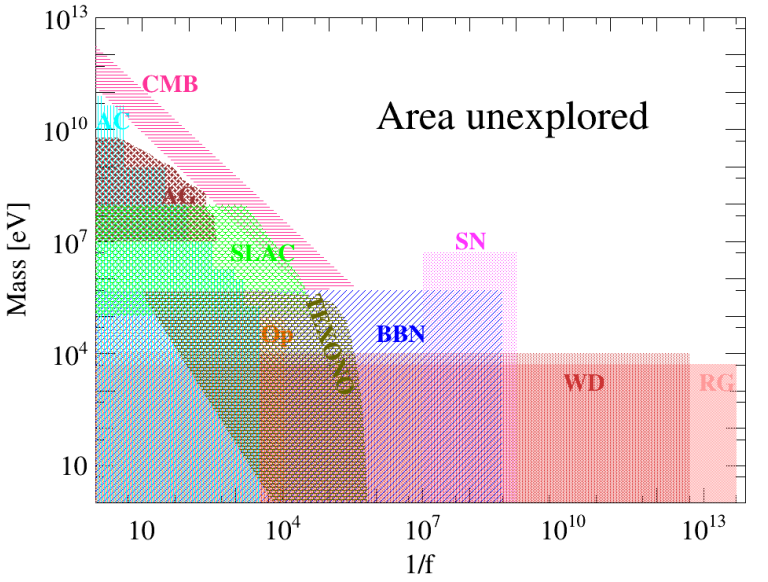

(a)

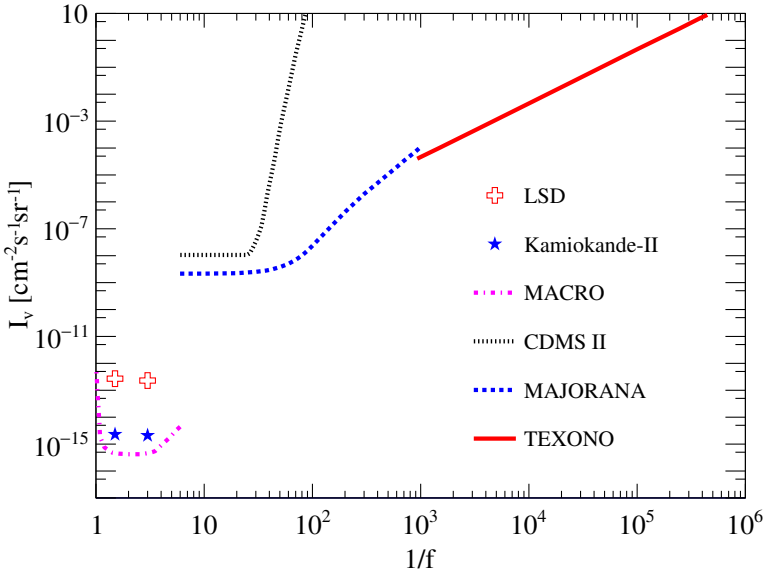

(b)

Figure 1.1: (a) Constraints on FCP mass-charge parameter space from astrophysical and cosmological observations and laboratory experiments. Constraints are adapted from Refs. [80, 81] and include those from accelerator-based experiments (AC) [15, 25], ArgoNeut (AG) [81], the search for the invisible decay of ortho-positronium (OP) [82], the SLAC millicharged particle search (SLAC) [18], Big Bang nucleosynthesis (BBN) [80], plasmon decay in red giants (RG) [48], plasmon decay in white dwarfs (WD) [48], the cosmic microwave background (CMB) [79] and Supernova 1987A (SN) [78]. (b) The intensity upper limits from various direct-detection experiments as a function of f^{-1} [32–37].

1.4 A review of the FCP searches

While no confirmed FCP detection has been reported, various astrophysical and cosmological observations and experimental measurements put constraints on FCP parameters. Figure 1.1 (a) shows the constraints on FCPs in the mass vs. charge parameter space. Observations of red giants (RG), white dwarfs (WD), supernovae (SN), and primordial nucleosynthesis (BBN) place constraints on fractionally charge particles with mass less than a ∼1 MeV as can be seen in the figure. Cosmic microwave background (CMB) data constrain the cosmological abundance of FCPs to $f^{-1} < 10^6$ [79].

FCPs with both large masses and small charges have a small probability of being produced in colliders. The smallest charge constrained from colliders is $\sim e/10^5$ ($f^{-1} = 10^5$) at the mass of 10 keV and the constraints start loosening at high masses, becoming $\sim e/10^3$ at 100 MeV [18]. Above 100 MeV, constraints from colliders loosen further to $> e/100$ [83].

Over the past thirty years, direct-search experiments have reported sensitivity to LIPs with an ever smaller electric charge. The upper limits on intensity of LIPs, from these experiments, as a function of f^{-1}, are shown in Fig. 1.1 (b). In the 1990s LSD [33] and Kamiokande [32] reported intensity limits on charge $e/3$ and $2e/3$. The 90 % confidence level (C.L.) upper limits on the intensity from LSD [33] for charges $e/3$ and $2e/3$ were:

$$\begin{aligned} I_v(\frac{1}{3}e) &\leq 2.3 \times 10^{-13}\,\mathrm{cm^{-2}sr^{-1}s^{-1}}, \text{and} \\ I_v(\frac{2}{3}e) &\leq 2.7 \times 10^{-13}\,\mathrm{cm^{-2}sr^{-1}s^{-1}}. \end{aligned} \tag{1.8}$$

The intensity limits from Kamikande II [32] were:

$$\begin{aligned} I_v(\frac{1}{3}e) &\leq 2.1 \times 10^{-15}\,\mathrm{cm^{-2}sr^{-1}s^{-1}}, \text{and} \\ I_v(\frac{2}{3}e) &\leq 2.3 \times 10^{-15}\,\mathrm{cm^{-2}sr^{-1}s^{-1}}. \end{aligned} \tag{1.9}$$

In 2006, MACRO [34] reported intensity limits of LIPs with charge $> e/6$ and the lowest limit obtained was 6.1×10^{-16} cm^{-2}s^{-1}sr^{-1}. In 2015, CDMS II [35] reported intensity limits for charges between $e/6$ and $e/200$ with the lowest intensity of 7×10^{-9} cm^{-2}s^{-1}sr^{-1}. In 2018, MAJORANA [36] reported intensity limits of LIPs with charges as small as $e/10^3$ with the lowest limit of 2×10^{-9} cm^{-2}s^{-1}sr^{-1} obtained in the experiment. In 2019, TEXONO [37] extended the limits to even smaller fractional charges, up to a $e/(3\times10^5)$.

FCPs bound to ordinary matter are searched in Levitometer [84] and Millikan-droplet [85] experiments. These experiments are generally sensitive to fractional charges close to an electron charge ($\gtrsim e/10$) and hence do not address FCPs with small electric charges. The results from various searches of FCPs bound to ordinary matter can be found in Ref. [72, 83]. A large region of the parameter space of LIPs is yet to be explored (see Fig. 1.1); this opens the possibility of finding LIPs in future experiments.

1.5 Introduction to dark matter

Observations of anisotropy cosmic microwave background (CMB) indicate that dark matter makes up ~27 % of the mass-energy content of the universe while the ordinary matter is only ~5 % and the rest of the universe is dark energy [86]. Dark matter does not participate in electromagnetic or strong interactions and is therefore non-visible or "dark". The evidence for dark matter comes from a variety of astrophysical and cosmological sources of both galactic and cosmic length scales. The "missing mass" in galaxy clusters [87], and within galaxies [88–93], the observations in CMB power spectrum [94, 95], Bullet cluster [96], and Large Scale Structure formation [97] all favor the existence of dark matter particles.

1.6 Dark matter properties

The astrophysical and cosmological observations suggest the following properties of dark matter:

- *Cold and weakly interacting:* The structure formation physics indicate dark matter to be non-relativistic [98, 99] or cold. Since dark matter interaction is not yet detected, it is assumed that the interaction strength should be of a weak scale.
- *Weak self-interactions:* The self-interaction of dark matter is very weak ($\sigma_{DM-DM}/m_{DM} < 1\,\mathrm{cm}^2\mathrm{g}^{-1}$) as has been observed in Bullet cluster [96].
- *Stable and abundant:* The comparison of dark matter abundance in the early universe (measured through CMB) and in the current times (measured through rotational curves and dwarf galaxies) shows that the amount of dark matter has not decreased significantly over time. On the other hand, the present universe has nearly five times more dark matter than ordinary matter. Therefore, dark matter should be stable and abundant.

1.7 Dark matter candidates

There are many candidates of dark matter proposed in particle physics theories [100]. Some important candidates are WIMPs, axions [101, 102], and sterile neutrinos [103–105]. The most favored candidates for dark matter are WIMPs. They can interact with standard model (SM) particles at most on the scale of the weak interaction. These particles are neutral and massive with masses expected to be between 1 GeV/c^2 and 10 TeV/c^2.

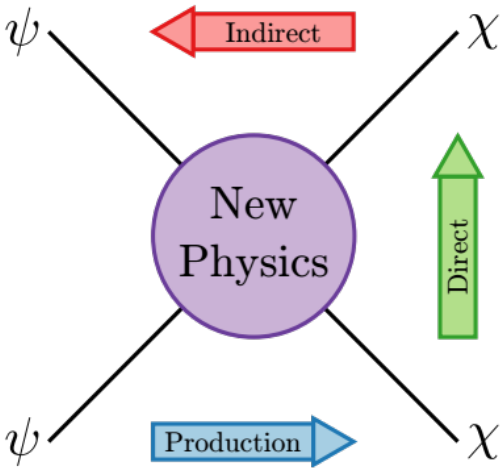

Figure 1.2: Feynman diagrams describing methods of dark matter detection [106]. Dark matter and standard model particle in the figure are shown by the symbols χ and ψ, respectively.

1.8 Detection methods

There are three approaches to dark matter detection: collider production, indirect detection, and direct detection. Figure 1.2 shows a cartoon describing the three detection methods.

- **Collider production:** The collision of two SM particles (ψ) at high energy can produce dark matter (χ). The reconstruction of decay particles and missing energy in collisions would infer the production of dark matter. ATLAS and CMS at LHC search production of DM [107].

- **Indirect detection:** Indirect detection experiments look for signatures of dark matter annihilation that results in SM particles. The annihilation product could be neutrinos, charged particles, or gammas. They are detected in satellites and analyzed for an excess in these particles to infer dark matter. Some of the indirect-detection experiments are MAGIC, VERITAS, HESS, HAWX, and LHAASO [108].

- **Direct detection:** A dark matter particle can elastically scatter off a nucleus or electron and causes nuclear or electron recoil. The direct-detection method aims to find such recoils. Some examples of direct detection experiments are SuperCDMS, CRESST, LZ, and PICO [109].

1.9 Possible backgrounds for a dark matter search experiment at JUSL

An event with the potential of mimicking a signal is commonly referred to as the background. The sensitivity of a rare-event search experiment including the dark matter search at JUSL could be affected by various backgrounds that can produce events in detectors. It is, therefore, crucial to identify and estimate all possible backgrounds at JUSL that could impact the results of the experiment. The possible backgrounds at JUSL can be classified into two major categories: 1) cosmogenic backgrounds, and 2) radiogenic backgrounds. They are described below.

Cosmic rays consist of mostly protons; they interact with the atmosphere producing secondary showers of particles. The secondary showers primarily contain pions, muons, and neutrons. These cosmogenically produced muons are very energetic and can traverse large distances through the rock of the earth-overburden. The interaction of muons with the rock can further produce secondaries; the secondaries as well as the primary muons can reach the detectors in the underground laboratory. Since JUSL is under the rock overburden of nearly 555 m (or 1060 m.w.e), the shielding provided by the rock itself reduces cosmic muons by a significant amount underground. However, the residual muons that could not be shielded and their secondaries are backgrounds to the experiment.

The radiogenic backgrounds are due to the radioactivity of the materials near detectors

in the experiment. The isotopes with long half-lives such as the ^{238}U, ^{232}Th, and ^{40}K were generated during the earth's formation and their traces are present in the cavern rock. These isotopes have a long decay chain and undergo many alpha and beta decays before reaching the stable lead isotopes. The decays are often accompanied by the emission of gammas. ^{40}K isotope also emits gammas. These decay products are the radiogenic backgrounds for the experiment. The α particles from the decay chain can also interact with the surrounding material and produce neutrons in (α, n) reactions. Additionally, the uranium and thorium isotopes undergo spontaneous fission-producing neutrons. These neutrons are backgrounds to the experiment.

1.9.1 Neutron backgrounds

Of all the backgrounds that could induce events in the detector, neutrons are the most important since neutron interaction with detector is similar to WIMPs. A WIMP interaction with the detector is a nuclear recoil (NR) as the particle interacts only with the nucleus of a detector atom. Neutrons also produce NR events and similar to WIMPs, deposit keV-scale energy in the detector. Other backgrounds, such as the gammas and beta particles, interact with electrons and produce electron recoil (ER) events in the detector [110]. The energy deposited in particle interactions is generally collected through ionization, phonon, or scintillation channels of energy measurement depending on the detector material [106]. A combination of two energy measurement channels is typically used in direct-detection experiments to discriminate between ER and NR events [106]. This type of discrimination can be used to separate neutrons from backgrounds that cause electron recoils in the detector. However, the same is not useful to separate WIMPs from neutron events since both produce nuclear recoils in the detector; consequently, neutrons are indistinguishable from WIMPs in direct-detect experiments. It is therefore crucial to estimate the total

neutron backgrounds at JUSL. In this thesis, the cosmogenic and radiogenic neutrons are estimated using GEANT4-based simulations.

Bibliography

[1] Donald E. Groom, Nikolai V. Mokhov, and Sergei I. Striganov. *Atom. Data Nucl. Data Tabl.* 78 (2001), 183–356.

[2] L.B. Okun, M.B. Voloshin, and V.I. Zakharov. *Physics Letters B* 138.1 (1984), 115 –120.

[3] N. Vinyoles and H. Vogel. *Journal of Cosmology and Astroparticle Physics* 2016.03 (2016), 002–002.

[4] Bob Holdom. *Physics Letters B* 166.2 (1986), 196 –198.

[5] R. Foot, G.C. Joshi, H. Lew, et al. *Modern Physics Letters A* 05.02 (1990), 95–100. eprint: https://doi.org/10.1142/S0217732390000123.

[6] Emidio Gabrielli, Luca Marzola, Martti Raidal, et al. *Journal of High Energy Physics* 2015.8 (2015), 150.

[7] James M. Cline, Zuowei Liu, and Wei Xue. *Phys. Rev. D* 85 (10 2012), 101302.

[8] A.Yu. Ignatiev, V.A. Kuzmin, and M.E. Shaposhnikov. *Physics Letters B* 84.3 (1979), 315 –318.

[9] Xiao-Gang Wen and Edward Witten. *Nuclear Physics B* 261 (1985), 651 –677.

[10] A.N. Schellekens. *Physics Letters B* 237.3 (1990), 363 –369.

[11] K. S. Babu and Rabindra N. Mohapatra. *Phys. Rev. D* 41 (1 1990), 271–277.

[12] Chris Kouvaris. *Phys. Rev. D* 88 (1 2013), 015001.

[13] J.J. Aubert, G. Bassompierre, K.H. Becks, et al. "A search for free quarks in deep inelastic muon scattering". *Physics Letters B* 133.6 (1983), 461 –466.

[14] F. Bergsma, J. Dorenbosch, M. Jonker, et al. *Zeitschrift für Physik C Particles and Fields* 24.3 (1984), 217–218.

[15] E. Golowich and R. W. Robinett. *Phys. Rev. D* 35 (1 1987), 391–393.

[16] G. Hüntrup, D. Weidmann, S. E. Hirzebruch, et al. *Phys. Rev. C* 53 (1 1996), 358–361.

[17] Dipak Ghosh, Sunil K. Das, and Anit Ghosh. *Fizika B* 5.1 (1996), 135–140.

[18] A. A. Prinz, R. Baggs, J. Ballam, et al. "Search for millicharged particles at SLAC". *Phys. Rev. Lett.* 81 (1998), 1175–1178. arXiv: hep-ex/9804008.

[19] Davison E. Soper, Michael Spannowsky, Chris J. Wallace, et al. *Phys. Rev. D* 90 (11 2014), 115005.

[20] F. Abe, D. Amidei, C. Anway-Weiss, et al. *Phys. Rev. D* 46 (5 1992), R1889–R1894.

[21] D. Buskilic, D. Decamp, C. Goy, et al. *Physics Letters B* 303.1 (1993), 198 –208.

[22] R. Akers, G. Alexander, J. Allison, et al. *Zeitschrift für Physik C Particles and Fields* 67 (2 1995), 203–211.

[23] P. Abreu, W. Adam, T. Adye, et al. *Physics Letters B* 396.1 (1997), 315 –326.

[24] D. Acosta, T. Affolder, H. Akimoto, et al. *Phys. Rev. Lett.* 90 (13 2003), 131801.

[25] G. Abbiendi, C. Ainsley, P.F. Å kesson, et al. *Physics Letters B* 572.1 (2003), 8 –20.

[26] Joerg Jaeckel, Martin Jankowiak, and Michael Spannowsky. *Physics of the Dark Universe* 2.3 (2013), 111 –117.

[27] S. Chatrchyan, V. Khachatryan, A. M. Sirunyan, et al. *Phys. Rev. D* 87 (9 2013), 092008.

[28] S. N. Gninenko, N. V. Krasnikov, and A. Rubbia. *Phys. Rev. D* 75 (7 2007), 075014.

[29] Jiunn-Wei Chen, Hsin-Chang Chi, Hau-Bin Li, et al. *Phys. Rev. D* 90 (1 2014), 011301.

[30] L. Singh, J. W. Chen, H. C. Chi, et al. *Phys. Rev. D* 99 (3 2019), 032009.

[31] M. Aglietta, P. Antonioli, G. Badino, et al. *Astroparticle Physics* 2.1 (1994), 29 –34.

[32] Ping-Kai Hu, Alexander Kusenko, and Volodymyr Takhistov. *Physics Letters B* 768 (2017), 18 –22.

[33] M. Mori, Y. Oyama, A. Suzuki, et al. *Phys. Rev. D* 43 (9 1991), 2843–2846.

[34] M. Ambrosio, R. Antolini, G. Auriemma, et al. *Phys. Rev. D* 62 (5 2000), 052003.

[35] R. Agnese, A. J. Anderson, D. Balakishiyeva, et al. *Phys. Rev. Lett.* 114 (11 2015), 111302.

[36] S. I. Alvis, I. J. Arnquist, F. T. Avignone, et al. *Phys. Rev. Lett.* 120 (21 2018), 211804.

[37] L. Singh, J. W. Chen, H. C. Chi, et al. "Constraints on millicharged particles with low-threshold germanium detectors at Kuo-Sheng Reactor Neutrino Laboratory". *Phys. Rev. D* 99 (3 2019), 032009.

[38] David C. Joyce, Peter C. Abrams, Roger W. Bland, et al. "Search for Fractional Charges in Water". *Phys. Rev. Lett.* 51 (9 1983), 731–734.

[39] V. Halyo, P. Kim, E. R. Lee, et al. "Search for free fractional electric charge elementary particles". *Phys. Rev. Lett.* 84 (2000), 2576–2579. arXiv: hep-ex/9910064.

[40] Irwin T. Lee, Sewan Fan, Valerie Halyo, et al. "Large bulk matter search for fractional charge particles". *Phys. Rev. D* 66 (1 2002), 012002.

[41] Peter C. Kim, Eric R. Lee, Irwin T. Lee, et al. *Phys. Rev. Lett.* 99 (16 2007), 161804.

[42] George S. LaRue, James D. Phillips, and William M. Fairbank. "Observation of Fractional Charge of $(\frac{1}{3})e$ on Matter". *Phys. Rev. Lett.* 46 (15 1981), 967–970.

[43] M. Marinelli and G. Morpurgo. "The electric neutrality of matter: A summary". *Physics Letters B* 137.5 (1984), 439–442.

[44] P.F. Smith, G.J. Homer, J.D. Lewin, et al. "Searches for fractional electric charge in tungsten". *Physics Letters B* 197.3 (1987), 447–451.

[45] P.F. Smith, G.J. Homer, J.D. Lewin, et al. "A search for fractional charge changes on levitated niobium spheres". *Physics Letters B* 171.1 (1986), 129–134.

[46] W. G. Jones, P. F. Smith, G. J. Homer, et al. "Searches for fractional electric charge in meteorite samples". *Zeitschrift für Physik C Particles and Fields* 43.3 (1989), 349–355.

[47] G. J. Homer, P. F. Smith, J. D. Lewin, et al. "A search for fractional electric charge in sea water". *Zeitschrift für Physik C Particles and Fields* 55.4 (1992), 549–554.

[48] S. Davidson, B. Campbell, and D. Bailey. "Limits on particles of small electric charge". *Phys. Rev. D* 43 (7 1991), 2314–2321.

[49] R. Agnese et al. "Low-mass dark matter search with CDMSlite". *Phys. Rev. D* 97.2 (2018), 022002. arXiv: 1707.01632 [astro-ph.CO].

[50] I. Alkhatib et al. "Constraints on Lightly Ionizing Particles from CDMSlite" (Nov. 2020). arXiv: 2011.09183 [hep-ex].

[51] S. Agostinelli, J. Allison, K. Amako, et al. *Nucl. Instrum. Methods Phys. Res. A* 506.3 (2003), 250 –303.

[52] S. Banik, V.K.S. Kashyap, M.H. Kelsey, et al. "Simulation of energy loss of fractionally charged particles using Geant4". *Nuclear Instruments and Methods in Physics Research Section A: Accelerators, Spectrometers, Detectors and Associated Equipment* 971 (2020), 164114.

[53] S. Banik, V. K. S. Kashyap, S. Ghosh, et al. "Simulation of neutron background for a dark matter search experiment at JUSL". *JINST* 16.06 (2021), P06022.

[54] J Preskill. "Magnetic Monopoles". *Annual Review of Nuclear and Particle Science* 34.1 (1984), 461–530. eprint: https://doi.org/10.1146/annurev.ns.34.120184.002333.

[55] Paul Adrien Maurice Dirac. "Quantised singularities in the electromagnetic field," *Proc. Roy. Soc. Lond. A* 133.821 (1931), 60–72.

[56] Alexander M. Polyakov. "Particle Spectrum in the Quantum Field Theory". *JETP Lett.* 20 (1974), 194–195.

[57] Gerard 't Hooft. "Magnetic Monopoles in Unified Gauge Theories". *Nucl. Phys. B* 79 (1974), 276–284.

[58] Edward Witten. "Dyons of Charge e theta/2 pi". *Phys. Lett. B* 86 (1979), 283–287.

[59] F. Alexander Bais. *To be or not to be? Magnetic monopoles in non-Abelian gauge theories*. 2005. arXiv: hep-th/0407197.

[60] Robert Foot, H. Lew, and R. R. Volkas. "Electric charge quantization". *J. Phys. G* 19 (1993). [Erratum: J.Phys.G 19, 1067 (1993)], 361–372. arXiv: hep-ph/9209259.

[61] Michael B. Green, J. H. Schwarz, and Edward Witten. *Super-string theory*. Cambridge University Press, Cambridge, England, 1986.

[62] Graham G. Ross. *GRAND UNIFIED THEORIES*. 1985.

[63] Bob Holdom. "Searching for ϵ charges and a new U(1)". *Physics Letters B* 178.1 (1986), 65–70.

[64] Gary Shiu, Pablo Soler, and Fang Ye. "Millicharged Dark Matter in Quantum Gravity and String Theory". *Phys. Rev. Lett.* 110 (24 2013), 241304.

[65] R. Bernabei, P. Belli, F. Cappella, et al. "First results from DAMA/LIBRA and the combined results with DAMA/NaI". *The European Physical Journal C* 56.3 (2008), 333–355.

[66] C. E. Aalseth, P. S. Barbeau, J. Colaresi, et al. "Search for an Annual Modulation in a *p*-Type Point Contact Germanium Dark Matter Detector". *Phys. Rev. Lett.* 107 (14 2011), 141301.

[67] R. Foot. "Can dark matter-electron scattering explain the DAMA annual modulation signal?" *Phys. Rev. D* 90 (12 2014), 121302.

[68] R. Foot and S. Vagnozzi. "Diurnal modulation signal from dissipative hidden sector dark matter". *Physics Letters B* 748 (2015), 61–66.

[69] Lawrence W. Jones. "A review of quark search experiments". *Rev. Mod. Phys.* 49 (4 1977), 717–752.

[70] L. Lyons. "Quark Search Experiments at Accelerators and in Cosmic Rays". *Phys. Rept.* 129 (1985), 225.

[71] G. Hüntrup, D. Weidmann, S. E. Hirzebruch, et al. "Search for fractionally charged nuclear fragments in relativistic heavy ion collisions". *Phys. Rev. C* 53 (1 1996), 358–361.

[72] Martin L. Perl, Eric R. Lee, and Dinesh Loomba. *Annual Review of Nuclear and Particle Science* 59.1 (2009), 47–65. eprint: https://doi.org/10.1146/annurev-nucl-121908-122035.

[73] Jeremy Bernstein, Malvin Ruderman, and Gerald Feinberg. "Electromagnetic Properties of the Neutrino". *Phys. Rev.* 132 (3 1963), 1227–1233.

[74] M. I. Dobroliubov and A. Yu. Ignatiev. "Millicharged particles". *Phys. Rev. Lett.* 65 (6 1990), 679–682.

[75] Sacha Davidson and Michael Peskin. “Astrophysical bounds on millicharged particles in models with a paraphoton”. *Phys. Rev. D* 49 (4 1994), 2114–2117.

[76] R.N. MOHAPATRA and S. NUSSINOV. “ELECTRIC CHARGE NONCONSERVATION AND MINICHARGED PARTICLES—PHENOMENOLOGICAL IMPLICATIONS”. *International Journal of Modern Physics A* 07.16 (1992), 3817–3834. eprint: https://doi.org/10.1142/S0217751X92001708.

[77] Martin Haft, Georg Raffelt, and Achim Weiss. “Standard and nonstandard plasma neutrino emission revisited”. *Astrophys. J.* 425 (1994). [Erratum: Astrophys.J. 438, 1017 (1995)], 222–230. arXiv: astro-ph/9309014.

[78] R.N. Mohapatra and I.Z. Rothstein. “Astrophysical constraints on mini-charged particles”. *Physics Letters B* 247.4 (1990), 593–600.

[79] S. L. Dubovsky, D. S. Gorbunov, and G. I. Rubtsov. “Narrowing the window for millicharged particles by CMB anisotropy”. *Journal of Experimental and Theoretical Physics Letters* 79.1 (2004), 1–5.

[80] Sacha Davidson, Steen Hannestad, and Georg Raffelt. “Updated bounds on millicharged particles”. *Journal of High Energy Physics* 2000.05 (2000), 003–003.

[81] Roni Harnik, Zhen Liu, and Ornella Palamara. “Millicharged particles in liquid argon neutrino experiments”. *J. High Energy Phys.* 2019.7 (2019), 170.

[82] A. Badertscher et al. “Improved limit on invisible decays of positronium”. *Phys. Rev. D* 75 (3 2007), 032004.

[83] MARTIN L. PERL, PETER C. KIM, VALERIE HALYO, et al. “THE SEARCH FOR STABLE, MASSIVE, ELEMENTARY PARTICLES”. *International Journal of Modern Physics A* 16.12 (2001), 2137–2164. eprint: https://doi.org/10.1142/S0217751X01003548.

[84] P. F. Smith. “Searches for fractional electric charge in terrestrial materials”. *Ann. Rev. Nucl. Part. Sci.* 39 (1989), 73–111.

[85] R. A. Millikan. “A New Modification of the Cloud Method of Determining the Elementary Electrical Charge and the most Probable Value of that Charge”. *Phil. Mag. Ser. 6* 19 (1910), 209.

[86] Planck Collaboration, Ade, P. A. R., Aghanim, N., et al. "Planck 2015 results - XIII. Cosmological parameters". *A&A* 594 (2016), A13.

[87] G. Squires, Nick Kaiser, A. Babul, et al. "The Dark matter, gas and galaxy distributions in Abell-2218: A Weak gravitational lensing and x-ray analysis". *Astrophys. J.* 461 (1996), 572. arXiv: astro-ph/9507008.

[88] Louis E. Strigari, James S. Bullock, Manoj Kaplinghat, et al. "A common mass scale for satellite galaxies of the Milky Way". *Nature* 454 (2008), 1096–1097. arXiv: 0808.3772 [astro-ph].

[89] Joshua D. Simon and Marla Geha. "The Kinematics of the Ultra-Faint Milky Way Satellites: Solving the Missing Satellite Problem". *Astrophys. J.* 670 (2007), 313–331. arXiv: 0706.0516 [astro-ph].

[90] Matthew Walker. "Dark Matter in the Galactic Dwarf Spheroidal Satellites". *Planets, Stars and Stellar Systems: Volume 5: Galactic Structure and Stellar Populations*. Dordrecht: Springer Netherlands, 2013, pp. 1039–1089.

[91] Alan W. McConnachie. "THE OBSERVED PROPERTIES OF DWARF GALAXIES IN AND AROUND THE LOCAL GROUP". *The Astronomical Journal* 144.1 (2012), 4.

[92] Vera C. Rubin and W. Kent Ford Jr. "Rotation of the Andromeda Nebula from a Spectroscopic Survey of Emission Regions". *Astrophys. J.* 159 (1970), 379–403.

[93] Yoshiaki Sofue and Vera Rubin. "Rotation curves of spiral galaxies". *Ann. Rev. Astron. Astrophys.* 39 (2001), 137–174. arXiv: astro-ph/0010594.

[94] K. Nakamura et al. "Review of particle physics". *J. Phys. G* 37 (2010), 075021.

[95] Brian Fields and Subir Sarkar. "Big-Bang nucleosynthesis (2006 Particle Data Group mini-review)" (Jan. 2006). arXiv: astro-ph/0601514.

[96] Douglas Clowe, Maruša Bradač, Anthony H. Gonzalez, et al. "A Direct Empirical Proof of the Existence of Dark Matter". *The Astrophysical Journal* 648.2 (2006), L109–L113.

[97] P. Coles and F. Lucchin. *Cosmology: The Origin and evolution of cosmic structure*. 1995.

[98] Volker Springel, Carlos S. Frenk, and Simon D. M. White. "The large-scale structure of the Universe". *Nature* 440 (2006), 1137. arXiv: astro-ph/0604561.

[99] Volker Springel et al. "Simulating the joint evolution of quasars, galaxies and their large-scale distribution". *Nature* 435 (2005), 629–636. arXiv: astro-ph/0504097.

[100] Jonathan L. Feng. "Dark Matter Candidates from Particle Physics and Methods of Detection". *Ann. Rev. Astron. Astrophys.* 48 (2010), 495–545. arXiv: 1003.0904 [astro-ph.CO].

[101] Leanne D. Duffy and Karl van Bibber. "Axions as Dark Matter Particles". *New J. Phys.* 11 (2009), 105008. arXiv: 0904.3346 [hep-ph].

[102] Jihn E. Kim. "A Review on axions and the strong CP problem". *AIP Conf. Proc.* 1200.1 (2010), 83–92. arXiv: 0909.3908 [hep-ph].

[103] Scott Dodelson and Lawrence M. Widrow. "Sterile neutrinos as dark matter". *Phys. Rev. Lett.* 72 (1 1994), 17–20.

[104] Takehiko Asaka, Steve Blanchet, and Mikhail Shaposhnikov. "The νMSM, dark matter and neutrino masses". *Physics Letters B* 631.4 (2005), 151–156.

[105] A. D. Dolgov, S. L. Dubovsky, G. I. Rubtsov, et al. "Constraints on millicharged particles from Planck data". *Phys. Rev. D* 88.11 (2013), 117701. arXiv: 1310.2376 [hep-ph].

[106] D'Ann Rebekah Barker. "SuperCDMS Background Models for Low-Mass Dark Matter Searches". PhD thesis. Minnesota U., 2018.

[107] Antonio Boveia and Caterina Doglioni. "Dark Matter Searches at Colliders". *Ann. Rev. Nucl. Part. Sci.* 68 (2018), 429–459. arXiv: 1810.12238 [hep-ex].

[108] Rebecca K. Leane. "Indirect Detection of Dark Matter in the Galaxy". *3rd World Summit on Exploring the Dark Side of the Universe*. May 2020. arXiv: 2006.00513 [hep-ph].

[109] Marc Schumann. "Direct Detection of WIMP Dark Matter: Concepts and Status". *J. Phys. G* 46.10 (2019), 103003. arXiv: 1903.03026 [astro-ph.CO].

[110] Mark David Pepin. "Low-Mass Dark Matter Search Results and Radiogenic Backgrounds for the Cryogenic Dark Matter Search". PhD thesis. Minnesota U., 2016.

Chapter 2

SuperCDMS experiment

The Super Cryogenic Dark Matter Search (SuperCDMS) is a direct-detection dark matter search experiment that aims to detect dark matter particle with germanium or silicon detectors. SuperCDMS Soudan experiment operated from 2012 to 2015 in the Soudan iron ore mine in Minnesota, USA. This chapter describes the SuperCDMS experiment at Soudan. It begins with a brief description of the Soudan mine in Section 2.1. This is followed by a discussion on shielding used in the experiment in Section 2.2. The detectors used in the experiment are described in Section 2.3. The detectors measure ionization and phonon signals from particle interactions; they are described in Section 2.4 and Section 2.5, respectively. The processing of the SuperCDMS data is described in Section 2.6 and various data-taking runs in Section 2.7. The experiment operated some detectors in a high-bias-voltage mode, called CDMS low ionization threshold experiment (CDMSlite), to achieve a low threshold of energy depositions. The data taken in the second CDMSlite Run is used in the LIPs search analysis. Section 2.8 discusses CDMSlite as well as the energy calibration and resolution in CDMSlite Run 2. The chapter concludes with a summary in Section 2.9.

2.1 The Soudan mine

The Soudan mine was an iron ore mine that opened in 1882. The mine stopped its operation in 1962 and various scientific endeavors have taken place since then at Soudan. It began with the Soudan 1 proton decay experiment at 590 m below ground in the early 1980s. This was followed by a second experiment, Soudan 2, nearly 713 m below ground and was operational from the late 1980s until the 2000s. The underground cavern was then expanded to house many other experiments including Main Injector Neutrino Oscillation Experiment (MINOS) [1] and Cryogenic Dark Matter Search Experiment (CDMS) [2]. Figure 2.1 shows the graphical rendering of the Soudan Underground Laboratory (SUL). The science runs of CDMS at SUL, known as CDMS II and SuperCDMS experiments, took place from 2003 to 2008 and 2012 to 2015, respectively.

2.2 Shielding

The SuperCDMS shielding is designed to reject/reduce backgrounds from cosmic rays, the radioactivity of rock around the cavern and the experimental apparatus. The experimental cavern is beneath a ~780 m rock overburden which itself provides ~2090 meter water equivalent (m.w.e) shielding from cosmic rays. The overburden reduces the flux of muons relative to the surface by a factor of 5×10^4 [2]. However, the remaining muons which could not be shielded by the earth's overburden and the secondaries generated from muon interactions can also produce events in the detector. To identify and remove muon-veto-coincident events, an array of muon-veto panels were employed. Fig. 2.2 shows the muon veto panels and various shielding layers used in the experiment. There were forty veto panels, each with a 5 cm thick Bicron BC-408 ($H_{11}C_{10}$) plastic, connected to photomultiplier tubes (PMTs); they make the outermost layer of the shielding. The panels are overlapped

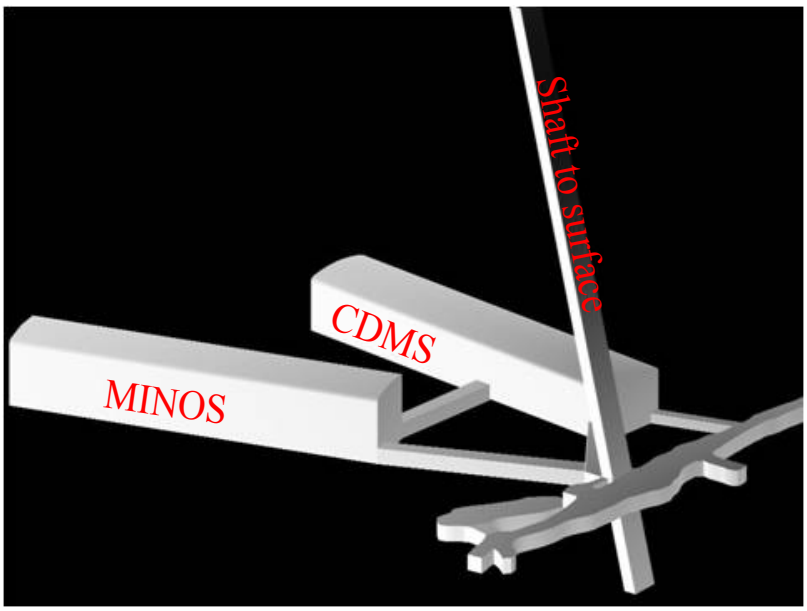

Figure 2.1: A graphical rendering of the Soudan Underground Laboratory [3]. The white space within the rock in black indicates the open space. The large rectangular blocks are the Soudan 2 (right-block) and MINOS (left-block) caverns, respectively. The CDMS experiment was housed in the Soudan 2 cavern. The caverns are connected by various tunnels. The vertical (slightly tilted) tunnel is the shaft to the surface.

in a fashion that prevents any direct line-of-sight to the detectors placed inside. The veto panels are shown in Fig. 2.2 by the blue rectangles that are connected to PMTs shown in black.

Inside the veto panels, there were layers of shields (or moderators) for gammas and neutrons. The outer layer is 40 cm thick polyethylene bricks to moderate neutrons. Two layers of lead (natural lead and "ancient lead") with a total thickness of 22.5 cm, inside the polyethylene layer, were used to shield gammas. After the lead layers, there was another layer of polyethylene of thickness 10 cm to shield neutrons that are produced in the outer polyethylene and lead layers. The polyethylene layers are shown in green and the lead layers in grey in Fig. 2.2. A layer of mu-metal (81 % Ni, 19 % Fe) with 0.381 mm thickness was used inside the inner polyethylene layer to block any magnetic fields that could interfere

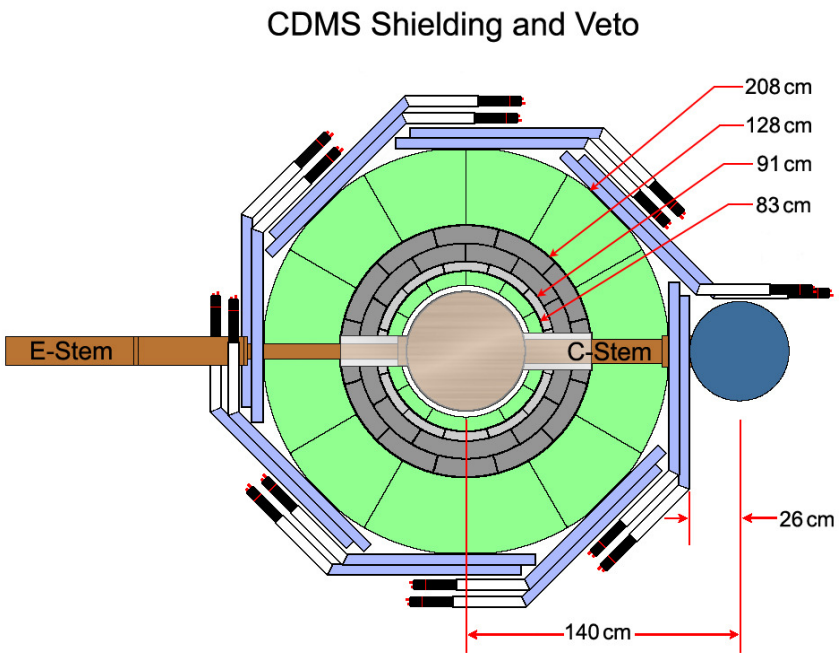

(a) Top View

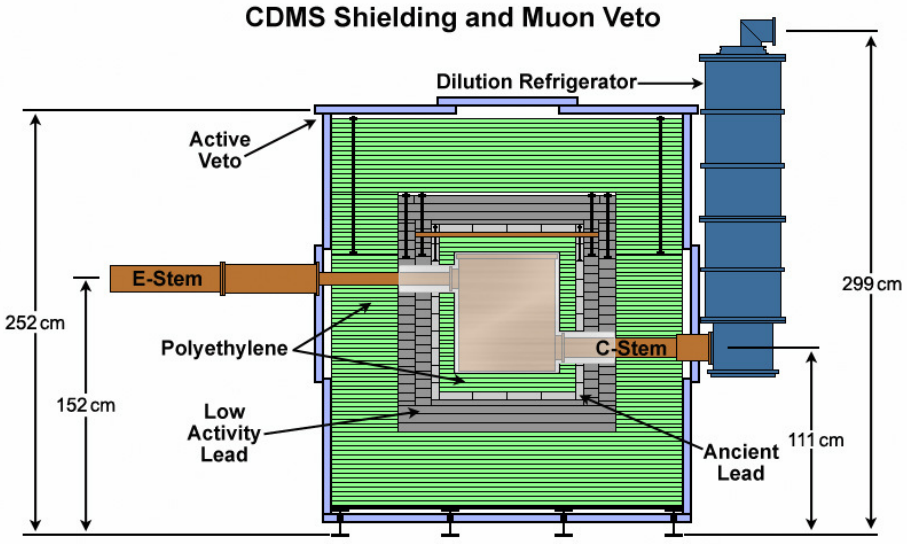

(b) Side View

Figure 2.2: The top (a) and side (b) view of the SuperCDMS shielding. The outermost light blue layers are the active veto panels connected to the PMTs shown in white. From the outside, the passive shielding layers are as follows: a 40 cm thick polyethylene layer (green), an 18 cm thick natural lead (grey), a 4.5 cm ancient lead (light grey), and another 10 cm thick polyethylene layer (green). The dilution refrigerator on the right is shown in blue and the cryostat in the center in light brown. Figures courtesy A. Villano and J. Sanders.

with detector electronics operations.

The ^{210}Pb isotope, with a half-life of 22.3 yr, is found in the natural lead. The decay product of this isotope can create bremsstrahlung which could be a source of electromagnetic background. The ancient lead (recovered from a sunken Roman ship found in the Mediterranean), on the other hand, is depleted of ^{210}Pb. A layer of ancient lead with a thickness of 4.5 cm was used after the natural lead layer to shield against the bremsstrahlung.

The gap between the mu-metal and the cryostat inside was flushed with a dry nitrogen purge to reduce ^{222}Rn contamination from mine air as ^{222}Rn is a source of ^{210}Pb. The cryostat cans were radio-pure copper built and provide an additional shield against γ and β particles.

The thicknesses of different shielding layers are optimized in the following way. Monte carlo simulations with GEANT3 were run to see how much lead and polyethylene suppress environmental photon and low energy neutron background. It was found that each 5 cm of Pb cuts photon background a factor of 10-20, and each 10 cm of polyethylene suppresses neutrons from fission in the rock by a factor of 10. High energy cosmic muons generate neutrons from lead, so it's good to have some polyethylene inside most of the lead, along with a veto outside the poly, because poly isn't good at stopping high energy neutrons. With this preliminary understanding of what parts of the shield would do, Geant models of possible shields were chosen and tuned to get estimated backgrounds to an acceptable level.

2.3 Detectors

SuperCDMS employed 15 detectors stacked in five towers. The arrangement of the detectors in the towers is shown in Fig. 2.3 (a). The detectors were named according to their position

in various towers of the arrangement. The top detector in the fifth tower, for example, is called T5Z1. The detectors were cylindrical in shape with a diameter of 7.6 cm and a thickness 2.5 cm. The material of the detectors is germanium. Figure 2.3 (b) shows a single detector module.

To measure the phonon and charge signals from particle interactions inside the detector, the top and bottom faces were equipped with phonon and charge sensors which form four phonon channels and two charge channels. The phonon and charge sensors were interleaved; the SuperCDMS detectors are therefore called interleaved Z-sensitive Ionization and Phonon (iZIP) detectors. Figure 2.3 (c) shows the phonon channels (A, B, C, and D) and the charge channels (inner disk and outer ring) of SuperCDMS detectors. Phonon sensors were biased with 0 V and charge sensors typically with ~4 V. The phonon and charge traces of a typical event is shown in Fig. 2.4. Some of the iZIP detectors, to achieve a low energy threshold for energy-deposition measurements, were operated with a high bias voltage (50–80 V) [4]. This high-bias-voltage operation of SuperCDMS detectors is called CDMS low ionization threshold experiment (CDMSlite) [4], and the detectors are sometimes referred to as CDMSlite detectors.

The interaction of the incident particle in the detector could be either an electron recoil (ER) or a nuclear recoil (NR). The measurement of ionization and phonon signals in ERs and NRs are discussed below.

2.4 Ionization signal

When a particle interacts in a SuperCDMS detector, a part of the deposited energy goes into exciting electrons from the valence to conduction band and the remaining energy into the production of optical phonons [3, 6]. A vacancy created in the valance band acts

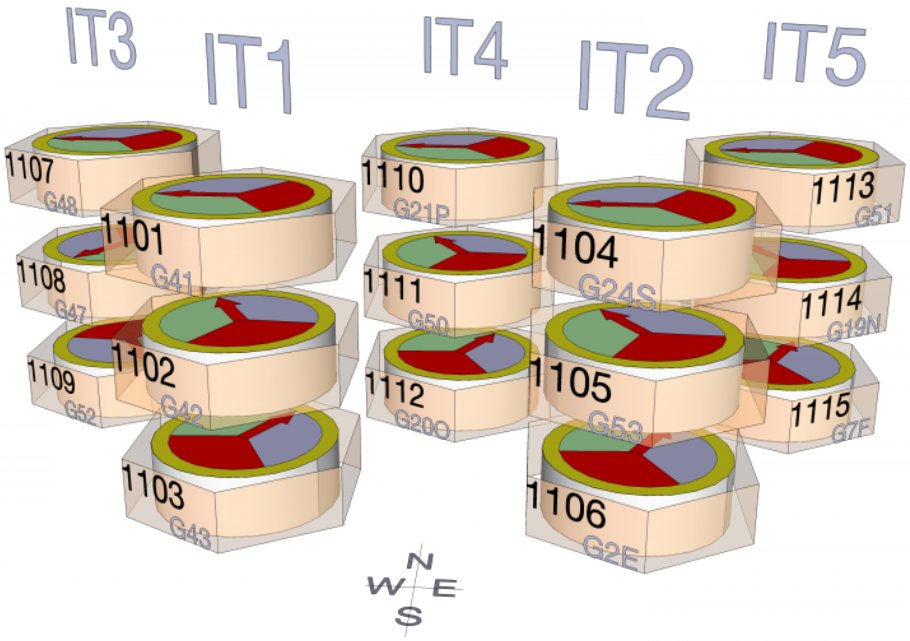

(a)

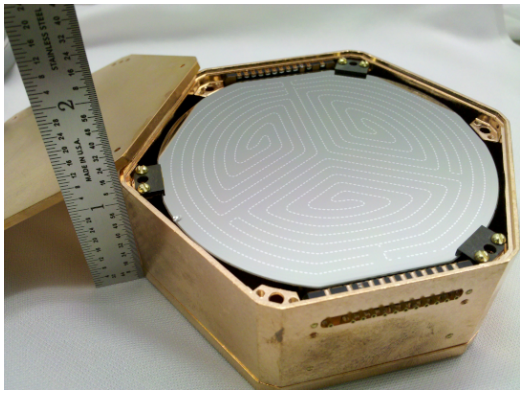

(b)

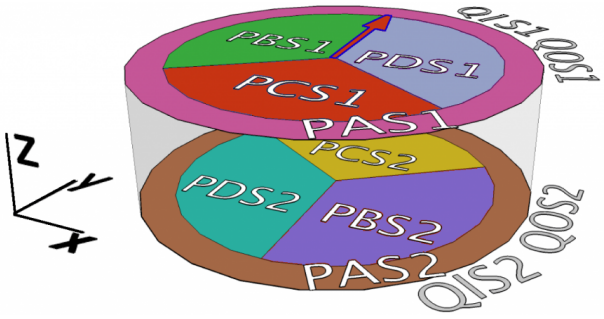

(c)

Figure 2.3: (a) SuperCDMS detectors stacked in five towers, with each containing three germanium detectors [5]. (b) a single detector module inside a copper housing [5]. (c) a cartoon that shows the phonon and charge channels on each side of the detector [5].

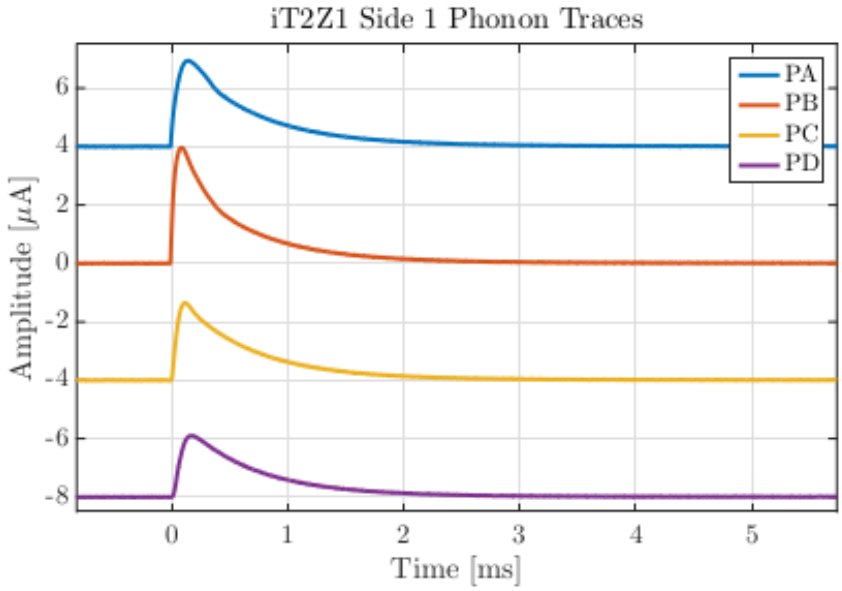

(a)

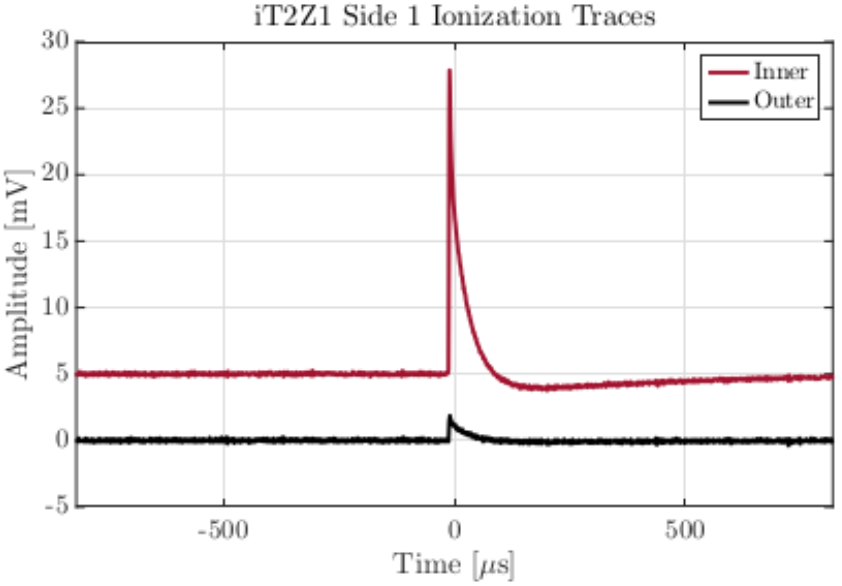

(b)

Figure 2.4: (a) Phonon output traces from the four channels on side 1 (top surface) of iT2Z1 for an example event [3]. For clarity, the amplitudes of the traces from the channels are vertically shifted by 4 nA. The traces from inner and outer ionization chanels of side 1 of iT2Z1 for an example event [3]. For clarity, the inner channel's trace is shifted upwards by 5 mV. See phonon and charge chanels in Fig. 2.3 (c).

as a positively charged particle called a "hole". The average energy required to create a single electron-hole pair in germanium is ~3.0 eV [7]. The initially-freed electrons, if carry sufficient momentum, can free more electrons creating a cascade. The charge carriers generated in nuclear recoils are fewer as compared to the same in electron recoils. The effect is called "quenching".

The bias voltage applied across the crystal drifts the freed electrons and holes towards the opposite faces of the detector. The ionization energy measured in the detector is given by

$$E_Q = N_{e/h}\epsilon, \tag{2.1}$$

where $N_{e/h}$ is the number of electron-hole pairs created in an interaction and ϵ is the average energy required to create a single electron-hole pair. For electron recoils, the recoil energy $E_r = E_Q$. For nuclear recoils, a quantity called "ionization yield" $Y(E_r)$ (< 1) accounts for the "quenching" such that-

$$E_Q = Y(E_r)E_r. \tag{2.2}$$

Therefore,

$$N_{e/h} = Y(E_r)E_r/\epsilon \tag{2.3}$$

The yield is used to discriminate between nuclear recoils and electron recoils:

$$\begin{aligned} Y(E_r) &= 1 \text{ for ERs, and} \\ &< 1 \text{ for NRs.} \end{aligned} \tag{2.4}$$

Ionization signals are detected in the sensors at the faces of the detector.

2.5 Phonon signal

The total phonons measured in the sensors comprise of a) primary phonons, b) Neganov-Trofimov-Luke (NTL) phonons [8, 9], and c) relaxation phonons. The mechanism through

which they are produced and the time of their creations are as follows.

Primary phonons are created at the interaction site when an incoming particle recoils of an electron or nucleus. The energy of the primary phonons, E_P, is given by-

$$E_P = E_r - N_{e/h}E_{gap}, \tag{2.5}$$

where E_r is the recoil energy, $N_{e/h}$ is the number of initial electron/hole pairs from the interaction, and E_{gap} is the bandgap energy.

The charge carriers created in the initial interaction drift through the detector crystal towards the electrodes of the detector. As the carriers traverse through the crystal, they reach a terminal velocity. The work done by the electric field on the charge carriers moving at terminal velocity is transferred to the lattice for phonon production. These phonons are called NTL phonons [8, 9]. The NTL phonon contribution, E_{NTL}, to the total phonon energy is:

$$E_{NTL} = eN_{e/h}V - E_{KE}, \tag{2.6}$$

where e is the charge of an electron, E_{KE} is the energy of the charge carriers and V is the bias voltage across the crystal.

As the charge carriers reach their respective electrodes, they recombine with their image charges, and energy is transferred to the lattice as relaxation phonons. The energy of relaxation phonons, E_{rel}, in an event is given by-

$$E_{rel} = N_{e/h}E_{gap} + E_{KE}. \tag{2.7}$$

The total phonon energy, E_T, is the sum of the primary, NTL, and relaxation phonon

energy:

$$\begin{aligned} E_T &= E_P + E_{NTL} + E_{rel} \\ &= (E_r - N_{e/h}E_{gap}) + (eN_{e/h}V - E_{KE}) + (N_{e/h}E_{gap} + E_{KE}) \\ &= E_r + eN_{e/h}V. \end{aligned} \tag{2.8}$$

The total phonon energy in the signal, after replacing the formula for the number of electron-hole pairs from Eqn. 2.3 into Eqn. 2.8, is given by-

$$E_T = E_r(1 + \frac{Y(E_r)eV}{\epsilon}). \tag{2.9}$$

Phonon signals are detected in the sensors at the faces of the detector.

2.6 Data processing

The raw data in the experiment primarily comprise of the traces from detectors' phonon and charge channels. The information of the initial interaction, most importantly the recoil energy was extracted from these raw traces. Each trace was processed by an Optimal Filter algorithm [10]. The OF algorithm models the signal trace ($S(t)$) as the sum of a scaled template and a Gaussian noise:

$$S(t) = a\,A(t - t_0) + n(t), \tag{2.10}$$

where $A(t - t_0)$ is the template with a time-delay parameter t_0, a is the amplitude, and n(t) is the Gaussian noise. The OF algorithm tries to fit $S(t)$ with the trace of an event, and a and t_0 are determined from the fit. The algorithm was run in the frequency domain where it determines, at each t_0 (scanned over a time-delay window), the best-fit amplitude and goodness-of-fit χ^2. The time-delay and amplitude corresponding to the lowest χ^2 value is considered as the global best-fit parameter. The amplitude primarily gives the energy information and the time-delay the position of an event in the detector.

There are a variety of OF algorithms used in SuperCDMS:

- **Standard Optimal Filter:** This is the most basic of all the OF algorithms where a signal template is fit to a trace. The algorithm is used on individual channel's traces and also on the combined trace of all channels.

- **Non-stationary Optimal Filter:** The phonon traces tend to have position-dependence that appears as fluctuations in nearly the first 100 μs of the signal [11]. The algorithm aims to deweight this portion in the χ^2 of frequency-domain-fits by treating the fluctuations as non-stationary noise. The algorithm is called the Non-stationary optimal filter (NSOF or NF) algorithm. The details of the algorithm can be found in Allison Kennedy's thesis [11]. Since the processing in NSOF is slower compared to the standard OF algorithm, the NSOF was applied only on the total phonon-trace from all channels. The data processing with NSOF provides better energy resolution over the OF algorithm. The NSOF is not useful to determine position information of the initial scattering.

- **Two Template Optimal Filter:** The NSOF algorithm loses position information from phonon traces of events. The position information is however necessary for the fiducialization of detectors. A two-template (2T) optimal filter algorithm was developed where the template encodes both the energy and position information of an event. The signal template ($s(t)$) in a 2T-fit algorithm is given by-

$$S(t) = \sum_{i=s,f} a_i A_i(t - t_0) + n(t), \tag{2.11}$$

where A_s is the standard OF template (slow fall-time) and A_f is a template with fast fall-time. The amplitudes of the slow and fast templates are a_s and a_f, respectively and $n(t)$ is the Gaussian noise. The OF template was subtracted from a collection of phonon traces and the average of the residual traces, after inverting those with negative

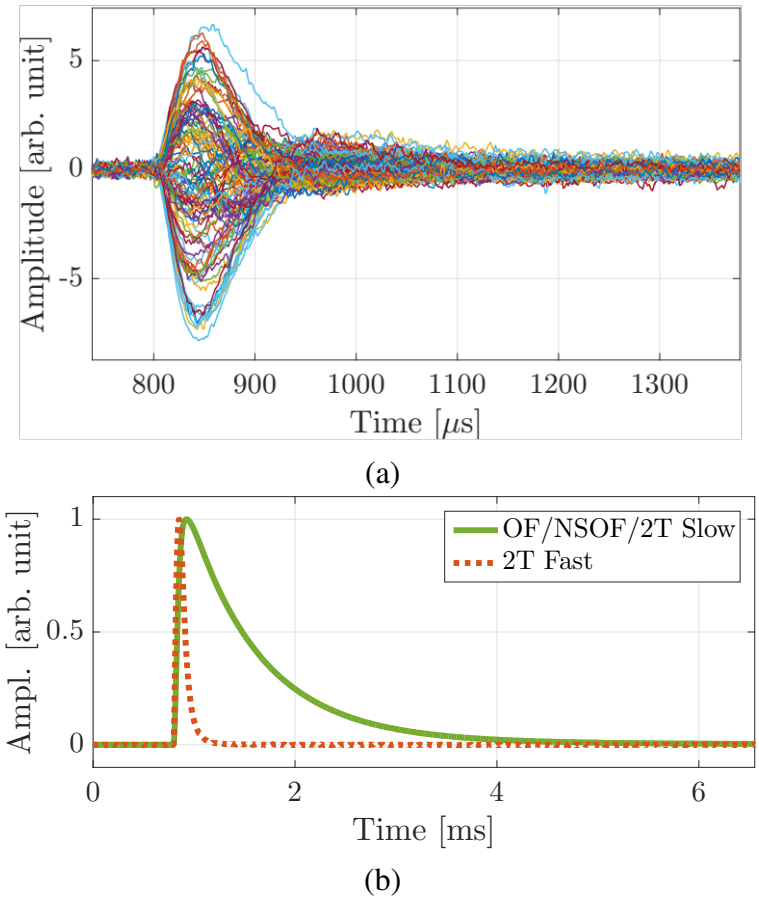

Figure 2.5: (a) Residual traces obtained from a collection of phonon traces [3]. (b) The slow template and the fast template obtained from residuals [4].

peaks, was considered as the fast template. Figure 2.5 (a) shows the residual traces, and Figure 2.5 (b) the slow and fast templates of 2T fit.

The algorithm was applied on traces of individual phonon channels as well as on the total phonon trace of an event. The 2T-fit returns four parameters: a) the amplitude of the slow template, b) the amplitude of the fast template, c) the time-delay (same for both templates), and d) χ^2 of the fit. The amplitude of the slow template provides the energy information and the relative amplitudes of the fast template between the channels are used to extract position information. The energy resolution from 2T-fit was comparable

to the same from NSOF, but the former provided slightly worse resolution.

- **Zero time-delay Optimal or Non-stationary Optimal Filter:** In SuperCDMS analyses, the distributions of energy-depositions from randomly triggered events (in short 'randoms') are treated as an estimate of noise in the detectors. The standard OF and NSOF algorithms are biased towards producing non-zero amplitudes for randoms and as a result, the distribution of energy deposition can have peaks away from 0 keV. To prevent this, the time-delay t_0 is fixed to zero in the OF fit of charge and phonon traces (OF0) and in the NSOF fit of phonon traces (NSOF0).

  For the CDMSlite Run 2 (the data used in the analysis presented in this thesis), NSOF algorithm was used on event traces with an additional 2T-fit based position correction [4]. To OF0/NSOF0 fit was applied on noise traces to determine noise energy distribution which was used for computing baseline resolution.

2.7 Data divisions

The data-taking period during which the cryogenics were stable is called a "Run". There were three SuperCDMS Runs; they are as follows:

- **Run 133:** March 2012 – July 2013.
- **Run 134:** July 2013 – July 2014.
- **Run 135:** September 2014 – November 2015.

There were also CDMSlite Runs (more detail will follow) that spanned parts of the above periods: the first during Run 133, the second during R134–135, and the third during Run 135.

The basic unit of stored data was a "data series" (or "series", for short). The length of a series was determined by how long the detectors could maintain sufficient neutralization for the full collection of the charge signal [12]. Each data series roughly lasts 3 hours. The data taken in SuperCDMS is classified into three categories:

- **Low-background or WIMP search:** The majority of the data taken were of this type to maximize the possibility of seeing signal events. No internal sources were placed near the detectors in this mode. The events recorded during this period could be physics events, but mostly due to the natural radioactivity of the apparatus and the detectors themselves.

- **^{133}Ba calibration:** ^{133}Ba decays to ^{133}Cs via gamma and conversion electron channels. The most prominent peaks from the decays are at 356.0, 81.0, 302.8, and 383.8 keV [13]. ^{133}Ba sources were placed inside the lead and polyethylene shields to use for electron recoil (ER) calibration and defining the ER band in the yield vs. recoil energy plane (see definition of "yield" in Section 2.4). On average, five ^{133}Ba data series per week were taken for SuperCDMS.

- **^{252}Cf calibration:** ^{252}Cf most of the time decays via alpha (α) emission which is followed by emission of gammas. However, it has a small probability, nearly 3 %, of undergoing spontaneous fission. The spontaneous fission of ^{252}Cf produces neutrons with energies up to 10 MeV with the most probable energy of neutrons at ~1 MeV [14]. A ^{252}Cf source was placed alternatively between the two source tubes (E and C stems of Fig. 2.2) for the nuclear recoil (NR) calibration and defining the NR band in the yield vs. recoil energy plane. To lower the neutron activations of the detectors, the ^{252}Cf calibration data were taken only a few times per calendar year. The activation peaks are used for the energy scale calibration of the CDMSlite data [4].

2.8 CDMSlite

The high-bias-voltage operation of iZIP detectors was explored in some SuperCDMS runs. The NTL phonon contribution to the total phonon energy (see Eqn. 2.9) linearly increases with the applied bias voltage and also is directly proportional to the number of electron-hole pairs (see Eqn. 2.8) created by the initial recoil. The number of pairs is related to the ionization energy of the event by $N_{e/h} = E_Q/\epsilon$. In other words, the application of high bias voltage amplifies the ionization signal by producing more NTL phonons as compared to the standard operation of the detectors. This enables the detector to measure very small energy recoils. The high-bias-voltage mode of operating iZIP detectors is called CDMS low ionization threshold experiment (CDMSlite).

In the CDMSlite mode, the detector was biased with a voltage of ~50–80 V [4], where one side of the detector was grounded and a negative bias was applied on the other side. The CDMSlite mode although provides a very small threshold (~56 eV in CDMSlite Run 2 [4]) for measuring energy depositions in the detector, loses the ability to discriminate between electron-recoil and nuclear-recoil events [3, 4].

There were three CDMSlite Runs; the data taken in the first Period of the second CDMSlite run was used in the LIPs search analysis presented in this thesis. The energy calibration and resolution of the data taken are described below.

- *Energy calibration:* The filtering algorithms described in Section 2.6 return amplitudes in units of volts (for charge channel traces) or amperes (for phonon channel traces). A calibration to convert amplitude to recoil energy in physical units (e.g keV) is crucial for the analysis. This requires peaks at known recoil energies from a known source. The electron capture peaks, which are ERs, following the ^{252}Cf calibration for NR (see Section 2.7) were used for this purpose. The energy scale for CDMSlite is calculated in

electron equivalent energy units (keV_{ee}) where it is assumed that all events are ERs with $Y(E_r) = 1$.

The neutron capture by a ^{70}Ge nucleus, during the calibration with ^{252}Cf neutron source, produces unstable ^{71}Ge with a half-life of 11.4 days. The ^{71}Ge thus produced decays by electron capture into a ^{71}Ga nucleus. The vacancy created by electron capture shifts from lower shells to higher shells until the vacancy reaches the outermost shell and ^{71}Ga turns stable. The various transitions of electrons between orbitals of ^{71}Ga atom following the electron capture cause emission of X-rays and Auger electrons. The entire process can be symbolically expressed by Eqn. 2.12.

$$\begin{aligned} {}^{70}\mathrm{Ge} + \mathrm{n} &\longrightarrow {}^{71}\mathrm{Ge} \\ {}^{71}\mathrm{Ge} + \mathrm{e} &\longrightarrow {}^{71}\mathrm{Ga} + \nu_e \\ {}^{71}\mathrm{Ga} &\longrightarrow {}^{71}\mathrm{Ga} + \gamma\text{'s, e's} \end{aligned} \tag{2.12}$$

The amount of energy released in the process depends on the shell in which the electron is

Shell	Energy (keV)	Branching Ratio
K	10.37	87.6 %
L	1.30	10.5 %
M	0.16	1.78 %

Table 2.1: The energy and branching ratio of different electron capture peaks [15].

captured and is equal to the Ga binding energy for that shell. Table 2.1 shows the locations of various shell peaks in the energy-deposition distribution and their branching ratios. The K-shell and L-shell captures have high probabilities and are useful for calibration purposes. The energy scale was calibrated using the K-capture peak. The drift in both detector bias and cryostat base temperature with time caused this peak position to vary by 5—10 % over time. This along with two additional small residual shifts (~2.5 %) of unknown origin were observed and corrected [16].

Peak	Location [keV$_{ee}$]	Resolution [eV$_{ee}$]
Base line	0.0	9.7 ± 0.1
M shell	0.16	18.6 ± 4.2
L shell	1.30	31 ± 2
K shell	10.37	101 ± 1

Table 2.2: The baseline resolution and resolutions at locations of various electron-capture peaks [4].

- *Energy resolution:* The electron capture peaks at 10.37 keV$_{ee}$ (K shell), 1.30 keV$_{ee}$ (L shell), and 0.16 keV$_{ee}$ (M shell) were utilized to model the CDMSlite detector resolution. The energy is reconstructed using the filter algorithms described in Section 2.6. The baseline resolution is calculated using the distribution of noise (randomly-triggered) events where zero time-delay Non-stationary Optimal Filter (NSOF0) was used. This is because, the standard OF or NSOF when applied to noise traces, the algorithms tend to bias the fit toward nonzero amplitudes. This is undesirable for characterizing the baseline noise distribution; the time delay is therefore forced to be zero. Figure 2.6 shows the probability distribution function (PDF) and the cumulative distribution function (CDF) of noise events in Run 2. The energy difference between the two vertical purple dashed lines at 84.13th and 15.87th percentiles is considered as the baseline resolution. The baseline resolution following this procedure is found to be 9.25 ± 0.11 eV$_{ee}$. The K, L, and M-shell peaks are then fitted with Gaussians, and resolutions (1σ) at the peak locations are determined from the fits; The NSOF algoritm is used to estimate energies. Table 2.2 shows the resolutions of the baseline noise and electron capture peaks.

  The resolution as a function of recoil energy was modeled as

$$\begin{aligned}\sigma_T &= \sqrt{\sigma_E^2 + \sigma_F^2(E_{r,ee}) + \sigma_{PD}^2(E_{r,ee})} \\ &= \sqrt{\sigma_E^2 + BE_{r,ee} + (AE_{r,ee})^2},\end{aligned} \tag{2.13}$$

  where σ_E is the baseline resolution caused by electronic noise, σ_F is the resolution due to

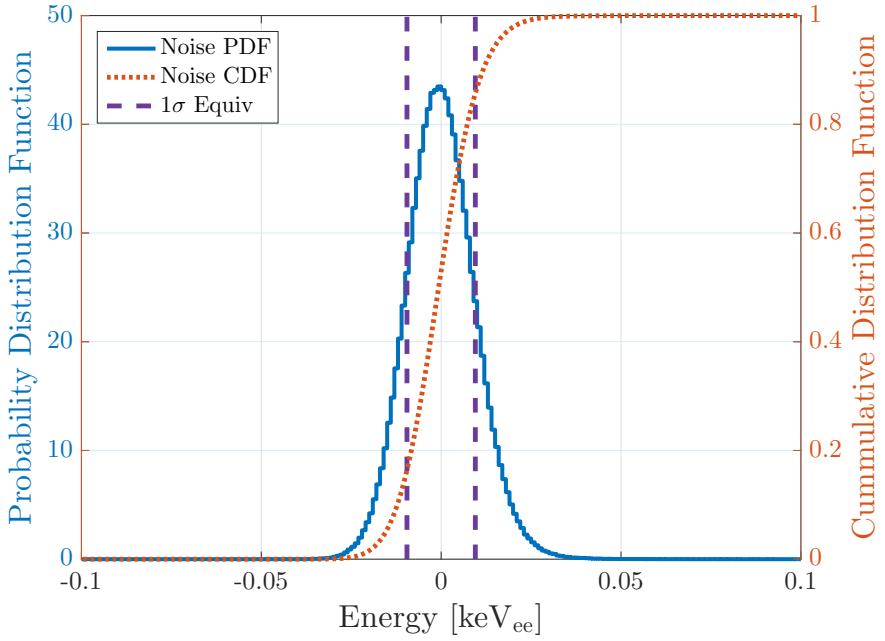

Figure 2.6: Probability distribution function of recoil energy (PDF) calculated with randomly-triggered (noise) events. The cumulative distribution function (orange dotted curve) was also calculated and shown on the right axis.

Fano statistics and $\sigma_{PD}(E)$ is the resolution due to position dependence of events. While σ_E is independent of energy, the other two terms of the resolution model are energy dependent and are described below.

The variance in the number of electron-hole pairs created in an event, assuming a Poisson distribution, is given by $\sigma_N = \sqrt{N_{e/h}}$. U. Fano [17] found a deviation from this number such that $\sigma_N = \sqrt{FN_{e/h}}$. The factor F is called "Fano factor". For an electron recoil, the recoil energy $E_{r,ee} = N_{e/h}\epsilon$. Therefore, the resolution in energy due to fluctuation in the number of charge-carriers produced in an ER is given by

$$\sigma_F^2 = \sigma_N^2\epsilon^2 = FE_{r,ee}\epsilon \tag{2.14}$$

The position dependence is taken into consideration in the resolution model as $\sigma_{PD}^2 = (AE_{r,ee})^2$. This term also includes other effects on the resolution that scales with energy.

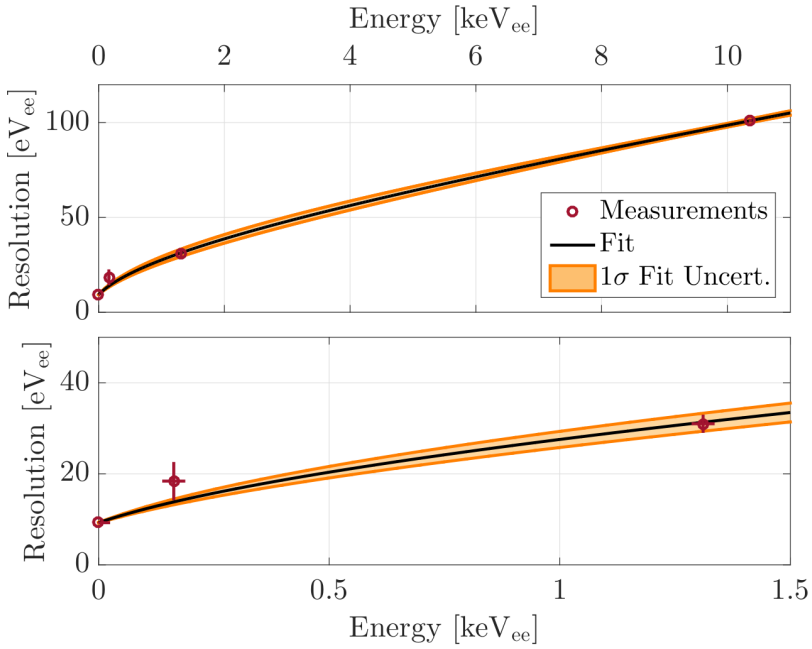

Figure 2.7: The resolution at four energy-points, the best-fit curve, and the 68 % uncertainty band on resolution at various energies [4]. The bottom panel shows resolution below 1.5 keVee.

The resolution determined at four energies, zero energy (baseline resolution) and K, L, M-shell peaks, are fitted with the resolution model of Eqn. 2.13. The fit is shown in Fig. 2.7.

2.9 Summary

SuperCDMS is a direct-detection dark matter search experiment at the Soudan mine in Minnesota, USA. The earth's overburden (~2090 m.w.e) above the experimental cavern shields cosmogenic muon flux by a factor of 5×10^4 relative to the flux at the surface. SuperCDMS uses muon-veto panels to tag cosmic muons that still can reach the detectors and also layers of shielding to stop other cosmogenic and radiogenic backgrounds such as

the neutrons and gammas from the cavern rock. The shielding includes an array of muon-veto panels to identify muon-coincident events, a polyethylene layer (40 cm) to moderate neutrons, lead layers (natural plus ancient lead of total 22.5 cm thickness) to shield gammas, and another polyethylene layer (10 cm) to shield neutrons from previous layers. There were forty veto panels, each with a 5 cm thick Bicron BC-408 ($H_{11}C_{10}$) plastic, connected to photomultiplier tubes (PMTs). The panels are overlapped in a fashion that prevents any direct line-of-sight to the detectors placed inside. Inside the veto panels, there are 40 cm thick polyethylene bricks to moderate neutrons. Two layers of lead (natural lead and "ancient lead") with a total thickness of 22.5 cm, inside the polyethylene layer, were used to shield gammas. The ^{210}Pb isotopes are found in the natural lead. The decay product of this isotope can create bremsstrahlung which could be a source of electromagnetic background. The ancient lead, on the other hand, is depleted of ^{210}Pb. A layer of ancient lead with a thickness of 4.5 cm was used after the natural lead layer to shield against the bremsstrahlung. After the lead layers, there was another layer of polyethylene of thickness 10 cm to shield neutrons that are produced in the outer polyethylene and lead layers. A layer of mu-metal (81 % Ni, 19 % Fe) with 0.381 mm thickness was used inside the inner polyethylene layer to block any magnetic fields that could interfere with detector electronics operations. The detectors were placed inside the shielding.

The experiment employed fifteen germanium detectors stacked in five towers. The detectors use (interleaved) ionization and phonon sensors to detect the respective signals from particle interactions inside the detector; they are called interleaved Z-sensitive Ionization and Phonon detectors (iZIPs). The phonon sensors consist of Quasiparticle-trap-assisted Electrothermal-feedback Transition-edge-sensors (QETs) which are affixed to a flat surface of the detector. The QETs consist of aluminum fins which are connected to strips of tungsten. The detector is cooled such that the aluminum (T_c = 1.2 K) and tungsten (T_c ~80 mK)

are superconducting, with the tungsten being held at its conduction/superconducting transition. The ionization signal is read out through a Junction gate Field-Effect Transistor (JFET). While the phonon signals were digitized at a rate of 0.625 MHz (1.6 μs per sample), the ionization signals were digitized at a rate of 1.25 MHz (0.8μs per sample). The measured ionization and phonon signals in iZIPs were used to discriminate between electron and nuclear recoils by defining a quantity called "ionization yield" which is the ratio of ionization energy to the recoil energy in an event. The discrimination with yield was used to reduce backgrounds in the measured data. The iZIPs were typically operated with a bias voltage of ~4 V where the yield-based discrimination is very efficient. The high bias voltage (~50–80 V [4]) mode of operation of iZIPs was also explored. In this mode, the detectors cannot discriminate between electron and nuclear recoils. However, this high-bias-voltage mode of operating iZIP detectors, called the CDMSlite, enabled the detectors to measure very small energy recoils. For example, the energy threshold achieved in the second CDMSlite Run was ~56 eV_{ee} [4].

The raw data in the experiment primarily comprises of the traces from detectors' phonon and charge channels. The traces are processed with Optimal Filter algorithm where a signal template is fitted with the event traces. The amplitudes of the traces returned from the OF-fit are calibrated to energy. The goodness-of-fit χ^2 from the fit determined if the trace is significantly different from the signal template i.e the event is non-physical. The energy scale calibration of CDMSlite was determined by using the electron capture peaks of ^{71}Ga following the ^{252}Cf calibrations. The energy resolution was modeled using the noise distribution and resolutions of the electron capture peaks. The resolution model comprises of energy-independent baseline resolution, and two energy-dependent components. The energy-dependent resolutions are due to the fluctuation in the number of electron-hole pairs created in an event, and due to position-dependence of events and other detector effects.

The CDMSlite Run 2 Period 1 data after calibration is used for the LIPs search analysis presented in this thesis. The resolution model is used to smear the expected energy deposition distributions of LIPs and the background-model-spectra. The analysis will be discussed later in this thesis.

Bibliography

[1] D.G. Michael, P. Adamson, T. Alexopoulos, et al. "The magnetized steel and scintillator calorimeters of the MINOS experiment". *Nuclear Instruments and Methods in Physics Research Section A: Accelerators, Spectrometers, Detectors and Associated Equipment* 596.2 (2008), 190–228.

[2] D. S. Akerib et al. "First results from the cryogenic dark matter search in the Soudan Underground Lab". *Phys. Rev. Lett.* 93 (2004), 211301. arXiv: astro-ph/0405033.

[3] Mark David Pepin. "Low-Mass Dark Matter Search Results and Radiogenic Backgrounds for the Cryogenic Dark Matter Search". PhD thesis. Minnesota U., 2016.

[4] R. Agnese et al. "Low-mass dark matter search with CDMSlite". *Phys. Rev. D* 97.2 (2018), 022002. arXiv: 1707.01632 [astro-ph.CO].

[5] D'Ann Rebekah Barker. "SuperCDMS Background Models for Low-Mass Dark Matter Searches". PhD thesis. Minnesota U., 2018.

[6] Kyle Michael Sundqvist. "Carrier Transport and Related Effects in Detectors of the Cryogenic Dark Matter Search". PhD thesis. UC, Berkeley, 2012.

[7] S.O.W. Antman, D.A. Landis, and R.H. Pehl. "Measurements of the Fano factor and the energy per hole-electron pair in germanium". *Nuclear Instruments and Methods* 40.2 (1966), 272–276.

[8] B. S. Neganov and V. N. Trofimov. "Colorimetric method measuring ionizing radiation". *Otkryt. Izobret.* 146 (1985), 215.

[9] P. N. Luke. "Voltage-assisted calorimetric ionization detector". *Journal of Applied Physics* 64.12 (1988), 6858–6860. eprint: https://doi.org/10.1063/1.341976.

[10] Sunil Ramanlal Golwala. “Exclusion limits on the WIMP nucleon elastic scattering cross-section from the Cryogenic Dark Matter Search”. PhD thesis. UC, Berkeley, 2000.

[11] Allison Blair Kennedy. “SuperCDMS Prototype Detector Design and Testing”. PhD thesis. Minnesota U., 2017.

[12] B. Serfass. *R133 data quality summary*. SuperCDMS Internal note, Run 133-135 Analysis. 2012.

[13] A. Sonzogni. *NuDat 2.7*. http://www.nndc.bnl.gov/nudat2/. 2018.

[14] M. Divadeenam and J.R. Stehn. “A least-squares fit of thermal data for fissile nuclei”. *Annals of Nuclear Energy* 11.8 (1984), 375–404.

[15] W. Bambynek, H. Behrens, M. H. Chen, et al. “Orbital electron capture by the nucleus”. *Rev. Mod. Phys.* 49 (1 1977), 77–221.

[16] R. Agnese, A. J. Anderson, T. Aramaki, et al. “New Results from the Search for Low-Mass Weakly Interacting Massive Particles with the CDMS Low Ionization Threshold Experiment”. *Phys. Rev. Lett.* 116 (7 2016), 071301.

[17] U. Fano. “Ionization Yield of Radiations. II. The Fluctuations of the Number of Ions”. *Phys. Rev.* 72 (1 1947), 26–29.

Chapter 3

Simulation framework for LIPs

In experiments to search LIPs through direct detection, it is important to know the expected Probability Distribution Function (PDF) of energy deposition as LIP-flux passes through the detector. A framework to model energy loss by LIPs in typical detector materials (e.g. Ge, Si) has been developed within GEANT4 simulation setup [1, 2] and is used to calculate PDFs of energy deposition in the SuperCDMS detector for different (fractional) charge, mass and velocity of the particle. To build a simulation setup for LIP in GEANT4, it is required to have a definition for LIP as a particle in GEANT4, and a "physics list" in which physics processes that the particle has to follow, while passing through the detector material can be specified. This chapter starts by describing the motivation, in Section 3.1, to have such a framework in GEANT4. The physics modeling (writing LIP definition and "physics list") of LIPs is discussed in Section 3.2, and its validation in Section 3.3. The results from the simulation is discussed in Section 3.4. The chapter ends with a conclusion in Section 3.5.

All the studies that have been done in this thesis are for a germanium detector but the results obtained from it can be extended for many other typical detector materials.

3.1 Motivation

Simulation is an important tool to characterize signals and backgrounds from their interactions with the detector material and therefore is used in all areas of experimental physics. While there are many simulation toolkits, such as GEANT4 [1], FLUKA [3], and MCNP [4], available to model energy loss of standard particles, none include LIPs. This makes the LIP signal modeling very challenging, and experiments are to rely on PDFs that are calculated solely from theoretical techniques. However, it is widely known that a Monte Carlo program calculates energy loss better than any other method [5]. A standard framework to perform simulations for LIPs can serve as an important tool.

GEANT4 is the most commonly used open-sourced toolkit to simulate passage of particles through matter. The physics models of GEANT4 undergoes many systematic and extensive validation tests [6–9] resulting in a great degree of reliability among researchers. Moreover, the toolkit comes with a range of functionalities for easy inclusion in a simulation setup through its "object-oriented" programming design: it allows users to define geometries of any experimental setup with a range of choices of materials involved, offers a wide choices for fundamental particles of interest, choices of physics processes and models, and tracking through materials, etc. A detailed description of different functionalities of GEANT4 can be found from Ref. [1]. The potential of the toolkit in simulating energy loss has been utilised in many experiments starting from low energy nuclear physics to high energy particle physics experiments with a very wide range of detector materials. The success of the toolkit inspires its use in simulations for LIPs as well. With the introduction of LIPs in GEANT4, where all other standard particles are already defined, energy loss simulations can be brought into a common framework. The simulation framework will facilitate future LIP-search experiments, which include both SuperCDMS SNOLAB and

other direct detection experiments, with a tool to calculate energy loss as well as detection efficiencies of LIPs under different experimental configurations.

For the LIP-search analysis reported in this thesis, the simulation framework serves two major purposes: a) calculation of energy deposition distributions for LIP-interactions with the SuperCDMS detector and b) estimation of corrections to LIP selection efficiencies. They will be discussed in subsequent chapters.

3.2 Physics modeling

The modeling of energy loss involves two major parts, one being the definition of the particle in GEANT4 [1], and the other being the writing of a physics list to specify physics processes. The GEANT4 version 10.02 [10] is used to model energy loss of LIPs.

3.2.1 LIPs definition

Positively and negatively charged LIPs are defined in separate classes, which take the desired charge and mass as arguments. In the particle definition, LIPs are assumed to have mostly the same properties as muons. They differ from muons because of their fractional charges and masses and also unlike muons, they do not decay. The class for a positively charged LIP is given in Appendix 3.A.

3.2.2 Physics list

Since LIPs are charged particles, they are expected to participate in electromagnetic interactions. The known particles which could be closest to LIPs are Minimum Ionizing Particles (MIPs). Cosmic ray muons travel at relativistic speeds at sea level, and are typically MIPs. The energy loss of LIPs is modeled in close similarity with muons since cosmic muons,

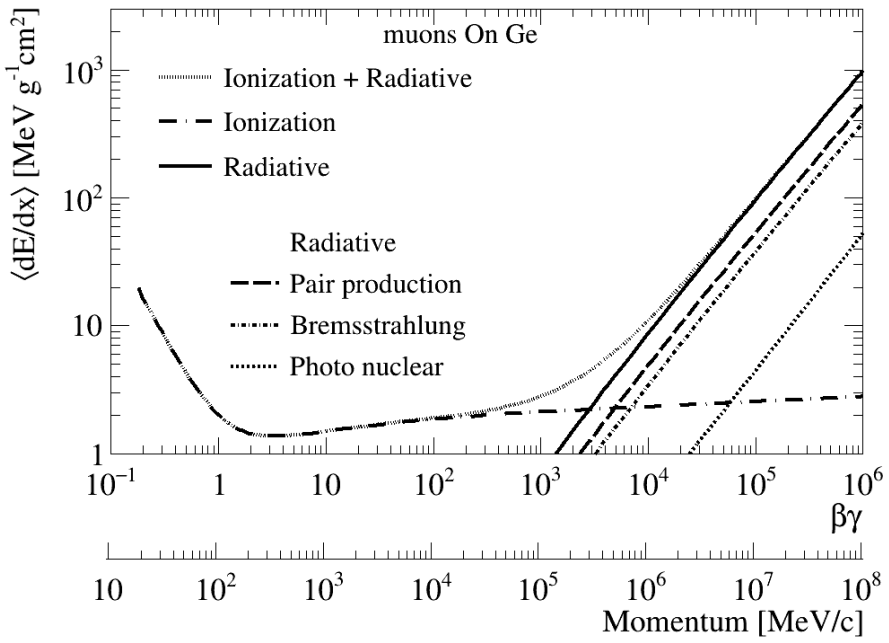

Figure 3.1: Stopping power of muons as a function of momentum (or $\beta\gamma$) in germanium [2]. Contribution in stopping power from different processes has been shown. Data for the stopping power contributions from different processes are taken from [11].

much like LIPs, lose a small amount of energy in any detector. Figure 3.1 shows the stopping power of muons in a germanium detector. The figure shows the contribution of energy loss from ionization, bremsstrahlung, pair-production and photo-nuclear processes at different incident momenta of muons. The momentum of the particle is expressed in terms of $\beta\gamma$. Ionization is found to be the dominant process in the low momentum region, whereas in the high momentum region pair-production and bremsstrahlung dominate over ionization and photo-nuclear. In the current simulation framework, all the energy loss processes for muons are included in the physics list of LIPs, except photo-nuclear as it has a negligible contribution in the high momentum region. The physics processes and models used for LIPs are given in Table 3.1. There are two choices for ionization energy-loss simulation are provided for LIPs: IonizationA with `G4ICRU73QO`, `G4BetheBloch` and `G4MuBetheBlochModel` or

IonizationB with `G4PAIModel`. The differences between IonizationA and IonizationB are: simulations with the former manifest "Barkas effect [11]" at low velocities ($\beta\gamma < 0.1$) and the later produces atmoic shell peaks (see Section 3.4) in the distributions of energy deposition. An advanced algorithm [12], where multiple-scattering `G4Wentzel-VI` and single-scattering `G4eCoulombScattering` models are simultaneously used, has been recently developed in GEANT4 for precision in simulation of lateral displacements of particle trajectories as they pass through the detector. This algorithm helps better estimate the actual amount of energy which will be measured, excluding the component of energy loss which escapes from a detector of finite size, in the detector. The same is used in the simulation.

GEANT4 provides a method to organize and incorporate physics processes as 'builders' or 'modules' into a physics list. A module for LIPs with the processes described in Table 3.1 is constructed. To simulate the secondaries generated by the interaction of LIPs, a standard module, `G4EmStandardPhysics` is used. This has been chosen as the secondaries of LIPs are expected to be known particles in PDG.

During the course of implementation, it was found that some default GEANT4 models hardcode the particle charge and mass, requiring the corresponding codes to be modified in order to calculate LIP energy loss. The list of modifications made to standard GEANT4 codes is given in Appendix 3.B.

3.3 Validation

After implementing all physics processes and models, simulations are performed with different LIP charges and masses, for a range of incident energies. For each incident energy, a large number of events ($\sim 10^8$) are simulated. $\mathrm{d}E/\mathrm{d}x$ from each event, where $\mathrm{d}E$ is the energy lost by the incident particle in traversing a path $\mathrm{d}x$, is calculated. $\mathrm{d}E/\mathrm{d}x$ is

Processes and models		
Process	**Model**	**Energy range**
IonizationA	`G4ICRU73QOModel`	0 - 0.2 MeV
	`G4BetheBlochModel`	0.2 MeV - 1 GeV
	`G4MuBetheBlochModel (LIPBetheBlochModel)`	1 GeV - 100 TeV
IonizationB	`G4PAIModel (LIPPAIModel)`	0 - 100 TeV
Pair production	`G4MuPairProductionModel (LIPPairProductionModel)`	0 - 100 TeV
Bremsstrahlung	`G4MuBremsstrahlungModel (LIPBremsstrahlungModel)`	0 - 100 TeV
Single Scattering	`G4eCoulombScatteringModel`	0 - 100 TeV
Multiple Scattering	`G4WentzelVIUniModel`	0 - 100 TeV

Table 3.1: Processes and Models used in simulation [2]. The models within the parentheses are adapted to include charge or mass dependence. The energy bounds for the `G4ICRU73QO` and `G4BetheBloch` models shown in the Table are for LIPs with mass 105.6 MeV/c^2 (mass of a muon). The energy-bounds need to be scaled by a factor (m_{LIP}/m_{μ}) for any other mass of LIPs.

averaged over a large number of events ($\sim 10^8$) and the average $\mathrm{d}E/\mathrm{d}x$ is used as stopping power at that incident energy. To ensure that $\mathrm{d}E$ is infinitesimal compared to the incident particle energy, an appropriate thickness of the detector is chosen. For example: LIPs with unit charge[1] show infinitesimal energy loss in a detector with 0.25 mm thickness, whereas for smaller fractional charges (below e/1000), they would show infinitesimal energy loss even for a 250 cm thick detector, since the probability of interactions gets suppressed as charge squared.

Energy loss simulation of LIP for different charge and mass is validated by comparing the stopping power ($\langle \mathrm{dE/d}x \rangle$) of LIPs to that of muons. Stopping power for all energy loss processes of charged particles is proportional to the square of electronic charge, the same is expected from LIPs. The mass dependence of stopping power for different processes follows from the respective cross section used by the physics processes. The $\langle \mathrm{dE/d}x \rangle$ from ionization does not depend on mass for a given $\beta\gamma$, nor does it for pair-production process, but for bremsstrahlung $\langle \mathrm{dE/d}x \rangle$ scales as the inverse square of mass when plotted as a

[1] Charge of LIPs is fractional. Unit charge is considered only for verification purposes.

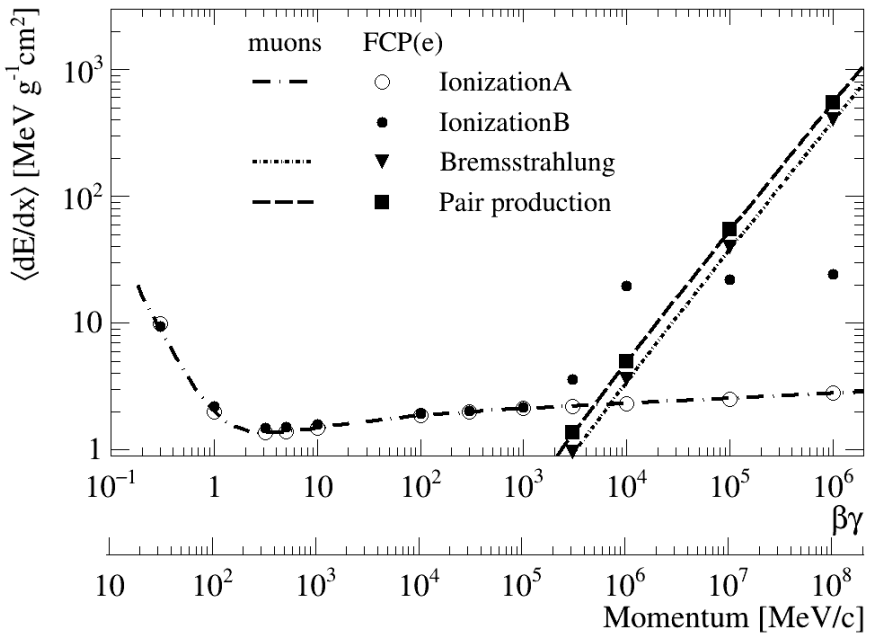

Figure 3.2: Comparison of stopping power of unit-charge LIPs and muons as a function of momentum (or $\beta\gamma$) [2]. Stopping power of muons are the same shown in Fig. 3.1. For LIPs, it is calculed for IonizationA, IonizationB, Pair production and Bremsstrahlung processes described in Table 3.1. Lines are for muons and markers are for LIPs with charge $+e$ and mass 105.6 MeV/c^2 (Muon mass).

function of energy.

Stopping power of LIPs is first calculated for LIPs with unit charge and for mass same as muons. The charge and mass are then varied to see departure of stopping powers from unit charge and muon mass. Figure 3.2 shows the comparison of stopping power due to Ionization (A & B), Bremsstrahlung and Pair-production energy loss of muons with that of LIPs with charge equal to $+e$ and mass 105.6 MeV/c^2 (Muon mass)(See also Fig. 3.1). The stopping powers for a fractional charge and different masses are shown in different panels of Fig. 3.3. Figure 3.3 (a) shows the stopping power of LIPs due to IonizationA with charge $+e/1000$ and masses 100 MeV/c^2 and 1 GeV/c^2, the same due to IonizationB is shown in Fig. 3.3 (b). Figure 3.3 (c) shows $\langle \mathrm{dE/d}x \rangle$ as a function of $\beta\gamma$ due to pair-production for

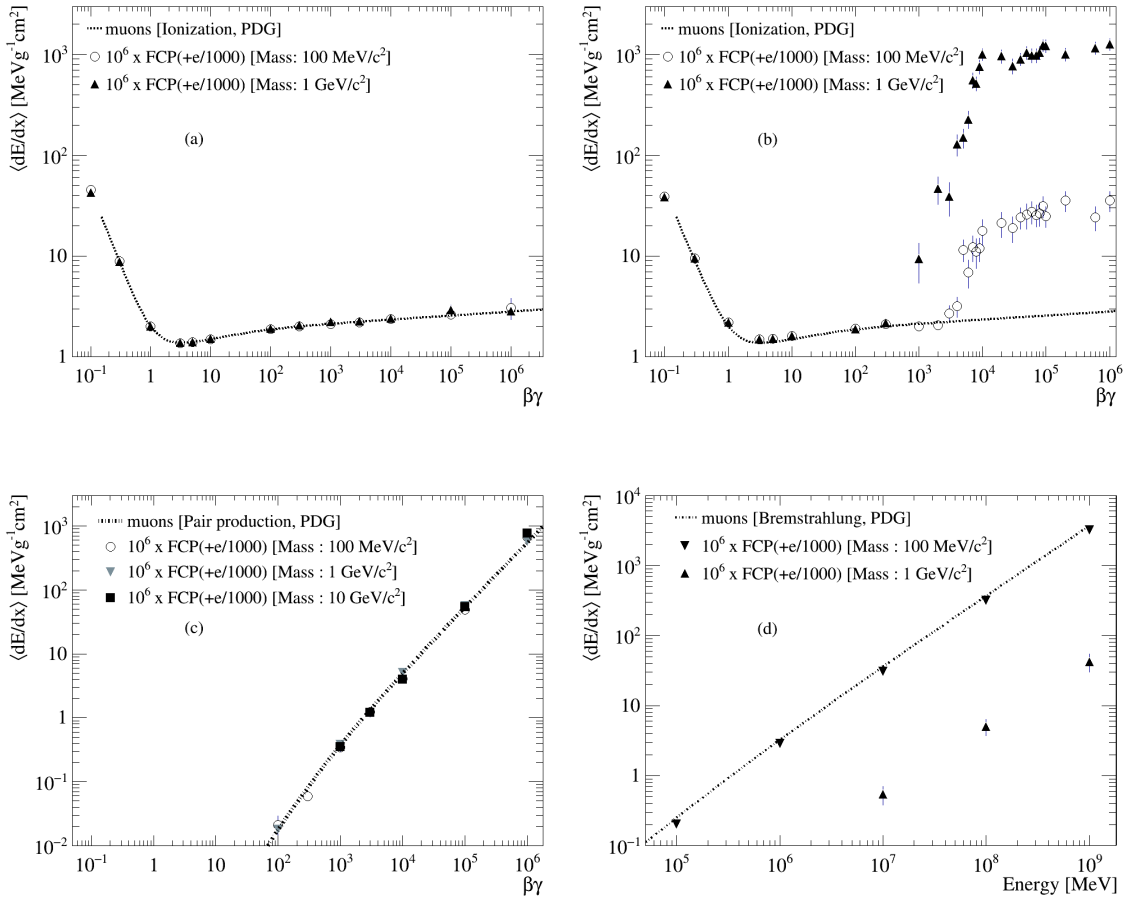

Figure 3.3: Comparison of stopping power of LIPs with that of muons for individual processes [2]. To show the charge dependence, $\langle dE/dx \rangle$ is scaled by the inverse of charge squared. (a) and (b) show stopping power due to IonizationA and IonizationB as a function of incident $\beta\gamma$, respectively. (c) shows stopping power due to pair-production as a function of incident $\beta\gamma$ and (d) shows the same as a function of incident energy due to bremsstrahlung process. The points with error bars shown in the plots are from simulation and the error bars are statistical.

LIPs with charge $+e/1000$ and with masses 100 MeV/c^2, 1 GeV/c^2 and 10 GeV/c^2. The results show the simulation respects charge and mass dependence. Figure 3.3 (d) shows $\langle \mathrm{dE/d}x \rangle$ due to bremsstrahlung of LIPs with charge $e/1000$ and masses 100 MeV/c^2 and 1 GeV/c^2 at different incident energies. It can be seen that the charge and mass dependence is also respected in energy loss due to the bremsstrahlung process.

On further investigation of Fig. 3.3 (b), it is found that the large values of $\langle \mathrm{dE/d}x \rangle$ in the figure is a result of a few very high energy loss (of the order of few GeV) events from the distribution of energy loss. Figure 3.4 (a) shows comparison of cumulative stopping power due to IonizationB as a function of energy loss for $\beta\gamma$ of 10^2 and 10^4. It can be seen that when energy losses above ~1 GeV are included, the $\langle \mathrm{dE/d}x \rangle$ for $\beta\gamma$ of 10^4 becomes larger as compared to that for $\beta\gamma$ of 100 which implies that the rapid rise in the $\langle \mathrm{dE/d}x \rangle$ is because of some high energy loss events. On the other hand, a large part of the distribution lies in the small energy loss region. If events with energy loss above 1 GeV are removed from the distributions of energy loss for $\beta\gamma$ above 100, the resulting stopping power shows expected values as shown in Fig. 3.4 (b). For experiments that are sensitive to energy losses below a certain upper energy threshold (below 1 GeV), IonizationB can also be used to generate distributions of energy deposition.

3.4 Results

As described in Section 3.3, the physics processes individually give correct energy loss (IonizationB correct up to 1 GeV). Therefore, they all can be used together to calculate quantities like distribution of energy deposition for different charges and masses of LIPs in various detector materials. This section presents the energy deposition distributions in the germanium detector calculated for SuperCDMS detector-dimensions with diameter 7.6 cm

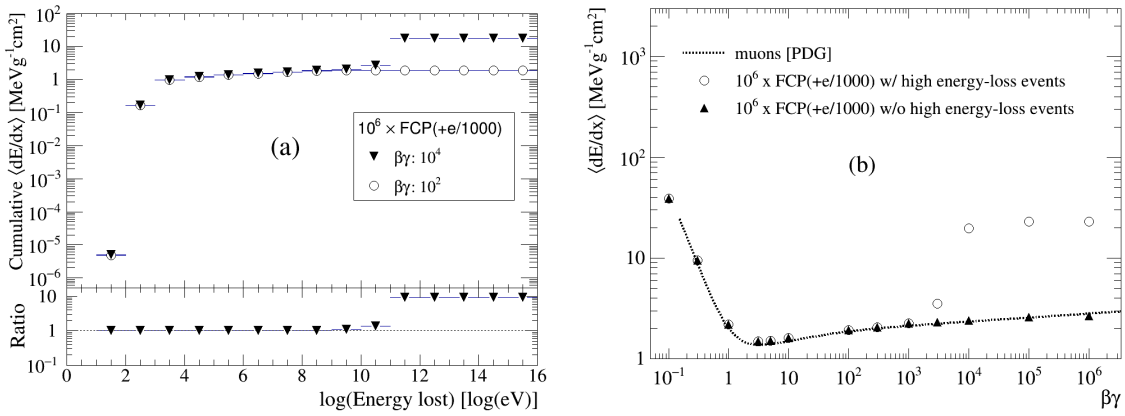

Figure 3.4: (a) Comparison of cumulative $\langle dE/dx \rangle$ due to IonizationB as a function of log (energy loss) for incident $\beta\gamma$ of 10^2 and 10^4 [2]. The top panel shows how $\langle dE/dx \rangle$ changes as we sucessively include more and more energy loss bins of the energy-loss spectrum to calculate stopping power and the bottom panel shows the ratio of the same for $\beta\gamma$ of 10^4 to $\beta\gamma$ of 10^2. (b) Stopping power due to IonizationB for LIPs with charge $+e/1000$ and mass 100 MeV/c^2 before and after removing very high energy-loss events. To show the charge dependence, $\langle dE/dx \rangle$ is scaled by the inverse of charge squared.

and thickness 2.5 cm. For simplicity, the distributions are calculated for normal incidence[2] of LIPs on the detector. Figure 3.5 shows the comparison of distributions with the two sets of ionization models for charge $+e/1000$ and $+e/50$; the mass for both is 100 MeV/c^2. It can be seen from Fig. 3.5 (a) that both IonizationA or IonizationB give similar energy depositions with the differences seen mostly in the form of atomic shell peaks, which are present in distributions with IonizationB but not with IonizationA. As the charge of particle is increased from $e/1000$ to $e/50$, increasing number of interactions in the detector, the atomic shell-peaks get smeared out; the same can be seen in Fig. 3.5 (b).

The probability distribution of energy deposition are further calculated for different charges and incident $\beta\gamma$ of the LIPs with IonizationB in the physics list. IonizationB model

[2]Cosmogenic LIPs falling on an actual detector may have some angular distributions. The energy deposition distributions for LIPs incidenting isotropically and also with a angular distribution of $\cos^2\theta$ type are also calculated, but not shown in the present chapter. They will be discussed in Chapter 4 while describing the LIPs-search analysis.

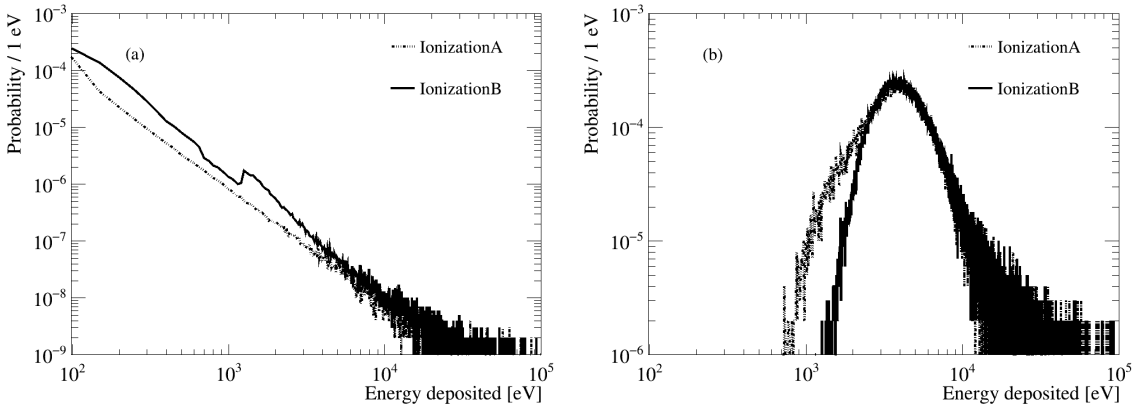

Figure 3.5: Probability distributions of energy depositions for normally incident LIPs with charge $e/1000$ (a) and charge $e/50$ (b) with IonizationA and IonizationB in the physics list [2]. Incident $\beta\gamma$ is 3.1 and mass is 100 MeV/c^2. The dash-dotted lines show distribution with IonizationA and the solid lines show the same with IonizationB.

is chosen as it preserves the atomic shell peaks in the energy deposition distributions. Figure 3.6 (a) shows the distributions for minimum ionizing LIPs with different charges of the particle. It can be seen that with the decrease in charge, probability also decreases. As particles with small velocity tend to interact more in a detector, the probability of interactions for small incident $\beta\gamma$ is expected to be very high. Figure 3.6 (b) shows that the probability decreases with increasing $\beta\gamma$ for LIPs with charges $+e/1000$ and mass 100 MeV/c^2.

The probability distributions obtained from GEANT4 are also compared with those published by CDMS II [13], where the distributions calculated in CDMS II use a convolution-based approach as discussed in Appendix 4.B. Figure 3.7 shows the comparison for minimum ionizing LIPs with charges $+e/6$, $+e/15$, and $+e/30$. GEANT4 probability distributions are calculated with IonizationA and IonizationB models. The distributions from CDMS II and GEANT4 are similar in shape, but peaks positions are slightly different from each other. Peaks corresponding to the most probable energy losses are at lower energies in GEANT4

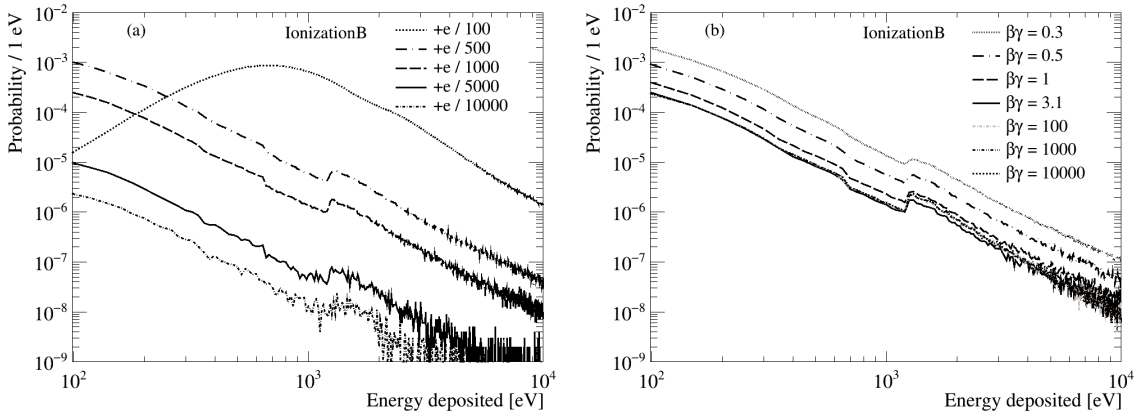

Figure 3.6: Probability distributions of energy depositions for LIPs with different charges (a) and different incident $\beta\gamma$ (b) [2]. IonizationB is used in the physics list. Incident $\beta\gamma$ is 3.1 and mass is 100 MeV/c^2.

when IonizationA is used and are at higher energies when IonizationB is used.

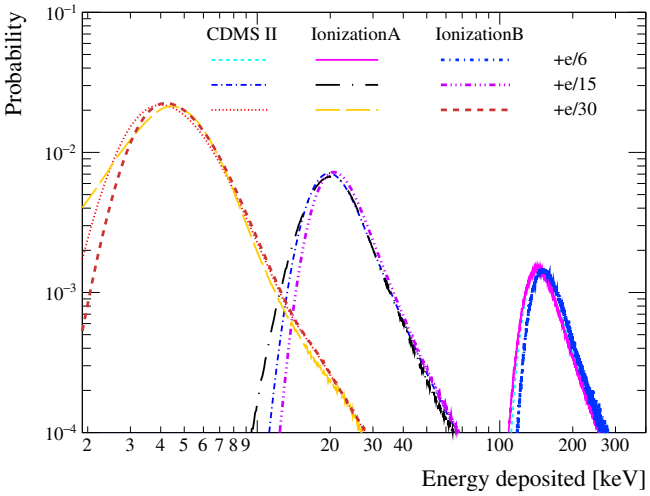

Figure 3.7: Probability distributions of energy deposition for LIPs with charge +e/6, +e/15 and +e/30 in a 1 cm Ge abosrber published by CDMS II [13] and in GEANT4 [2].

3.5 Conclusion

A GEANT4 framework to study the energy loss of LIPs in typical detector materials has been developed. Definitions of positively and negatively charged LIP are introduced in GEANT4 to perform simulations and calculate energy loss in any desired simulation geometry. A set of physics processes and models encapsulated in a physics list are validated. The list includes two set of ionization models, defined in Table 3.1 as IonizationA and IonizationB, and models for bremsstrahlung and pair-production energy losses. IonizationA shows correct average energy loss per unit length for all incident energies but it fails to produce the expected atomic shell structures in the distribution of energy deposition. IonizationB, on the other hand, produces atomic shell peaks very accurately in the distributions but at high incident $\beta\gamma$, the average energy loss per unit length are larger than the expected values. However, it is also noted that the large values of average energy loss per unit length for IonizationB is due to the presence of a few very high energy loss (of the order of few GeV) events in the distribution of energy loss. If these few events are neglected, the stopping powers become the same as the expected values. Atomic shell peaks are features visible in the energy deposition distributions of LIPs with small fractional charges; the peaks get smeared by many interactions in the detector if the charge of LIPs are larger. Therefore, IonizationB should be used for small fractional charges whereas both IonizationA and IonizationB can be used for large fractional charges of LIPs.

Being a Monte Carlo Simulation, the framework facilitates finding the physical location of events in a detector and therefore can be used to calculate detection efficiencies. Since both primaries as well as secondaries are tracked in any typical GEANT4 simulation, it allows calculating energy loss by the primary LIPs and also the amount of energy which actually gets deposited in the detector.

The simulation framework is now publicly available on `GitHub` [2, 14].

Bibliography

[1] S. Agostinelli et al. “Geant4–a simulation toolkit”. *Nuclear Instruments and Methods in Physics Research Section A: Accelerators, Spectrometers, Detectors and Associated Equipment* 506.3 (2003), 250 –303.

[2] S. Banik, V.K.S. Kashyap, M.H. Kelsey, et al. “Simulation of energy loss of fractionally charged particles using Geant4”. *Nuclear Instruments and Methods in Physics Research Section A: Accelerators, Spectrometers, Detectors and Associated Equipment* 971 (2020), 164114.

[3] Giuseppe Battistoni, Till Boehlen, Francesco Cerutti, et al. “Overview of the FLUKA code”. *Annals of Nuclear Energy* 82 (2015). Joint International Conference on Supercomputing in Nuclear Applications and Monte Carlo 2013, SNA + MC 2013. Pluri- and Trans-disciplinarity, Towards New Modeling and Numerical Simulation Paradigms, 10 –18.

[4] Los Alamos Scientific Laboratory. Group X-6. *MCNP : a general Monte Carlo code for neutron and photon transport*. Manual.;Issued November 1979.;Includes bibliographical references. Los Alamos, N.M. : Dept. of Energy, Los Alamos Scientific Laboratory ; [Springfield, Va.] : [for sale by the National Technical Information Service], 1979., 1979.

[5] Hans Bichsel. *Rev. Mod. Phys.* 60 (3 1988), 663–699.

[6] H Wenzel, J Yarba, and A Dotti. “The Geant4 physics validation repository”. *Journal of Physics: Conference Series* 664.6 (2015), 062066.

[7] K. Amako, S. Guatelli, V. Ivanchencko, et al. “Geant4 and its validation”. *Nuclear Physics B - Proceedings Supplements* 150 (2006). Proceedings of the 9th Topical Seminar on Innovative Particle and Radiation Detectors, 44 –49.

[8] Julia Yarba. “Recent Developments and Validation of Geant4 Hadronic Physics”. *Journal of Physics: Conference Series* 396.2 (2012), 022060.

[9] Sunanda Banerjee. “Validation of Geant4 hadronic physics models at intermediate energies”. *Journal of Physics: Conference Series* 219.3 (2010), 032002.

[10] https://geant4-userdoc.web.cern.ch/UsersGuides/InstallationGuide/BackupVersions/V10.2/fo/BookInstalGuide.pdf.

[11] Donald E. Groom, Nikolai V. Mokhov, and Sergei I. Striganov. *Atom. Data Nucl. Data Tabl.* 78 (2001), 183–356.

[12] V N Ivanchenko, O Kadri, M Maire, et al. *Journal of Physics: Conference Series* 219.3 (2010), 032045.

[13] R. Agnese, A. J. Anderson, D. Balakishiyeva, et al. *Phys. Rev. Lett.* 114 (11 2015), 111302.

[14] https://github.com/SamirBanik/FCP_Simulation. 2019.

Appendix 3.A Source code of LIPs definition in GEANT4

The GEANT4 definition of a positively charged LIP is given below [2].

```
#include "G4LIPPlus.hh"
#include "G4PhysicalConstants.hh"
#include "G4SystemOfUnits.hh"
#include "G4ParticleTable.hh"

// ########################################################################
// ###                          LIPPLUS                                 ###
// ########################################################################
G4LIPPlus* G4LIPPlus::theInstance = 0;

G4LIPPlus* G4LIPPlus::MakeLIPPlus(G4double charge, G4double mass)
{
  if (theInstance) return theInstance;
  const G4String name = "LIP+";
  // search in particle table]
  G4ParticleTable* pTable = G4ParticleTable::GetParticleTable();
```

```
  G4ParticleDefinition* anInstance = pTable->FindParticle(name);

  if (anInstance ==0)
  {
  // create particle
  //
  //    Arguments for constructor are as follows
  //               name             mass          width         charge
  //             2*spin           parity  C-conjugation
  //          2*Isospin       2*Isospin3       G-parity
  //               type    lepton number  baryon number   PDG encoding
  //             stable         lifetime    decay table
  //             shortlived      subType    anti_encoding
  anInstance = new G4ParticleDefinition(
                                       name, mass, 0,  +fabs(charge)*eplus,
                                       1,               0,                0,
                                       0,               0,                0,
                                       "lepton",        -1,                0,        -90,
                                       true,             0,             NULL,
                                       false,           "LIP"
                                       );

  // Bohr Magnetron
  G4double muB =  0.5*eplus*hbar_Planck/(anInstance->GetPDGMass()/c_squared) ;
  anInstance->SetPDGMagneticMoment( muB * 1.0011659209);
  }
  theInstance = reinterpret_cast<G4LIPPlus*>(anInstance);
  return theInstance;
}
```

Appendix 3.B Modifications made to standard GEANT4 code

Source file: G4MuBetheBlochModel.cc		
Function	**Changes made**	**Remark**

ComputeCrossSectionPerElectron(const G4ParticleDefinition* p, G4double kineticEnergy, G4double cutEnergy, G4double maxKinEnergy)	//Lines added: G4double charge = p->GetPDGCharge()/eplus; G4double charge2 = charge*charge;
	
	//Multiplied charge^2 to crosssection: cross *= charge2* twopi_mc2_rcl2/beta2;
		Source and header files copied and renamed as LIPBetheBlochModel.cc and LIPBetheBlochModel.hh respectively

ComputeDEDXPerVolume(const G4Material* material, const G4ParticleDefinition* p, G4double kineticEnergy, G4double cut)	//Lines added: G4double charge = p->GetPDGCharge()/eplus; G4double charge2 = charge*charge; //Multiplied charge^2 to dedx: dedx *= charge2*twopi_mc2_rcl2* eDensity/beta2;	
Source file: G4MuBremsstrahlungModel.hh		
Function	**Changes made**	**Remark**

inline void LIPBremsstrahlungModel:: SetParticle(const G4ParticleDefinition* p)	//Lines added: charge = particle->GetPDGCharge();
	
	//Multiplied charge^2 to a coefficient: coeff = 16.*charge*charge*CLHEP:: fine_structure_const*cc* cc/3.;
		Source and header files copied and renamed as LIPBremsstrahlungModel.cc and LIPBremsstrahlungModel.hh respectively

Source file: G4MuPairProductionModel.cc		
Function	**Changes made**	**Remark**
ComputeDEDXPerVolume(const G4Material* material, const G4ParticleDefinition* pcl, G4double kineticEnergy, G4double cutEnergy)	//Lines added: G4double charge = pcl->GetPDGCharge(); //Multiplied charge^2 to dedx: dedx *= charge*charge;	Source and header files copied and renamed as LIPPairProductionModel.cc and LIPPairProductionModel.hh respectively
ComputeCrossSectionPerAtom(const G4ParticleDefinition* p, G4double kineticEnergy, G4double Z, G4double, G4double cutEnergy, G4double maxEnergy)	//Lines added: G4double charge = p->GetPDGCharge(); //multiplied charge2̂ to cross-section: cross *= charge*charge;	
Source file: G4MuMultipleScattering.cc		
Function	**Changes made**	**Remark**
InitialiseProcess(const G4ParticleDefinition*)	//Used G4WentzelVIModel in place of G4UrbanMscModel G4VEmModel* theModel = 0; theModel = new G4WentzelVIModel(); AddEmModel(0, theModel);	Source and header files copied and renamed as LIPMultipleScattering.cc and LIPMultipleScattering.hh respectively

Table 3.1: Table of code modifications [2].

Chapter 4

LIPs search in SuperCDMS

This chapter discusses the analysis to search for Lightly Ionizing Particles (LIPs) with the low energy threshold data acquired in the CDMSlite mode [1]. The CDMSlite operation of SuperCDMS detectors is described in Chapter 2. Along with the data, a signal model that describes the LIP interactions with the detector material is essential in a LIPs search analysis. The LIP signal model is simulation-based; the framework to perform simulations for LIPs is developed in this thesis, and is described in Chapter 3. In this chapter, the upper limits on intensity of LIPs are calculated from the comparisons of the data spectrum with the expected energy deposition distributions, obtained from the signal model for different values of charge, mass, and incident $\beta\gamma$ of the particle. The limit-setting framework is developed with the spectra generated from the CDMSlite Run 2 background model [2], where the energy-deposition distributions from the background model act as as the representative of the data.

This chapter begins with a description in Section 4.1 of the mathematical framework for the intensity limit calculation. This is followed by a discussion on the LIP signal model in Section 4.2, description of the data-set in Section 4.3, and discussion on event selection

and efficiencies of the selection cuts in Section 4.4. The expected sensitivity calculated with the background-model spectra is discussed in Section 4.5. The analysis of the data and the intensity limit results are discussed in Section 4.6 and Section 4.7, respectively. Finally, the chapter ends with a conclusion in Section 4.8.

4.1 Mathematical framework

The intensity-limit calculation for LIPs requires the knowledge of four major components: a) energy-deposition spectrum measured in the detector, b) efficiency of the cuts used to select events of the spectrum, c) "live-time" of the detector, and d) expected energy-deposition distributions of LIPs. The basic limit formula uses expected energy-deposition distributions calculated at each incident angle of LIPs; the formula is then simplified. The simplified formula instead uses a single expected energy deposition distribution integrating all angles of incidence of LIPs. The following sections discuss the intensity limit formula and its simplification.

4.1.1 Intensity limit formula

The intensity limit of LIPs for different values of charge (fe), mass (m) and incident $\beta\gamma$ assuming that the particles incident on the detector isotropically is given by-

$$I_v^{90}(f,m,\beta\gamma) = \frac{N^{90}(f,m,\beta\gamma)}{\tau \times \int\int \underbrace{(\epsilon(f,m,\beta\gamma,E) \times \mathrm{PDF}(f,m,\beta\gamma,\theta,E))\,\mathrm{d}E}_{\text{detection efficiency}} \times \underbrace{2\pi A(\theta)\sin\theta\,\mathrm{d}\theta}_{\text{geometric factor}}}, \tag{4.1}$$

where $N^{90}(f,m,\beta\gamma)$ is the upper limit on the number of observed LIPs stated with 90 % confidence, τ is the live time of the detector, $\mathrm{PDF}(f,m,\beta\gamma,\theta,E)$ is the probability distribution of energy deposition for LIPs incident at an angle θ and $\epsilon(f,m,\beta\gamma,E)$ is the

LIP-selection efficiency. The effective cross-sectional area of the detector surface at θ is $A(\theta) = \pi r^2 \cos\theta + 2rh \sin\theta$, where r and h are the detector radius and height, respectively. The different components of the intensity limit formula are discussed in the following sections. The symbols f, m, and $\beta\gamma$ are dropped in the subsequent discussions unless it is necessary.

Upper limit on LIP-induced events (N^{90})

The upper limit on the number of events in the data that are due to interactions of LIPs with the detector is denoted as N^{90}. It is calculated with 90 % confidence using the "Optimum Interval (OI)" method [3].

In rare event searches, often all backgrounds are not fully known or too poorly understood to be subtracted from the data. In such cases, the OI method is a suitable choice for the upper limit calculations. The selection criteria used in the analysis remove significant amount of backgrounds, but all could not be removed. In the N^{90} calculation of the present analysis, all the events after the application of selection criteria are treated as potential signal events. This assumption leads to a conservative estimation of the N^{90} values. In other words, the limits estimated are not optimistic and would have been much lesser in magnitudes (stringent limits) if all backgrounds were subtracted from the data.

Detection efficiency

The LIP-detection-efficiency (see Eqn. 4.1) is defined as the product of the selection-efficiency ($\epsilon(E)$) and the probability distribution of energy deposition (PDF(θ, E)) integrated between the lower and upper bounds of energy deposition (0.1 and 2.0 keV$_{ee}$) considered in the analysis. The lower bound of 0.1 keV$_{ee}$ is chosen to avoid the rapid drop in trigger efficiency below this energy (see Fig. 4.12 of Section 4.4.3). The energy depo-

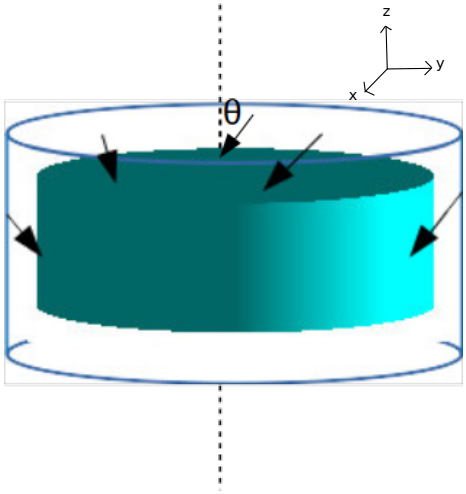

Figure 4.1: Schematic diagram of the detector geometry used in the simulation for the calculation of energy deposition PDFs. LIPs are thrown from surfaces of the outer cylinder surrounding the detector shown in sky-blue.

sition after calibration follows a linear relation with the amplitude of phonon pulse from channel A (see Fig. 2.3 (c) of Chapter 2) up to 2 keV_{ee} and saturates above this energy [4]. Because of this, the upper energy bound of 2 keV_{ee} is considered in this analysis. The selection efficiency of LIPs will be discussed in Section 4.4; the energy deposition PDFs calculated at each incident angle of LIPs is defined below.

$$\mathrm{PDF}(\theta, E) = \frac{n(\theta, E)}{\text{Number of events with incident angle } \theta}, \tag{4.2}$$

where the numerator $n(\theta, E)$ is the number of events with energy deposition E incident with an angle θ. The total number of events incident at angle θ (the quantity in the denominator) normalizes the distribution such that the total probability is unity; this quantity for an isotropic flux Φ_0 is given by-

$$\frac{\mathrm{d}N}{\mathrm{d}\theta} = 2\pi\Phi_0(\pi r^2 \cos\theta \sin\theta + 2rh \sin^2\theta). \tag{4.3}$$

The formula is verified in a simulation, where 10^9 particles are thrown isotropically on the detector (see Fig. 4.1). The comparison of the analytic formula and simulation result is

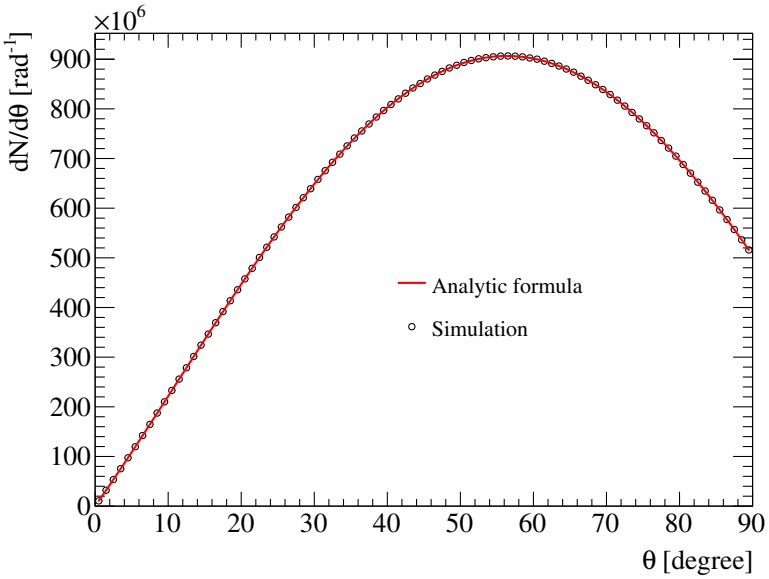

Figure 4.2: The distribution of the number of particles entering the detector at different incident angles.

shown in Fig. 4.2. The derivation of Eqn. 4.3 is given in Appendix 4.A of this chapter.

Geometric factor

The geometric factor in the intensity limit formula is the component which does not depend on the properties of LIPs but only on the geometry of the detector and the solid angle of LIP incidence on the detector surface. This factor comprises of the effective area $A(\theta)$ of the detector surface for incoming LIPs and the solid angle $\mathrm{d}\Omega$. For the top surface, $A(\theta) = \pi r^2 \cos\theta$ and for the side surface, $A(\theta) = 2rh \sin\theta$. The geometric factor $\mathcal{GF}$ is given by-

$$\mathcal{GF} = \int \left[(\pi r^2 \cos\theta + 2rh \sin\theta) \times 2\pi \sin\theta\right] \mathrm{d}\theta. \tag{4.4}$$

It should be noted that the Eqn. 4.3 (the denominator in the definition of PDF(θ, E)) and the integrand in Eqn. 4.4 (geometric factor) differs only by a constant factor i.e Φ_0.

4.1.2 Simplification of the intensity-limit formula

The calculation of intensity limits, as can be seen in Eqn. 4.1, involves integration over solid angles corresponding to different directions of incidence on the detector. However, if we note the defintion of PDF(θ, E) (Eqn. 4.3) and the geometric factor (Eqn. 4.4), the product of the two quantities results in a single angle-dependant component as given by-

$$\int \mathrm{PDF}(\theta, E) \times (\pi r^2 \cos\theta + 2rh \sin\theta) 2\pi \sin\theta \, \mathrm{d}\theta = \int \frac{n(\theta, E)}{\Phi_0} \mathrm{d}\theta. \tag{4.5}$$

The integration in this equation can be taken care of in the energy-deposition simulation circumventing the need to calculate PDF$(f, \beta\gamma, \theta, E)$ for each incident angle of LIPs. The intensity limit formula after this simplification is given by-

$$I_v^{90}(f, m, \beta\gamma) = \frac{N^{90}(f, m, \beta\gamma)}{\tau \times \int_{0.1\ \mathrm{keV}}^{2.0\ \mathrm{keV}} \mathrm{d}E \;\; \epsilon(f, m, \beta\gamma, E) \times \dfrac{n(f, m, \beta\gamma, E)}{\Phi_0}}, \tag{4.6}$$

where $n(f, m, \beta\gamma, E)$ $(= \int n(f, m, \beta\gamma, \theta, E)\mathrm{d}\theta)$ is the number of particles depositing energy E, considering all angles of incidence, out of N thrown from a cylindrical surface surrounding the detector (see Fig. 4.1) in a GEANT4 simulation. If the cylidrical surface has the radius and height of R and H respectively, Φ_0 is given by

$$\Phi_0 = \frac{N}{\pi^2(R^2 + RH)}. \tag{4.7}$$

The detail of the mathematics involved in this simplification is discussed in Appendix 4.A of this chapter.

4.2 LIP signal model

LIP interaction with CDMSlite detector is modeled using the simulation framework described in Chapter 3. The physics processes and models listed in Table 3.1 are used in

the simulation. Of the two choices of models provided in the table for the simulation of ionization energy loss, `G4PAI` [5] model is utilized in this analysis. This model is typically used to model energy depositions in situations where a paucity of interactions is expected (e.g. interactions in thin detectors) as in the cases of LIPs. The `G4PAI` model, unlike other default ionization models (e.g. `G4MuBetheBloch`), produces atomic shell peaks in the distribution of energy deposition.

The expected energy depositions of LIPs are calculated for the various charge, mass, and incident $\beta\gamma$ of the particle from the simulation. The motivation for the simulation-based approach of energy-deposition distribution calculations, as opposed to other methods such as the convolution-based calculations used in CDMS II [6, 7], is discussed in Section 4.2.1. The various approaches of energy-loss distribution calculation are described in Appendix 4.B. The simulation requires, as input, the angular distribution of the incident LIPs. The angular distributions considered for LIPs and the energy-deposition distributions obtained after the simulation are discussed in Section 4.2.2 and Section 4.2.3, respectively.

4.2.1 Motivation for simulation-based approach

A convolution-based method for calculating energy-deposition distributions of LIPs was developed in the CDMS II analysis [6, 7], but is not used in this thesis. There are many advantages of simulation with GEANT4 for the calculation of energy deposition distributions.

a) Accuracy

In general, a Monte Carlo simulation like GEANT4 calculates energy loss or deposition in detectors more accurately than any other method. The same reason has motivated the use of GEANT4 in many experiments including STAR, ALICE, ATLAS, CMS, LHCb, etc. SuperCDMS also uses GEANT4 in the SuperSIM simulation package. As we use the existing

GEANT4 models without making any major changes other than incorporating the charge squared factor in some processes for simulation of LIPs, it is expected that the simulation will give correct energy loss with the same accuracy GEANT4 provides for simulation of other standard particles.

b) Applicability

The convolution-based PDF generation framework developed for LIPs in CDMS II [6, 7] is applicable for the minimum ionizing ($\beta\gamma = 3.1$) LIPs, and for the detector materials germanium and silicon. With the framework developed using GEANT4, energy-deposition distributions for LIPs with any incident $\beta\gamma$, and for a range of typical detector materials can be calculated.

c) Energy loss vs. energy deposition

As charged particles pass through a detector they lose energy, producing electrons (in ionization) or gammas (in bremsstrahlung). The secondaries produced can escape detector volume before losing all of their energy. Under such circumstances, actual energy deposition in the detector will be less than the energy lost by the primary particle. This is a typical case for detectors with small volumes. It is important to track all the secondaries produced at least till they reach the boundary of the detector. GEANT4 do track both primary particle and also all the secondaries produced in interactions with detector material. One can calculate both energy loss by the primary particle and the amount of energy deposited in the detector. Other methods, including the convolution-based distribution calculation, on the other hand, neither calculate energy deposition nor even event-by-event energy loss. It gives directly a probability distribution of energy loss. One needs to make sure, when other

methods are used, that there is a negligible difference[1] between energy lost by the primary particle and energy measured (energy deposited) by the detector.

d) Inclusion of multiple processes and models

Simulation of energy loss of LIPs with GEANT4 along with ionization also uses radiative processes for example bremsstrahlung, and pair-production (see Chapter 3). There is also a possibility of including photo-nuclear process in the list in future. CDMS II on the other hand considered only ionization as the energy loss process for LIPs. Although the radiative processes do not contribute sigficantly in the energy window (0.1–2 keV) of the current analysis, they might have significant contribution if the energy window is broadened in future analyses.

e) Speed

Physical quantities calculated from Monte Carlo simulation often requires huge statistics. GEANT4 meets this challenge by adopting multithreading approach and exploiting the multicore architecture [8]. The current analysis did not require this advanced feature as we were able to generate PDFs with very high statistics (~billion events); time did not bring any limitations. If needs be, the LIPs simulation program can be adapted to use this functionality of GEANT4.

4.2.2 Angular distribution

Charged particles produced in the upper atmosphere from cosmic-ray interactions with the atmospheric nuclei when measured at the earth's surface, it is seen that the flux has

[1] For minimum ionizing LIPs with small charges, as the amount of energy loss is itself small, all of the energy lost by the primary particles are expected to be deposited in the detector. This is the case for the current analysis.

some angular dependence. An example is the cosmic-muon flux measured at the earth's surface. Cosmic muons are produced from pion and kaon decay high (typically 15 km) in the atmosphere; the flux of the particle at the earth's surface is found to have a $\cos^2\theta$ angular distribution [9].

The LIP-flux also has to pass through the atmosphere and rock-overburden before they can reach the Soudan Underground Laboratory (SUL). The interactions of LIP with the atoms along the way can introduce angular dependence in the flux of particles entering the detector placed at SUL. Two limiting shapes for the angular distributions of LIPs are considered: a) an isotropic angular distribution and b) a $\cos^2\theta$ angular distribution. The former is a good approximation for LIPs with small charges as these LIPs seldom interact in a medium (atmosphere plus rock-overburden). However, for LIPs with large charges (close to unit charged particles), since there will be more interactions in the medium, the latter shape will be a good approximation for LIP angular distributions. The $\cos^2\theta$ angular distribution is inspired from the flux measured for muons at the earth's surface.

4.2.3 Energy deposition distributions

In the simulation, LIPs are thrown, according to the angular distribution described in the previous section, on the surfaces of the detector and energy deposition for each LIP passing through the detector are recorded. The distribution of energy-depositions ($n(f, m, \beta\gamma, E)$) for each charge, mass and incident $\beta\gamma$ of LIPs is thus obtained from the simulation. The simulated energy-deposition distributions are then convolved with the detector energy resolution [1].

Figure 4.3 shows the distributions of energy deposition in the detector for various charges of LIPs with a fixed mass of 100 MeV/c^2. It can be seen that the probability of energy deposition is smaller for small fractional charges. The mass of LIP impacts

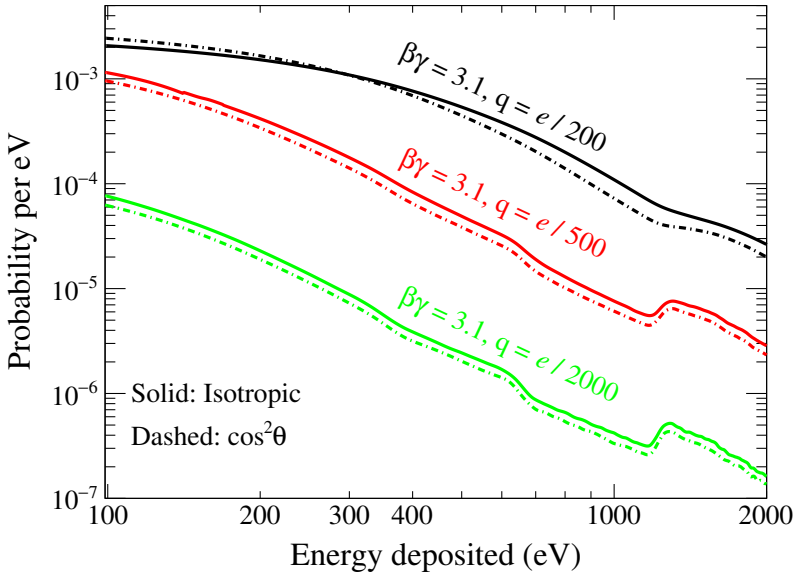

Figure 4.3: Simulated energy-deposition distributions averaged over incident angle for LIPs with a given incident $\beta\gamma$ of 3.1 and different charges of the particle.

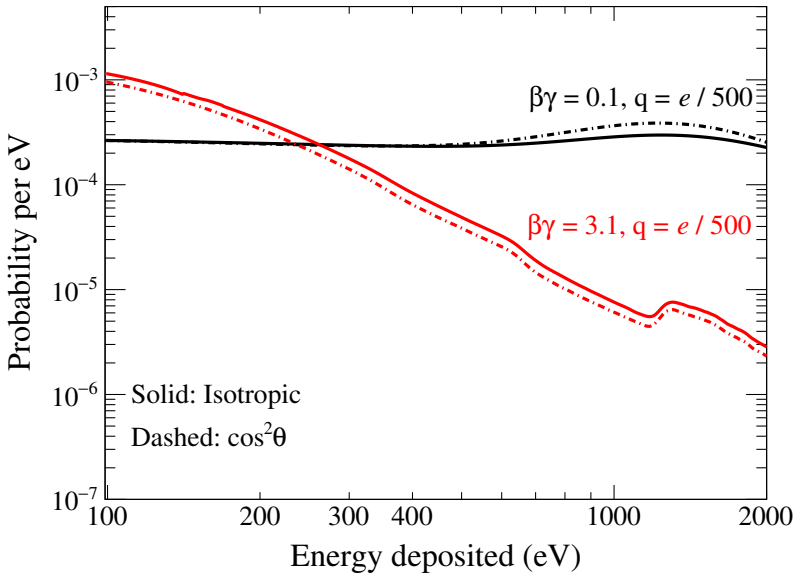

Figure 4.4: Simulated energy-deposition distributions averaged over incident angle for LIPs with a given charge of e/500 and two $\beta\gamma$ values of 0.1 and 3.1.

the expected energy-deposition distribution through the bremsstrahlung process. The number of bremsstrahlung interactions is proportional to the inverse square of the LIP mass. Simulations show that the bremsstrahlung contribution to energy-deposition distributions is negligible within the analyzed energy window and LIP mass range (5 MeV/c^2 – 100 TeV/c^2); consequently, the distributions are found to be effectively independent of mass. However, the incident $\beta\gamma$ of LIPs has strong impact on the distributions. If the $\beta\gamma$ is small (so is the velocity), LIPs can interact multiple times in the detector. As a result, high energy depositions are more probable in the small $\beta\gamma$ region. Figure 4.4 shows the comparison, for a given charge of e/500, of energy-deposition distributions for LIPs with $\beta\gamma = 0.1$ and 3.1. It can be seen that the distribution for $\beta\gamma = 0.1$ shows larger probability of energy depositions towards the upper threshold of the analysis.

4.3 Data set

CDMSlite Run 2 comprises parts of two SuperCDMS Runs, Run 134 (R134) and 135 (R135), during which one of the detectors was operated with high bias voltage (~ 70 V) mode. The comibined R134 and R135 spanned most of 2014, starting from February 2014 and up to January 2015. Figure 4.5 shows the timeline of SuperCDMS Runs. The CDMSlite Run 2 had two data taking periods: Period 1 (or Run2a) and Period 2 (Run2b).

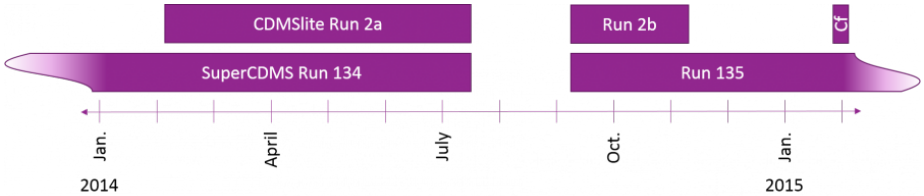

Figure 4.5: Timeline of CDMSlite Run 2 along with SuperCDMS Runs [4]. The data taken during CDMSlite Run 2a is used for the LIP-search analysis.

The data taken during Period 1 (February through July 2014) is used in the LIP-search

analysis. While the CDMSlite Run 2 data, based on both Period 1 and Period 2, is published for the WIMP-search [1, 10], the data from Period 1 is not inspected in this analysis untill the limit-setting framework for the LIP-search is developed. In place of data spectrum, the energy-deposition distribution of the background model developed for CDMSlite Run 2 is used in developping the limit-framework and calculating intensity-limit projections. This consideration makes the analysis effectively "blind". The blind analysis reduces possibility of introducing biases by the analyzers in the final results. The importance of a blind analysis can be found in Ref. [11, 12].

4.4 Event selection and efficiency of selection cuts

Selection criteria are applied to the experimentally measured data to remove non-physical events (such as electronic glitches) and physical events caused due to backgrounds (such as gamma, electron), and thereby leaving possible signal events from LIPs in the data spectrum. The selection criteria defined by CDMSlite Run 2 WIMP-search [1] are also used in the current analysis. This is because the relativistic LIPs with small fractional charges, similar to WIMPs, scarcely interact with the detector. However, the departure from WIMP-like features are expected from LIPs in the small velocity and large charge region. This is accounted for by calculating corrections to efficiencies of the relevant selection cuts.

The selection cuts can be classified into two major categories: quality cuts and physics cuts. The detailed description of the selction cuts can be found in Mark Pepin's thesis [13].

4.4.1 Quality cuts

The events that are not caused by interaction of a particle are removed by some quality cuts. These events could be due to electronic glitches or some non-physical reasons.

A. General quality cuts

1. *Bad Base Temperature, HVPS Current, or 2T-Fit:* The energy scale calibration (described in Chapter 11 of Pepin's thesis [13]) requires the information of the base temperature of the experiment, the output current from the high voltage power supply (HVPS), and 2T-fit (two template Optimal Filter (OF) fit) results. Some of the events have base temperature exceptionally high or not recorded, and some have exceptionally high HVPS current. These events along with those which could not be fitted with 2T-fitting algorithm are removed from the data as these events could not be calibrated.

2. *Bad GPS Timing Information:* The Data Acquisition system used in SuperCDMS had two methods of recording the time of an event. It was found that the time information from the two methods disagrees [14, 15], the reason for which is not understood, by an appreciable amount for some events. These events are removed by applying a selection cut.

3. *Traditional Glitch Cut:* The events with pulses having rapid rise and fall-times are defined as glitches. These events are not caused due to particle interactions in the detector. The number of phonon-triggered and charge-triggered channels in a physics event should be roughly equal. If a significant difference between them is observed, the events are removed as glitches. The events which satisfy the following criteria [16] are removed: $(n_p - n_q) > 6$ or $(n_q - n_p) > 1$, where n_p and n_q are the numbers of phonon-triggered and charge-triggered channels, respectively.

4. *Non-triggered Ionization Glitches:* Some glitch events with extremely sharp rise and fall-times, large amplitudes, and multiple peaks pass the traditional glich cut described earlier. The pulses of these events exhibit poor fit with the OF template. A cut in the OF-fit χ^2 vs. total ionization energy plane is defined and is shown in Fig. 4.6. The cut defined by the blue line in the figure rejects high χ^2 events from the data.

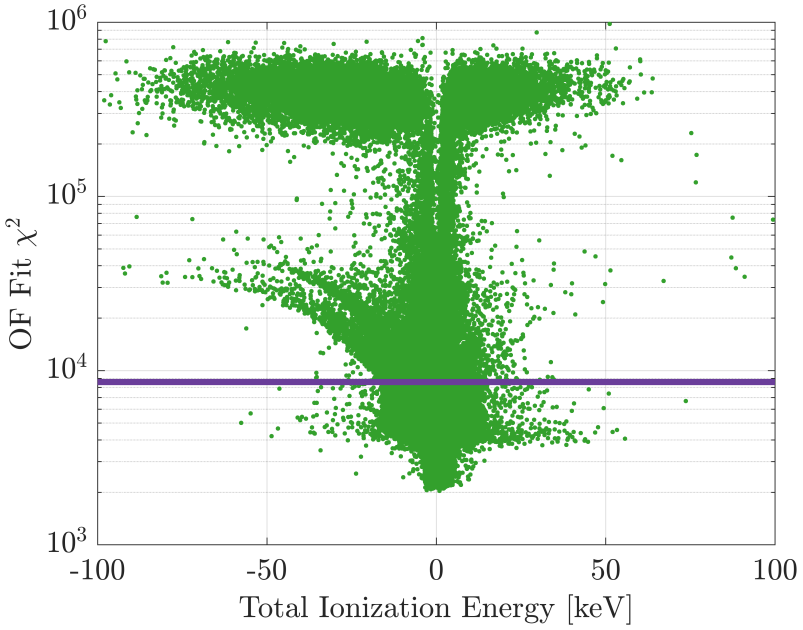

Figure 4.6: The comparison of OF-fit χ^2 and total ionization energy after the application of the cuts mentioned in 1–3 of the list of quality cuts (Section 4.4.1) [13]. The events above the blue line are the "Non-triggered Ionization" glitches.

5. *Good Phonon Baseline Noise:* The phonon pulse template (see Chapter 2) has a flat pre-pulse baseline whereas the pre-pulse baseline in the phonon traces has Gaussian electronic noise. A cut is defined to remove events with pre-pulse widths greater than 4σ, where σ (standard deviation) is determined by fitting the distribution of pre-pulse widths from randomly-triggered events with a Gaussian function.

6. *Bad Data Series:* Some "data series"[2] are removed as "bad" if they satisfy the following criteria.

   a) The ionization glitch cut removes more then 4 % of the live time in the series.

   b) The series has phonon traces with long tail.

   c) The detector is not pre-biased in the series.

B. Pulse-shape based quality cuts

The phonon pulse of an event is fitted using the Optimal Filter algorithm [17] with templates of three different types: a standard physical pulse template (also referred to as a "good pulse" template), a low-frequency noise template, and a glitch template. The comparison of the templates is shown in Fig. 4.7. An additional algorithm referred to as the non-stationary optimal filter (NSOF) [18] is also used for the "good pulse" template. The amplitude of the fits, after calibration, for the good pulses are used as an estimate of energy, while the χ^2 values of the fits are used to determine the quality of the pulse shapes. The comparison of χ^2 values from the fits to the three templates indicates how close, in resemblance, a pulse is to the respective templates and therefore can be used to separate good events from the low-frequency noise and the glitch events.

1. *Phonon Pulse Quality:* The events with exceptionally high χ^2 values (of the order of 10^4 as in Fig 4.6) of fits to "good pulse" templates are removed by applying a cut in the χ^2 Vs. energy plane. Figure 4.7 shows (the green curve) a typical "good pulse" template. The cut for this analysis is defined using the ^{133}Ba and ^{252}Cf calibration (discussed in Chapter 2) data. The cut mostly removes the "pile-up" events and those with saturated pulses. The events with more than one pulse recorded in a single trace are pile-ups. The

[2] The basic unit of stored data was a data series (or series, for short). The length of a series was determined by how long the detectors could maintain sufficient neutralization for the full collection of the charge signal.

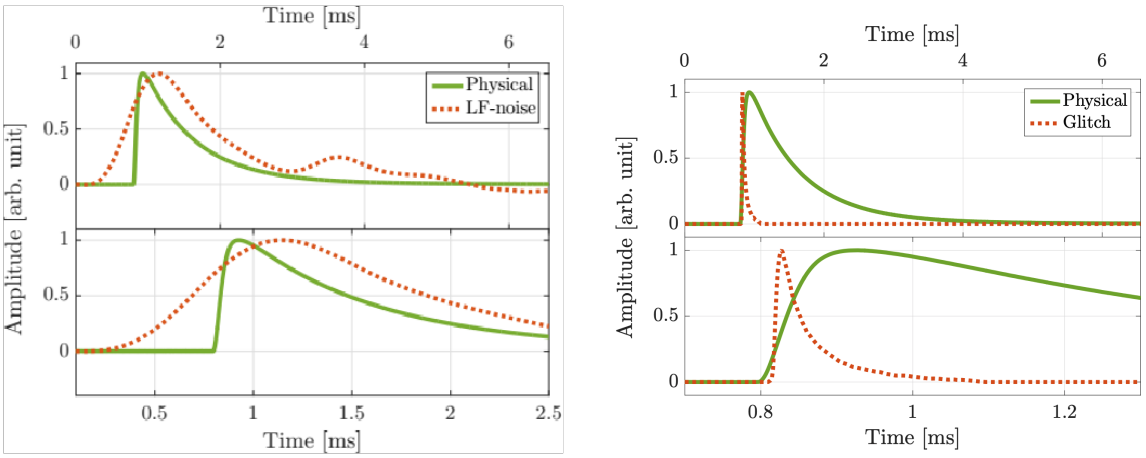

Figure 4.7: Left: the template for "good pulses" compared to the template for low frequency noise. Right: the template for "good pulses" compared to the template for glitches. The zoomed version of the templates around the rising edge is shown in the bottom panels.

common feature of such events is more than one peak in their traces. On the other hand, the peak of a saturated pulse is flattened.

2. *Low-Frequency Noise:* The primary source of low-frequency noise is the vibrations from the cryocooler used in the experiment [1]. The basic feature of a LF-noise trace is that it has slow rise and fall times and has oscilations in the tail. A LFN template which charecterizes these traces is shown in Fig. 4.7. The LFN events are removed by a cut that is developed using: a) cryocooler timing information, b) correlated noise metric, and c) $\Delta\chi^2_{LF}$ pulse-shape criteria [13].

$$\Delta\chi^2_{LF} = \chi^2_{OF} - \chi^2_{LF}, \tag{4.8}$$

where χ^2_{OF} is goodness-of-fit parameter for the fit with the "good-pulse" template and χ^2_{LF} is the same for the fit with LFN template.

3. *Pulse-Shape Glitches:* Some glitch events could not be removed by the general glitch quality cuts described earlier. The characteristic feature of the glitch traces are that they

have sharp rise and fall times. A template for glitch traces is shown in Fig. 4.7. A pulse-shape-based discrimination criteria is developed using the difference of χ^2 values ($\Delta\chi^2_{Gl}$) of "good-pulse" template and glitch template fits in the $\Delta\chi^2_{Gl}$ Vs. phonon energy plane. The cut removes the glitch events from the data.

4.4.2 Physics cuts

The events that are caused by interaction of a particle, but not expected of a LIP, are removed by some physics cuts. These events could be those co-incident with known sources, multiple-scattering events in detector array or events failling fiducial volume requirement. The physics cuts defined for the CDMSlite Run 2 WIMP-seach [1] are also used in this analysis. The cuts are discussed in the below sections. Some WIMP-search-based cuts could be much stricter than they need to be for the LIP-search analysis; they can remove some true LIP-induced events from the data. The possibility of losing LIP-events are also discussed while describing the cuts.

1. *Muon Veto Coincidence:* Cosmic muons can penetrate the earth overburden and reach the underground laboratory at Soudan. These muons can interact with the detector producing events. Besides, muon-produced neutrons, hadronic and electromagnetic showers can also cause triggering in the detector. SuperCDMS uses scintillation panels to veto cosmic muons, thereby associated events in the detector.

   The scintillation panels are about 5 cm thick, where muons generally deposit about 10 MeV energy. And, the threshold set in the panels to tag muons is about 1–2 MeV. Since the charge of LIPs considered in the analysis is less than a $e/100$, LIPs are very unlikely to be tagged by the veto panels. Therefore, the cut does not remove any LIP events.

2. *NuMI Beam Coincidence:* Soudan also houses the MINOS experiment [19] where it

detects the neutrino from NuMI or Neutrinos at the Main Injector [20] beam originated at Fermi National Accelerator Laboratory (FNAL). These neutrinos have very little probability of triggering events in the detector. However, to be conservative, the events that occurred when the NuMI beam was on are removed from the data.

3. *Singles Cut:* LIPs in general are expected to scatter from a single detector. On the other hands, backgrounds like gammas, electrons are likely to interact in multiple detectors. The events which exhibit interactions in multiple detectors ("multiple scatter" events) along with the CDMSlite detector are removed to reduce backgrounds from the data. The strategy adopted to remove "multiple-scatter" events are described by a flow diagram in Fig. 4.8, and can be summarised as follows:

   - First, examine if the energy deposition in the CDMSlite detector is above its threshold in an event.
   - Then, identify if any other detector (veto) has energy deposition above the single cut's threshold of the same detector in that event.
   - Check if the trace in the vetoing detector is a LF-noise or a pulse-shape glitch or the event is classified as a triggered glitch. If this is the case then the event is not a candidate of "multiple scatter". Otherwise, the event is removed from the data.

   To calculate the singles cut threshold of a detector, the energy deposition distribution for noises in the detector is fitted with a Gaussian, and the energy at which the cumulative of the distribution is 99.87 % (3σ equivalent of a Gaussian) is considered as the threshold. The randomly triggered events were an estimate of the noise for a given series, or set of series. The noise distributions are not in general Gaussians; they have large tails in the high-energy end. The threshold will be at a 3σ value from the mean if the

noise distribution were a perfect Gaussian. Figure 4.9 shows the noise distribution of a "series" and the threshold determined following this procedure.

The noise is not the same in a detector throughout the data-taking period; consequently, the energy thresholds in the veto detectors are not time-invariant. The data from multiple consecutive"series" with similar noise performances in a detector are combined to form "time-blocks" [21] and for each time block, an energy threshold is calculated using the procedure described above. The energy threshold in a veto detector varies from time-block to time-block.

This selection cut however has one disadvantage. The cut can remove some true LIP-induced events from the data. This is because LIPs with large charges and small velocities can hit multiple detectors. On the other hand, LIPs with small charges and relativistic velocities, as they rarely interact in multiple detectors, have very little probability of being removed by this selection cut. The range of charges and $\beta\gamma$ values for which the cut is efficient can be understood from the discussion on efficiency correction for LIPs in Section 4.4.4.

4. *Radial Cut:* The total phonon energy (E_t) measured in the detector (described in Chapter 2) is a sum of the recoil energy (E_r) and the NTL-gain which is proportional to the potential difference δV experienced by the electron-hole pairs created in the interaction:

$$E_t = E_r + E_r \frac{e\,\delta V}{\epsilon} \tag{4.9}$$

For interactions in the bulk of a detector, δV is equal to the potential difference between the top and bottom faces of the detector i.e. 70 V. This happens for most of the events. However, the electric field at the edges of the detector crystal is not uniform [1] as shown by the voltage map in Fig. 4.10, and δV can be smaller near the sidewall of the

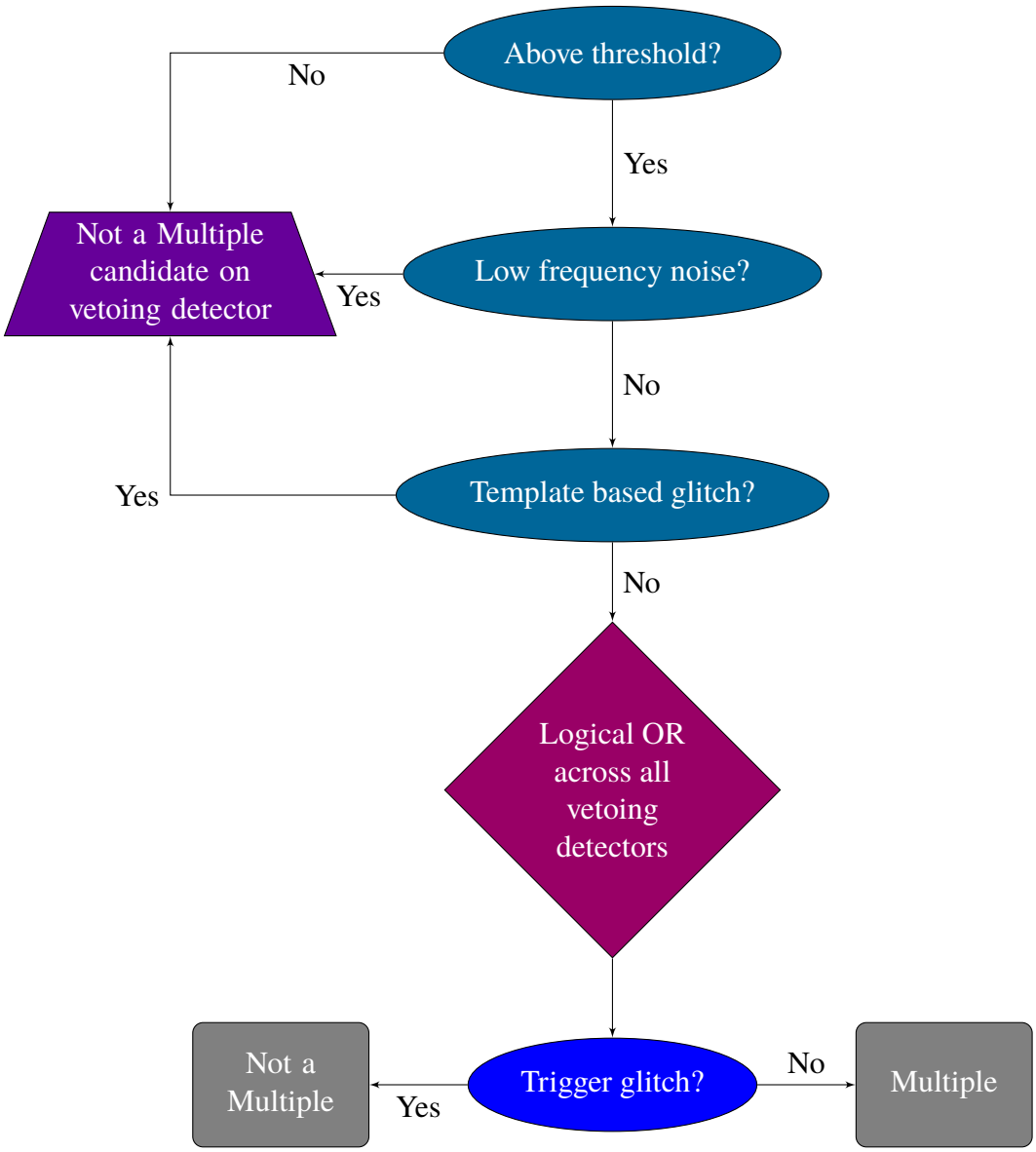

Figure 4.8: A logic diagram describing the event selection with singles cut.

detector. There could be events with interactions at high radii, and the total potential the charges drift through in those events is less than a 70 V. The NTL-gain will be lesser in such events. Consequently, some high-energy recoils are incorrectly reconstructed as low-energy recoils. Those events are removed by a radial cut.

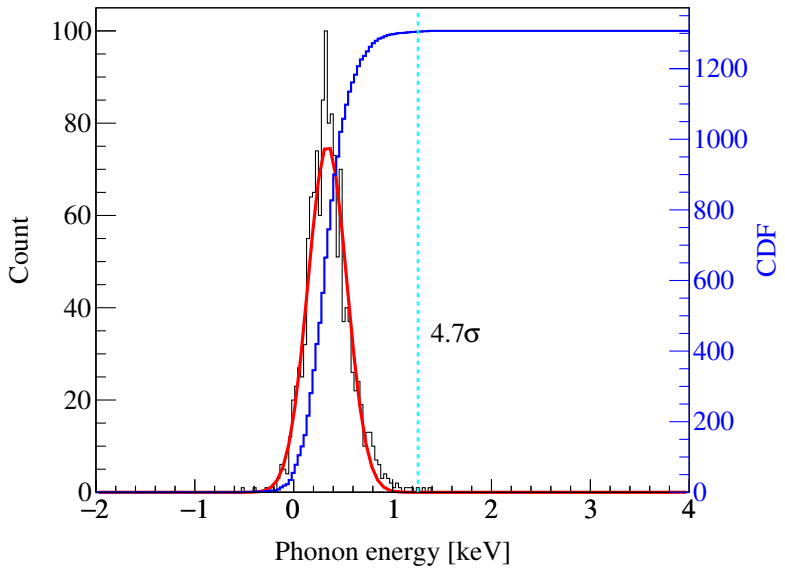

Figure 4.9: A distribution of energy deposition with randomly-triggered (noise) events of a 'data series' in T3Z3 detector. The distribution is fitted with a Gaussian, and the energy at which the cumulative of the distribution is 99.87 % is considered as the threshold of the detector.

To define the cut, a radial parameter representing the radial position of an event is needed. The detail of how the radial parameter is developed is discussed in Ref. [13, 22]. Figure 4.11 shows the radial parameter Vs. energy for the Period 1 data. The events above the blue dashed line in the figure are removed by this cut.

The radial cut developed in CDMSlite Run 2 WIMP search [1] is ideal for single-interaction events, as in the cases of WIMPs, in the detector. However, LIPs with large charges and small velocities can interact multiple times within the detector. As a result, this cut can remove some true LIP-induced events from the data. The cut without any change is used for the LIPs search analysis in this thesis with a correction made to the efficiency of the cut; this will be discussed in Section 4.4.4.

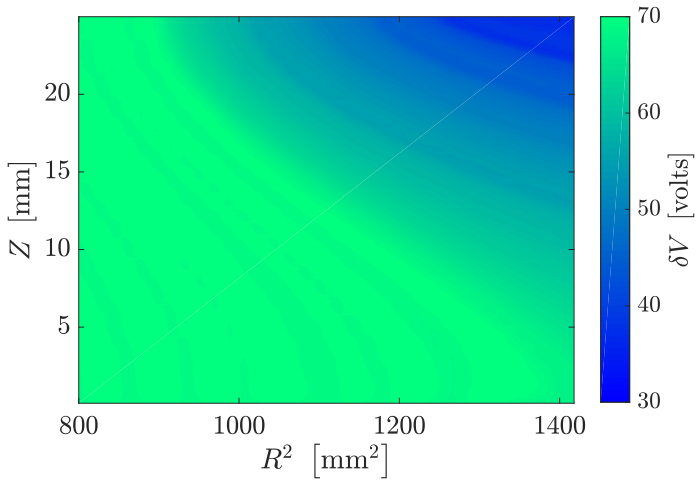

Figure 4.10: The voltage map for high radius events [1]. The x-axis is the radius squared and the y-axis is the vertical position. The potential difference δV is between the initial and final location of the charge carriers. The top face of the crystal is at 70 V, while the bottom is at 0 V. The copper case that houses the detector is also at 0 V, and there exists a small gap between the case and the sidewall. The total potential difference experienced by drifting charges, as a result of this, is less than 70 V in regions in the detector where field lines end on the sidewall. The low radii region (below $R^2 = 800$ mm^2) experience the full 70 V potential difference.

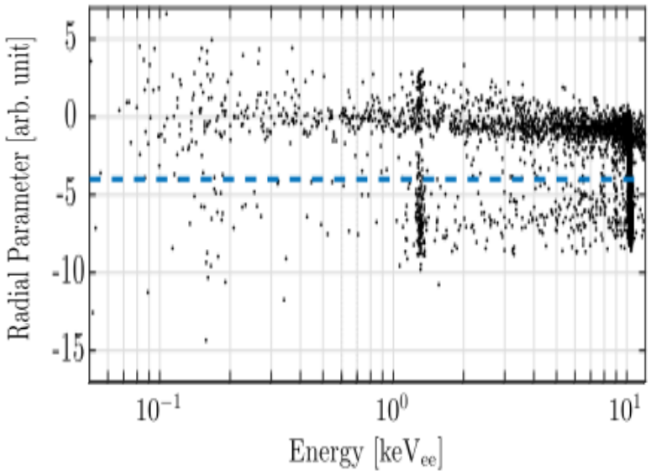

Figure 4.11: The radial parameter vs. energy deposition in the detector for the CDMSlite Run 2 Period 1 data [1]. The blue dashed line is the threshold of the radial cut; the events above this line are removed.

4.4.3 Selection efficiency

The efficiencies of the muon-veto cut and the singles cut are energy-independent, while the efficiencies of the pulse-shape based quality cuts and the radial cut are functions of energy deposition in the detector. The efficiencies of different cuts are described below.

1. *Muon Veto Cut Efficiency:* The efficiency of the muon-veto coincidence cut is determined using the noise i.e the randomly-triggered events. The efficiency of the muon veto cut is the fraction of the randomly-triggered events that are also tagged by the veto panels. The efficiency of this cut is found to be 98.77 ± 0.01 %.

2. *Singles Cut Efficiency:* Similar to the veto cut, the efficiency of the singles cut is also determined from randomly-triggered events. The efficiency of this cut is one minus the fraction of randomly-triggered events that are mis-identified as a multiple scatters. The efficiency of the cut is 98.27 ± 0.01 %.

3. *Trigger efficiency:* This is the efficiency with which the Data Acquisition (DAQ) system triggers on pulses or events. The trigger logic is set in a way that it prevents noise from dominating the data collection. A trigger is issued if the pulse measured exceeds a specified voltage threshold (typically ∼10 mV). However, as the pulse amplitudes get smaller, the DAQ triggers more noises than signals and the trigger efficiency reduces. In other words, while events with very low energy deposition that are buried inside the baseline noise will never be triggered (efficiency equal to zero), very high energy-deposition events will always be triggered with unit efficiency. And, there will be events in between that are only slightly distinguishable from noises and the efficiency will be somewhere between 0 and 1.

   The general method of estimating this efficiency[13] is as follows:

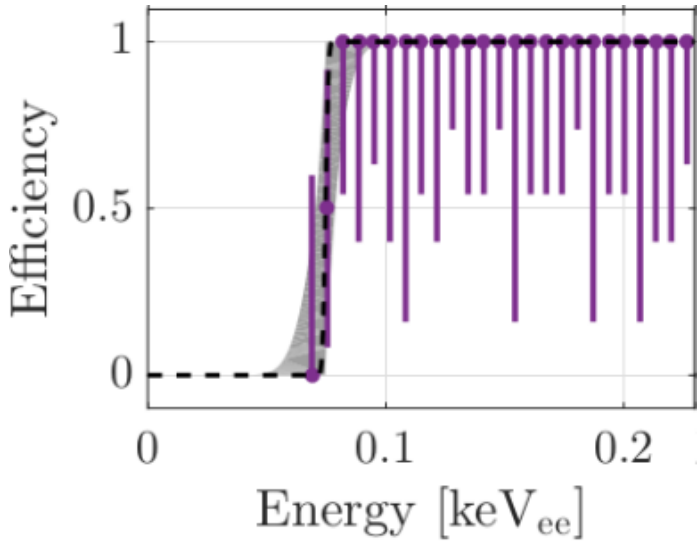

Figure 4.12: The trigger efficiency as a function of energy deposition for CDMSlite Run 2 Period 1 data [1]. The trigger efficiency is ∼1 within the energy window (0.1 − −2.0 keV) considered in this analysis.

a) Collect high statistics calibration data.

b) Find events that issued a trigger on a non-CDMSlite detector.

c) Of these events, determine how many are also issued a trigger in the CDMSlite detector. The trigger efficiency that is the fraction of these events as a function of energy deposition in the CDMSlite detector is determined.

The ^{252}Cf calibration data [1] taken during Period 1 is used to calculate the trigger efficiency. The detectors above and below the CDMSlite detector are used (as non-CDMSlite detectors) for this purpose. The trigger efficiency as a function of energy deposition in the CDMSlite detector for Period 1 is shown in Fig. 4.12. It rapidly rises and saturates to unity at high energy depositions in the detector.

The trigger efficiency is used to choose the lower energy threshold. A threshold of 0.1 keV is chosen in this analysis. This avoids the region where the efficiency shows a

sharp rise (Fig. 4.12) and thus simplifies the analysis. Besides, the efficiency is 100 % for all energy depositions above 0.1 keV.

4. *Pulse-shape-based cuts efficiency:* A set of events representing the real data (called "fake events") are simulated and the fraction of them that passes the pulse-shape-based cuts is considered as the efficiency of the cuts. The simulation procedure is graphically described in Fig. 4.13. A noise trace combined with a scaled template acts as a fake event. The fake event is then run through the CDMS standard reconstruction algorithm to obtain the RQ/RRQs[3] such as the OF energy estimators.

   To estimate the systematic uncertainty, the efficiency calculation is repeated with three different types of pulse templates. The pulse templates considered are the standard OF template, and the "peaky" and "non-peaky" templates created by a linear combination of the fast (sharp rise) and slow (slow rise) templates [13]. The three templates are shown in Fig. 4.14. The joint efficiency of all pulse-shape-based cuts for Period 1 is shown in Fig. 4.15. The upper and lower limits of the systematic uncertainties at different energies are the maximum and minimum of the efficiency for the three template curves.

5. *Radial cut efficiency:* The radial cut efficiency is estimated utilizing the electron-capture peaks of ^{71}Ge which is produced during the neutron calibration of the germanium detector with the ^{252}Cf source of neutrons [1]. The electron capture by ^{71}Ge from its orbitals and the emission of gammas and/or Auger electrons following the capture is shown in Eqn. 4.10. The process produces peaks at the K, L and M-shell binding

[3]The variables after processing the raw data collected by the experiment are called reduced quantities (RQs) and refined reduced quantities (RRQs).

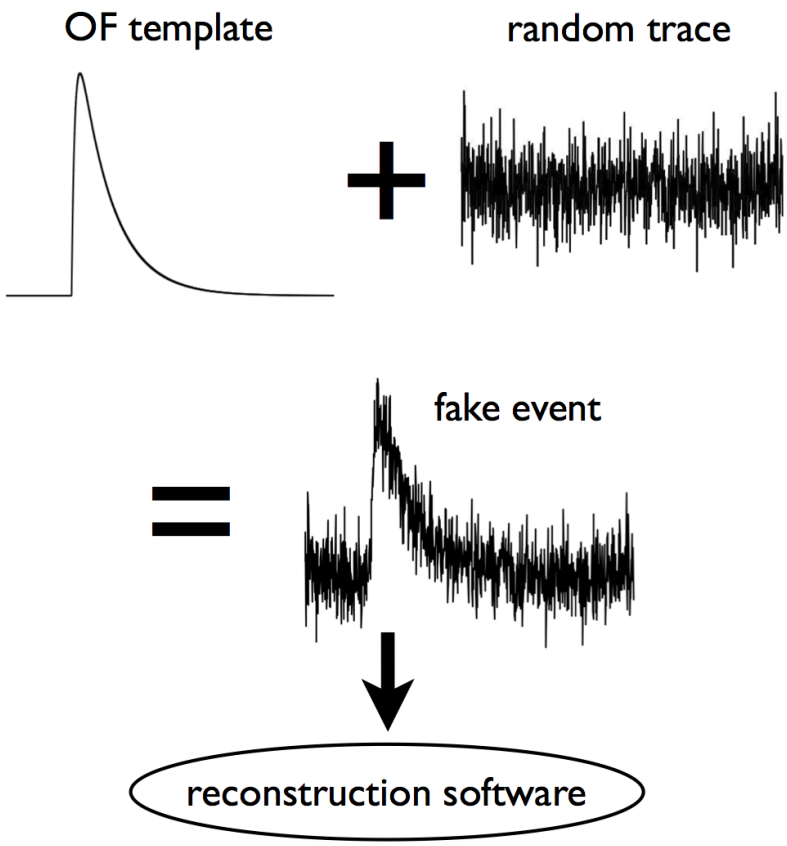

Figure 4.13: A graphical description of the event simulation procedure to generate fake events for the efficiency calculation of pulse-shape-based cuts [23]. The OF template is scaled to a particular amplitude, and then summed with a real random trace from Run 2 data period.

energies of ^{71}Ga; they are at 10.37, 1.30 and 0.16 keV, respectively [24].

$$\begin{aligned} {}^{70}\mathrm{Ge} + \mathrm{n} &\longrightarrow {}^{71}\mathrm{Ge} \\ {}^{71}\mathrm{Ge} + \mathrm{e} &\longrightarrow {}^{71}\mathrm{Ga} + \nu_e \\ {}^{71}\mathrm{Ga} &\longrightarrow {}^{71}\mathrm{Ga} + \gamma\text{'s}, \mathrm{e}\text{'s} \end{aligned} \tag{4.10}$$

Fig. 4.16 shows a cartoon describing the distribution of events from a mono-energetic source, such as the electron-capture peak, in the radius vs. energy deposition plane in the presence of a non-uniform electric field inside the crystal (see Fig. 4.10). The events

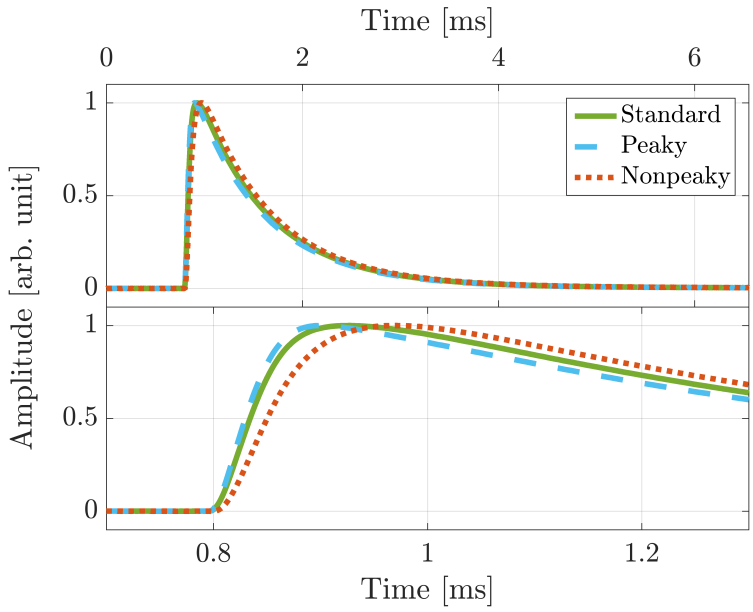

Figure 4.14: The pulse templates (top) used for generating fake events for the efficiency calculation of pulse shape based cuts [13]. The templates zoomed within 0.7 and 1.3 ms (bottom) show that the rise and fall times of the "peaky" template are shorter and of the "non-peaky" template are longer as compared to those of standard OF template.

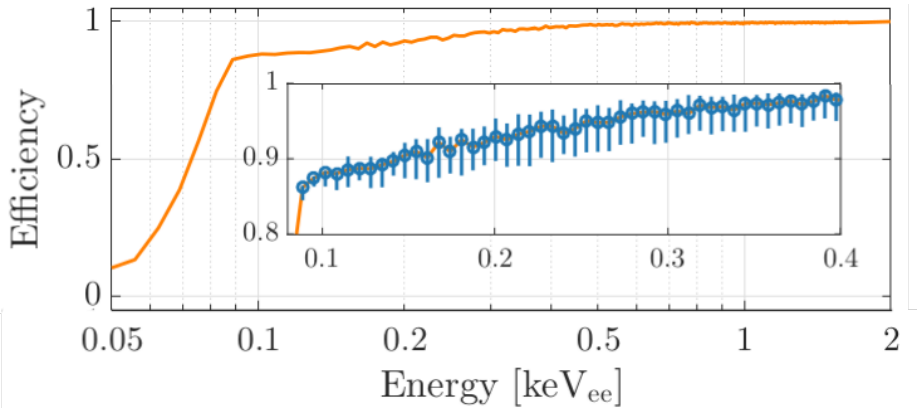

Figure 4.15: The efficiency of pulse-shape-based cuts plotted as a function of energy for Period 1 [1]. The uncertainty in the efficiency includes both statistical and systematic uncertainties, where the systematic uncertainty is obtained by using three different types of pulse templates described in Ref. [13].

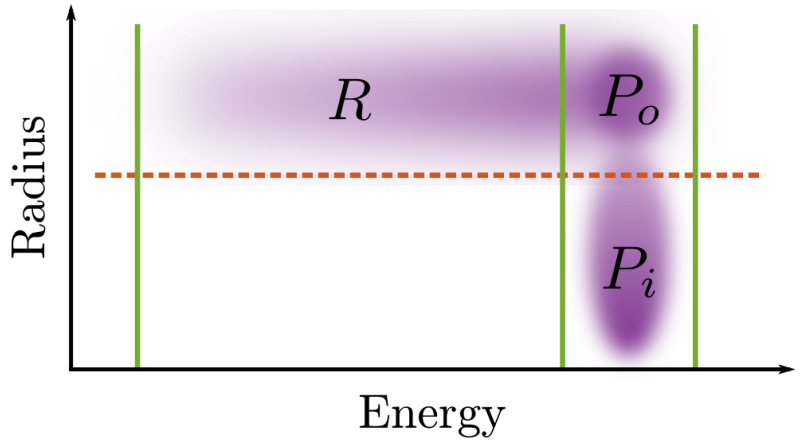

Figure 4.16: A cartoon showing the distribution of events in the radius vs. energy plane [1].

of this plane can be calssified into a) the events in the primary peak (P), and b) those with reduced NTL-gain (R). The events with low NTL-gain are mis-reconstructed as low energy recoils. Of all the events in the peak, some will pass the radial cut (P_i) and some will fail (P_0). The efficiency of radial cut is therefore:

$$\begin{aligned} \varepsilon &= \frac{P_i}{R+P} \\ &= \frac{P}{R+P} \times \frac{P_i}{P} \\ &= \varepsilon_1 \times \varepsilon_2 \end{aligned} \tag{4.11}$$

Here, ε_1 is the fraction of events with full NTL-gain and ε_2 is the fraction with full NTL-gain that also passes the radial cut. The former is related to the electric field map and is independent of energy, while the latter is calculated for various energy depositions in the detector. ε_1 is calculated for the K-shell peak and is used for the energy range considered in the analysis. At the K-shell peak, ε_2 is calculated from the data and for smaller energies "fake events" similar to the procedure described in Fig. 4.13 are used to calculate ε_2. The template used to generate the fake events is described in Ref. [1, 13]. Figure 4.17 shows the radial cut efficiency as a function of energy-deposition for

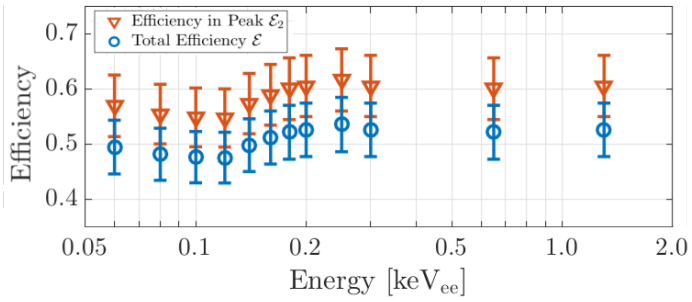

Figure 4.17: Radial cut efficiency as a function of energy deposition for Period 1 [1].

Period 1. The efficiency is ~50 % for for all energies within the analysis energy window (0.1–2 keV).

The total efficiency is the product of the efficiencies calculated for individual cuts. The efficiencies of the selection cuts are sequentially multiplied and are shown in Fig. 4.18. The radial cut efficiency is the dominant component of the total efficiency as can be seen in the figure. The correction factors to the radial and singles cut efficiencies are applied to account for the fact that some true LIP-induced events can be removed by these two cuts. These corrections are discussed below.

4.4.4 LIP-specific efficiency corrections

A. Singles cut efficiency correction: The singles cut reduces background sources capable of depositing energy in multiple detectors. However, LIPs with large charge may deposit energy in multiple detectors and hence can be rejected by this selection cut. A simulation with GEANT4 is performed to calculate the correction factor $\epsilon_{\text{sdh}}(f, \beta\gamma)$ of the singles cut efficiency described earlier. The simulation geometry, which includes the five towers of SuperCDMS detectors with three germanium detectors in each, is shown in Fig. 4.19. In the simulation, LIPs are thrown isotropically or with an angular distribution of $\cos^2\theta$ shape towards the detector arrangement of Fig. 4.19 and event-by-event energy depositions in all

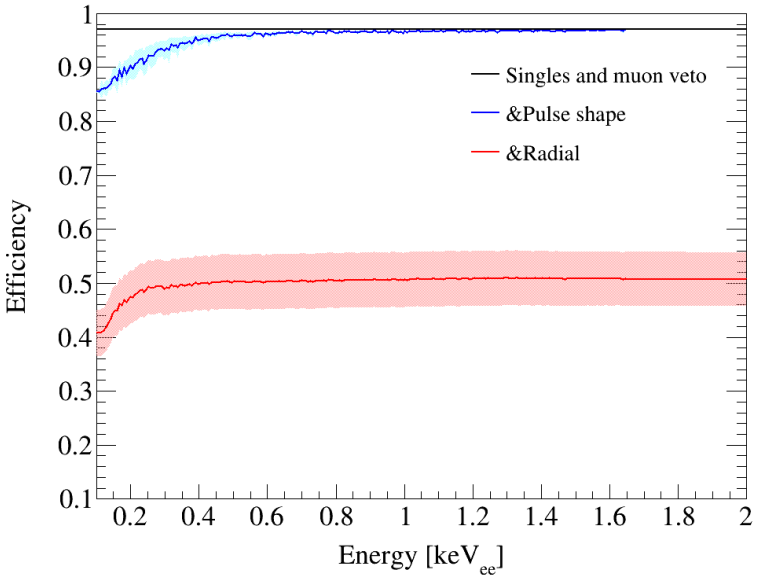

Figure 4.18: The efficiencies for Period 1 after sequential multiplication of individual efficiencies. The trigger efficiency is not shown as it has unit efficiency within the analysis thresholds (0.1–2.0 keV). The radial cut efficiency has the dominant contribution to the final efficiency. The 1σ uncertainty, which include both statistical and systamatic uncertainties, on efficiencies are shown in the figure.

fifteen detectors are recorded. The correction factor $\epsilon_{\text{sdh}}(f, \beta\gamma)$ is estimated as

$$\epsilon_{\text{sdh}}(f, \beta\gamma) = 1 - \frac{N_{\text{md}}(f, \beta\gamma)}{N_{\text{CDMSlite}}(f, \beta\gamma)}, \tag{4.12}$$

where $N_{\text{CDMSlite}}(f, \beta\gamma)$ is the number of events depositing energy in the CDMSlite detector within the analyzed energy window (0.1–2 keV), and $N_{\text{md}}(f, \beta\gamma)$ is the number of LIP events that also deposit energy in at least one other detector above its threshold ($\gtrsim$ 1 keV). Figure 4.20 shows the singles cut efficiency correction as a function of f^{-1} for both isotropic and $\cos^2\theta$ angular distribution. The correction factor, for a given $\beta\gamma$, decreases as the charge of LIP is reduced (large f^{-1}) and it approaches to unity for very small ($f^{-1} > 2 \times 10^3$) fractional charges. Also, the correction factor is larger for small $\beta\gamma$ values. In other words, the singles-cut efficiency requires no correction ($\epsilon_{\text{sdh}}(f, \beta\gamma) \sim 1$), if the charge of LIPs is very small.

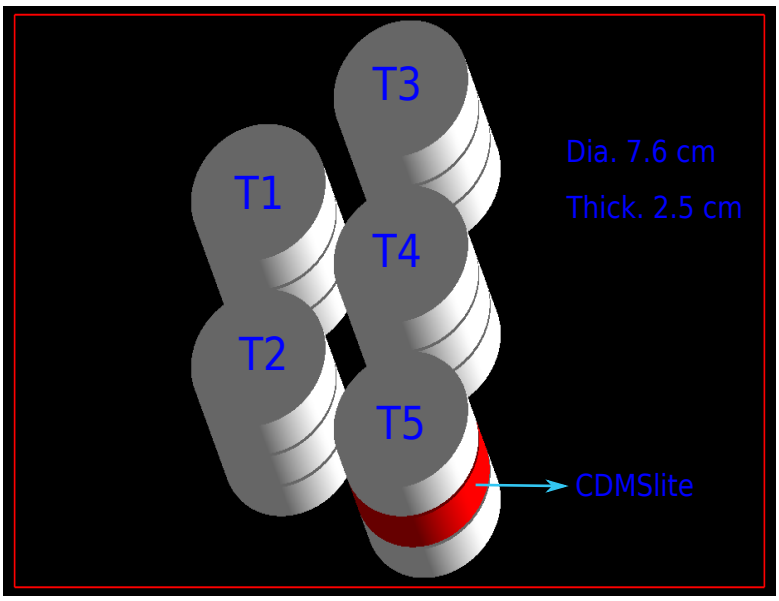

Figure 4.19: The simulation geometry defined with GEANT4 for the singles-cut efficiency calculation. The detectors are stacked in five towers with each having three detectors. The detector in red is the CDMSlite detector. LIPs are thrown isotropically or with an angular distribution of $\cos^2\theta$ shape towards this detectors' arrangement.

B. Radial cut efficiency correction: The correction factor for the radial-cut efficiency ($\epsilon_{\rm fv}(f,\beta\gamma)$) to account for the fact that some true LIPs events can be rejected by the cut is also calculated from simulations with GEANT4. While the radial cut removes events with interaction locations at high radii [1], we conservatively assume, for the efficiency correction calculation, that all events with more than one interaction point (need not be at the high radii) in the CDMSlite detector is such that they are rejected. LIPs are thrown isotropically or with a $\cos^2\theta$ angular distribution towards the CDMSlite detector. The number of events that deposit energy (number of interactions ≥ 1) in the CDMSlite detector ($N_{\rm total}(f,\beta\gamma)$) and the number of them that shows more than one interactions (number of interactions > 1) in the detector ($N_m(f,\beta\gamma)$) are determined from the simulation. The efficiency correction

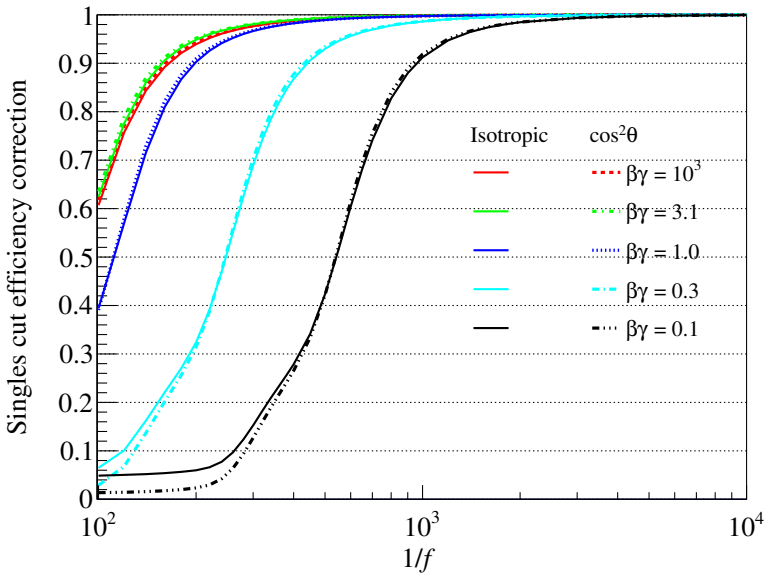

Figure 4.20: The singles-cut efficiency correction factor plotted as a function of f^{-1} for various values of $\beta\gamma$. The correction factors for both isotropic and $\cos^2\theta$ angular distribution are calculated and are shown by the solid and dashed lines, respectively.

factor is given by

$$\epsilon_{\mathrm{fv}}(f,\beta\gamma) = 1 - \frac{N_m(f,\beta\gamma)}{N_{\mathrm{total}}(f,\beta\gamma)}. \tag{4.13}$$

Figure 4.21 shows the radial-cut efficiency correction factor as a function of f^{-1} for various incident $\beta\gamma$ of LIPs. The efficiency correction factor saturates to unity for small fractional charges of LIPs. The factor is smaller for small incident $\beta\gamma$ of LIPs.

4.5 Intensity limit projection

Before analyzing the data and calculating final intensity limits, the expected sensitivities are calculated for various values of charge and incident $\beta\gamma$ of LIPs. This consideration makes the analysis effectively "blind". The calculation requires a set of events that represent the data. The spectra of energy depositions generated from the background model developped for CDMSlite Run 2 [2, 25] along with other components needed for a limit calculation

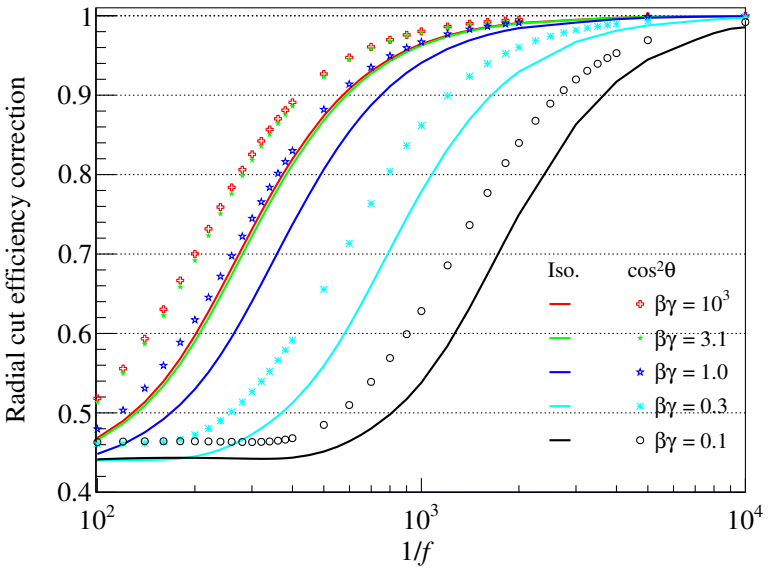

Figure 4.21: The radial-cut efficiency correction factor plotted as a function of f^{-1} for various values of $\beta\gamma$. The correction factors for both isotropic and $\cos^2\theta$ angular distribution are calculated and are shown by the solid lines and markers, respectively.

such as the signal spectrum, live-time and efficiencies are used. The background model and the results from the calculation of expected sensitivities or the projected limits are described below.

4.5.1 Background model spectra

The background sources that dominantly contribute to the energy spectrum measured in CDMSlite detector are the materials used for shielding and other apparatus and the detectors (15 detectors arranged in 5 towers) themselves. The dominant backgrounds are cosmogenic activation and neutron activation (during ^{252}Cf calibration) of the detector crystal, and Compton scattering from radioactive isotopes in the apparatus materials.

SuperCDMS detectors get expose to cosmic radiation during their fabrication, testing and storage above ground. The protons and neutrons from cosmic radiation cause spallations in the detector and apparatus materials whereby radioactive isotopes are produced.

Isotope	^{71}Ge	^{68}Ge	^{68}Ga	^{65}Zn	^{57}Co
half-life	11.4 d	270.3 d	68 m	244.3 d	271.9 d
Isotope	^{55}Fe	^{54}Mn	^{49}V	^{3}H	
half-life	2.73 y	312 d	330 d	12.32 y	

Table 4.1: The list of isotopes including their half-lives considered for the background model. The half-life data of the isotopes are taken from Ref. [27].

Also, during the calibration Runs of the CDMSlite detector with ^{252}Cf neutron source, radioactive ^{71}Ge isotopes are produced by neutron capture of the ^{70}Ge nucleus of the detector. The isotopes produced from the activations (cosmogenic and calibration) can have sufficiently long half-lives that they do not decay away between the time the detectors brought underground and the time of commencement of data-taking, as well as have live-times small enough to produce significant event rates in the energy-deposition spectrum. Table 4.1 shows the list of isotopes that are considered for the background model. The radiogenic photons from the contaminants in experimental materials which include shield materials (polyethylene and lead), cryostat (copper) and detector towers (copper) primarily contribute to the Compton backgrounds [26].

A maximum likelihood fit to the CDMSlite Run 2 energy deposition spectrum, where the fit includes all the different background components discussed above, is performed. Figure 4.22 shows the CDMSlite Run 2 energy deposition spectrum and the function describing the backgrounds obtained from the fit.

The energy-deposition distributions sampled from the background model curve are used as representative of the data. While the Period 1 data of CDMSlite Run 2 will be used for the final limit calculation, the CDMSlite Run 2 energy-deposition spectrum shown in Fig. 4.22 is based on both Period 1 and Period 2. The number of events in CDMSlite Run 2 is 318 [10], the same expected in Period 1 data will be lesser. The expected number of events is calculated by weighing the total events in Run 2 by the fraction of Period 1

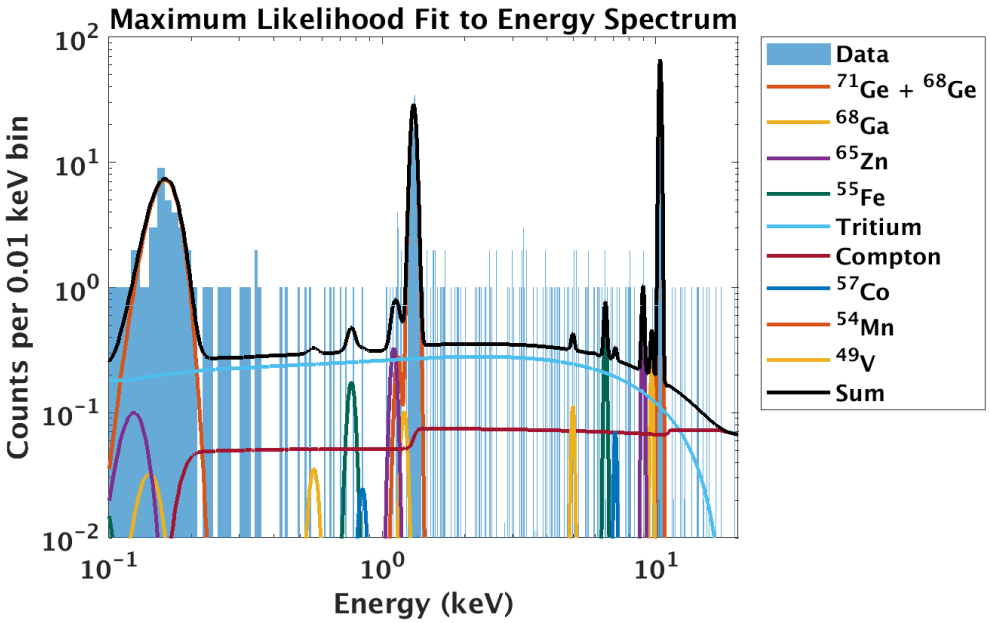

Figure 4.22: The background model from the maximum likelihood fit of CDMSlite Run 2 energy deposition spectrum [28].

live-time ($\sim$ 86%), and it is 270 ± 16. An energy deposition distribution sampled from the background model is shown in Fig 4.23.

4.5.2 Expected sensitivity and uncertainties

The expected sensitivity of LIPs are calculated with the use of the mathematical framework described in Section 4.1 including all the components such as the expected signal energy-deposition distributions, selection efficiencies, and live-time of the detector. The background model generated distribution of energy deposition is used as representative of the data. The sensitivity calculation is repeated 200 times with each calculation utilizing an energy deposition distribution generated from the background model. The mean of the distribution of sensitivities are calculated for various f^{-1} and incident $\beta\gamma$ of LIPs. The

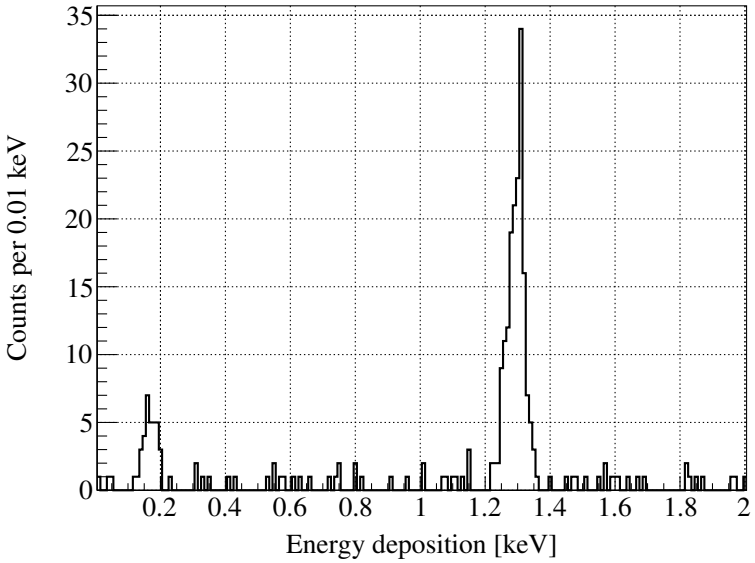

Figure 4.23: A sample distribution of energy deposition obtained from the background model. The number of events in the sample distributions are 270 ± 16. The uncertainty in the number of events is statistical and it is 1σ of the expected number of events.

1σ of the distribution is the statistical uncertainty due to the energy-depositions generated from the background model. The final intensity limits will not have this uncertainty as the data is a single energy deposition spectrum measured in the CDMSlite detector. The uncertainties common to both expected sensitivity and final limits are described below.

4.5.3 Uncertainties

1. *Uncertainties in selection efficiency:* The limits are calculated with randomly sampled efficiency curves. An example set of efficiency curves is shown in Fig. 4.24. The distribution of efficiencies at a given energy is a Gaussian with mean and standard deviation given by the central value and the uncertainty, respectively. The variation of the limits calculated with different efficiency curves is considered as the uncertainty due to selection efficiency; this is a major source of uncertainty.

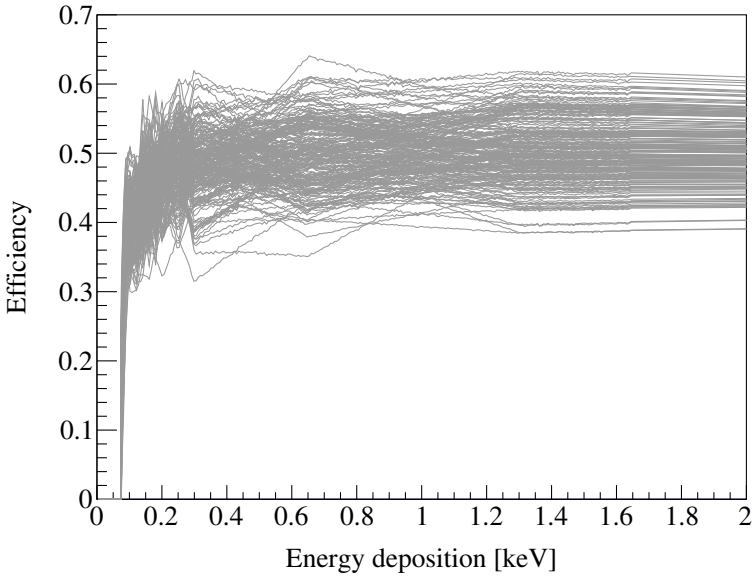

Figure 4.24: An example set of randomly sampled efficiency curves for the intensity limit calculation.

2. *Uncertainties in lower and upper energy bounds:* The lower and upper bounds of energy considered in this analysis are 0.1 and 2.0 keV, respectively. If the energy bounds are varied, the same can lead to different intensity limit results. The energy bounds are varied within the detector energy resolution [1] (see Chapter 2) to calculate the uncertainty due to this.

3. *Uncertainties in the signal model:* The limits are calculated with expected energy-deposition distributions calculated using GEANT4-based simulations. The distributions have statistical uncertainties. A set of 50 energy-deposition distributions, for a given charge and $\beta\gamma$, are calculated by repeating the simulation the same number of times. The intensity limit calculation is also repeated 50 times, where each calculation uses a distribution from the set. The variation in the intensity limits caused by this iterative procedure is considered as the statistical uncertainty due to the signal model.

   A systematic uncertainty on the signal model is also considered. In the CDMS II

LIP analysis, a convolution-based approach (described in Appendix 4.B) of calculating energy-deposition distribution was used. The difference in intensity-limit results with distributions obtained using GEANT4-simulation and CDMS II method is considered as a systematic uncertainty.

In the sensitivity calculation, the energy deposition distribution from the background model, the selection efficiency and the energy thresholds are varied altogether within their uncertainties. The resulting 1σ uncertainty on the expected sensitivity is ~32%. This uncertainty is quadratically added to the uncertainty due to the signal model, and the total uncertainty is found to be ~40%.

The expected sensitivity along with its uncertainty is shown as a function of f^{-1} for various values of $\beta\gamma$ in Fig. 4.25. Since the signal energy-deposition distributions are independent of mass in the range of masses considered (5 MeV/c^2–100 TeV/c^2), the calculated sensitivity is valid for the entire mass range. The most restrictive sensitivity is in the range of f^{-1} between 2×10^2 and 2×10^3. The sensitivity worsens outside this range of f^{-1}.

4.6 Data spectrum

The Period 1 LIP-search data is examined for the first time after finalizing the event-selection criteria and their efficiencies, the systematic uncertainties, and the procedure for calculating the LIP intensity limits. The measured spectrum contains 180 events after application of all selection criteria and is shown in Fig. 4.26. The most prominent features in the spectrum are the L- and M-shell peaks from decays of intrinsic Ge radioisotopes, as described in Ref. [1].

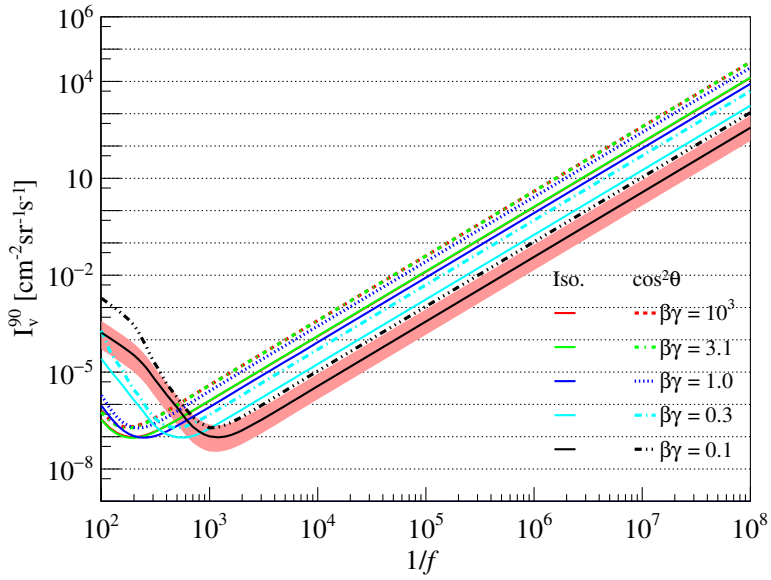

Figure 4.25: The expected sensitivity as a function of f^{-1} for various values of $\beta\gamma$. The solid lines shows the sensitivities for an isotropic distribution and the dashed lines for $\cos^2\theta$ angular distribution of LIPs. For clarity, 1 σ uncertainty band is shown for $\beta\gamma$ of 0.1 only.

4.6.1 Verification of the spectrum

A variety of checks are performed to see how the spectrum obtained in Fig. 4.26 compares with our expectations. Two primary checks are as follows.

Expected vs. actual Period 1 total events comparison:

The CDMSlite Run 2 background model was used to create energy-deposition distributions as representative of the data for the expected sensitivity calculation. While the mean number of events predicted for Period 1 was 270; we observed 180 events in the data. This is statistically different. This apparent discrepancy can be explained by the following argument. The relative number of events in the L and M shells from ^{252}Cf calibration does not scale with live-time. The amount of activation preceding Period 1 and Period 2 was approximately equal while Period 2 had far less live-time. Therefore, our scaling by the

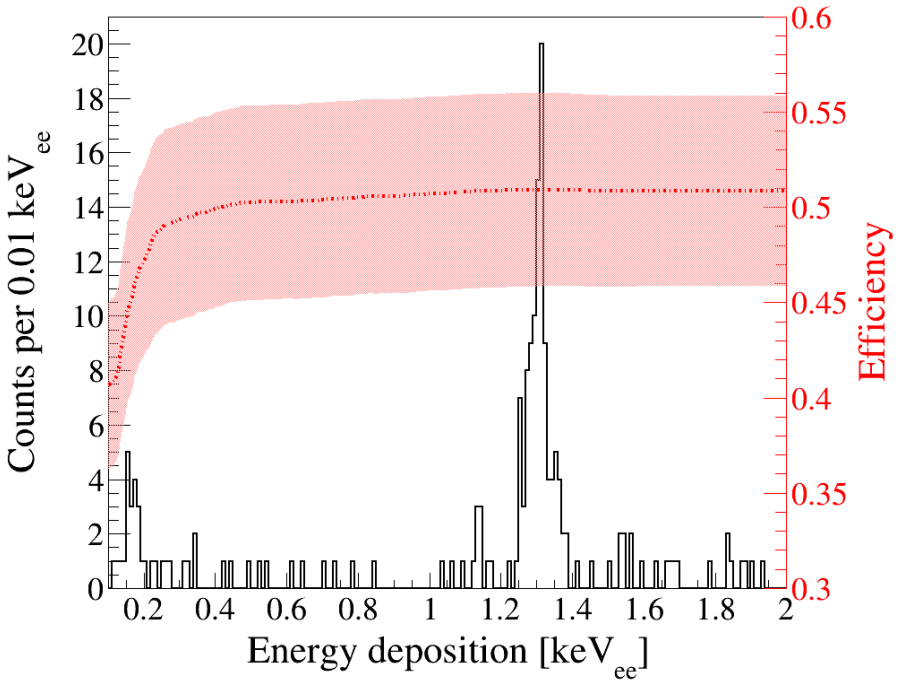

Figure 4.26: The measured energy-deposition spectrum after application of all event-selection criteria (black solid histogram labeled on left axis). Also shown is the selection efficiency (the red dashed curve labeled on right axis) with 1σ uncertainty (red band). The total efficiency shown in the figure is before applying corrections to singles-cut and radial-cut efficiencies. The energy depositions are measured in electron equivalent units (keV$_{ee}$) where it is assumed that all energy depositions in the detector are due to electron recoils [1].

live time greatly overpredicted the number of events that would be in these peaks. The number of events outside the peaks did scale with live-time [29].

Shape and peak position of the spectrum:

The mean energies associated with the L and M shell peaks are known. One can fit the peaks of the spectrum and compare the fit-results with those known values to see how accurate they are in the data.

The L-shell peak is fitted with a Gaussian plus a first order polynomial. The mean of the Gaussian (μ) obtained from the fit gives the location of the peak in the data spectrum.

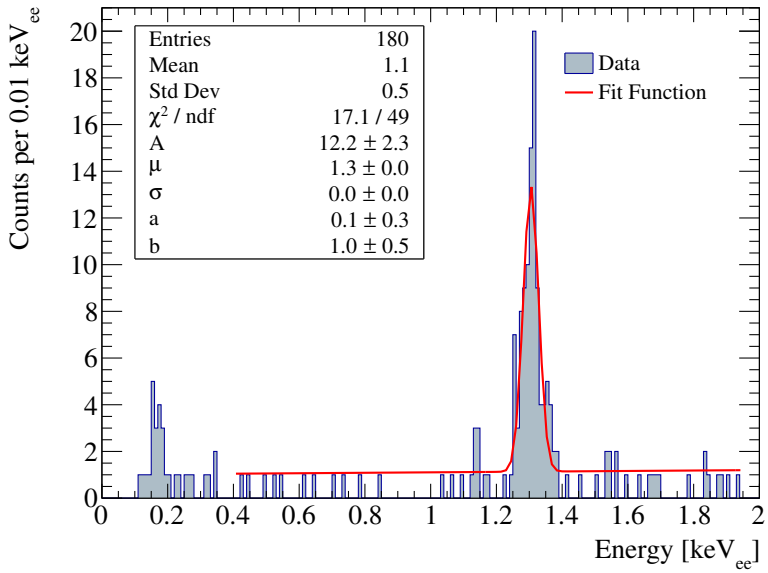

Figure 4.27: The energy deposition spectrum from Period 1 fitted with a Gaussian plus a first order polynomial.

Fig. 4.27 shows the fit to the L shell peak. The location of the L shell peak from the fit is found to be 1.3 keV$_{ee}$ (μ = 1.305 keV$_{ee}$), which matches with the expected location of the peak.

We also noticed that the mean values of the L-shell peak in Period 1 and Period 2 are slightly different from each other [30]. It is possible that this is an indication of the energy scale shift between the two data periods.

After these two checks, the data energy-deposition spectrum is considered for the intensity limit calculations.

4.7 Intensity limits

The 90 % confidence upper limits on intensity of cosmogenic LIPs are calculated with the Period 1 data. Fig. 4.28 shows the limits calculated in this analysis compared to the results from all prior searches of cosmogenic LIPs with minimum ionizing velocities ($\beta\gamma$ = 3.1).

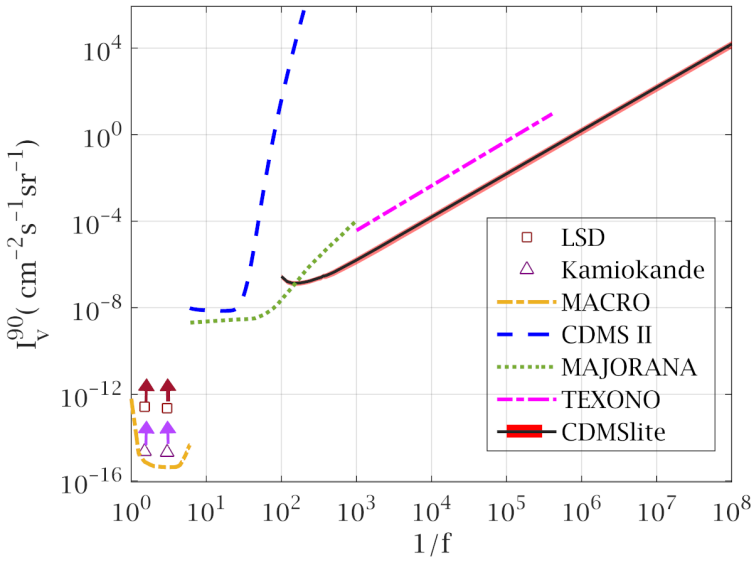

Figure 4.28: The 90 % confidence upper limit on the LIP intensity (solid black) compared to those from all prior searches, including LSD [31] (brown □), Kamiokande [32] (purple Δ), MACRO [33] (yellow dot-dashed), CDMS-II [34] (blue dashed), MAJORANA [35] (green dotted), and TEXONO [36] (magenta dot-dashed) under the assumptions of an isotropic distribution for minimum-ionizing LIPs [37]. The red band shows the 1σ level uncertainty on the limit.

This result sets the strongest constraint on LIPs with $f^{-1} > 160$, including a minimum intensity limit of $1.36 \times 10^{-7}\,\mathrm{cm^{-2}s^{-1}sr^{-1}}$ at $f^{-1} = 160$. Figure 4.29 shows the limits for a range of $\beta\gamma$ values, and for both isotropic and $\cos^2\theta$ angular distribution. The results are valid for the entire range of mass considered i.e 5 MeV/c^2 to 100 TeV/c^2. The intensity limit computed for a $\cos^2\theta$ angular distribution is nearly three times weaker than that for an isotropic angular distribution for most values of f^{-1}.

4.8 Conclusions

An analysis to search for LIPs with the data acquired in CDMSlite mode in the SuperCDMS experiment is presented. The analysis covers a wide range of parameter space: charges

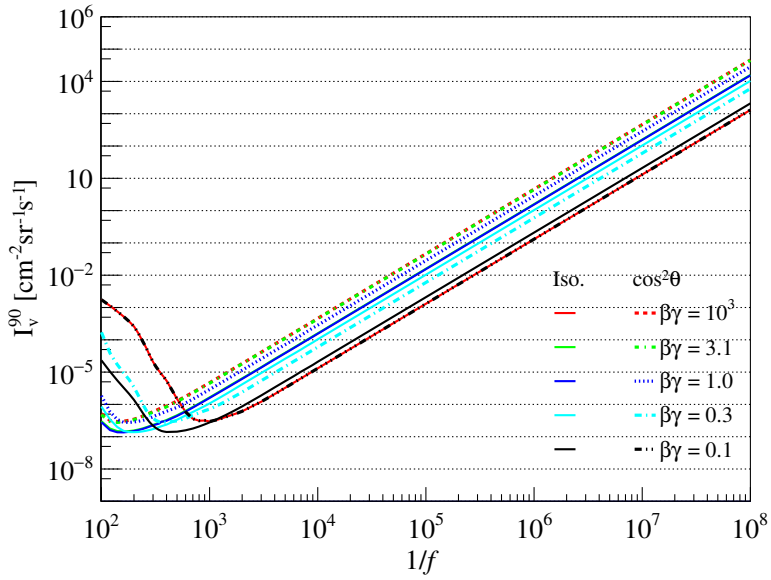

Figure 4.29: The 90 % confidence upper limit on intensity for various $\beta\gamma$ of LIPs. The solid lines show the limits for the isotropic distribution and the dashed lines for $\cos^2\theta$ angular distribution of LIPs.

smaller than $e/100$, masses between 5 MeV/c^2 and 100 TeV/c^2, and incident $\beta\gamma$ between 0.1 and 10^6. It is the first to probe the impact of mass on the signal model and therefore on the intensity limits. While the prior direct-searches of cosmogenic LIPs focused on minimum ionizing LIPs ($\beta\gamma \sim 3.1$), this analysis is the first to probe LIPs with non-relativistic velocities and also extended the $\beta\gamma$ range up to a 10^6.

The intensity limit calculation has several components which include a signal model, a measured data spectrum, the efficiency of selection cuts, and the exposure of the experiment. The basic formula of intensity limits, for a given charge, mass and $\beta\gamma$, require calculating expected signal energy deposition distributions at all incident angles. A framework is established where the limit calculation, for a given set of LIP parameters (mass, charge and $\beta\gamma$), can be done without knowing the distributions at each incident angle; a solid-angle-integrated distribution is used instead. The integration is taken care in the simulation

to calculate energy-deposition distribution of LIPs. Also, this is the first analysis where a GEANT4-simulation-based signal model is used. The importance of a simulation-based signal model is discussed.

The selection cuts and efficiencies including some corrections specific to this analysis are discussed. The efficiency corrections are calculated for singles and radial cuts and their product is the combined efficiency correction. The efficiency corrections are found to have significant impact for large charge and small velocities of LIPs. However, the combined efficiency correction approaches unity at charges smaller than $e/10^4$ for all $\beta\gamma$ considered in the analysis.

The expected sensitivity is calculated with the background model generated spectra and the final limits are calculated with the data spectrum measured in the experiment. The final limit agrees with the expected sensitivity within about 2σ for charges between $e/160$ and $e/500$, and within 1σ elsewhere. The final intensity limits are also compared with all prior direct-searches of cosmogenic LIPs. The analysis presented in this thesis sets the strongest constraint on LIPs with charges $< e/160$, including a minimum intensity limit of $1.36 \times 10^{-7}\,\mathrm{cm}^{-2}\mathrm{s}^{-1}\mathrm{sr}^{-1}$ at charge $e/160$ [37].

Bibliography

[1] R. Agnese et al. "Low-mass dark matter search with CDMSlite". *Phys. Rev. D* 97 (2 2018), 022002.

[2] R. Agnese, T. Aralis, T. Aramaki, et al. "Production rate measurement of Tritium and other cosmogenic isotopes in Germanium with CDMSlite". *Astroparticle Physics* 104 (2019), 1 –12.

[3] S. Yellin. "Finding an upper limit in the presence of an unknown background". *Phys. Rev. D* 66 (3 2002), 032005.

[4] *Summary of CDMSlite Run 2 First Results*. SuperCDMS internal note.

[5] J Apostolakis et al. "An implementation of ionisation energy loss in very thin absorbers for the GEANT4 simulation package". *Nucl. Instrum. Methods Phys. Res. A* 453.3 (2000), 597 –605.

[6] Kunj Bihari Prasad. "Search for lightly ionizing particles using CDMS-II data and fabrication of CDMS detectors with improved homogeneity in properties". PhD thesis. Texas A-M, 2013.

[7] R. Agnese, A. J. Anderson, D. Balakishiyeva, et al. "First Direct Limits on Lightly Ionizing Particles with Electric Charge Less than $e/6$". *Phys. Rev. Lett.* 114 (11 2015), 111302.

[8] J. Allison, K. Amako, J. Apostolakis, et al. "Recent developments in Geant4". *Nuclear Instruments and Methods in Physics Research Section A: Accelerators, Spectrometers, Detectors and Associated Equipment* 835 (2016), 186–225.

[9] M. Tanabashi et al. "Review of Particle Physics". *Phys. Rev. D* 98.3 (2018), 030001.

[10] SuperCDMS Collaboration. *CDMSlite Run 2 Data Release*. https://www.slac.stanford.edu/exp/cdms/ScienceResults/DataReleases/CDMSlite_Run2/CDMSlite_Run2_DataRelease_Document.pdf.

[11] P F Harrison. "Blind analysis". *Journal of Physics G: Nuclear and Particle Physics* 28.10 (2002), 2679–2691.

[12] Joshua R Klein and Aaron Roodman. "Blind ANALYSIS IN NUCLEAR AND PARTICLE PHYSICS". *Annual Review of Nuclear and Particle Science* 55.1 (2005), 141–163. eprint: https://doi.org/10.1146/annurev.nucl.55.090704.151521.

[13] Mark David Pepin. "Low-Mass Dark Matter Search Results and Radiogenic Backgrounds for the Cryogenic Dark Matter Search". PhD thesis. Minnesota U., 2016.

[14] J. Morales. *NuMI Cut R134*. SuperCDMS Internal note, Run 133-135 Analysis. 2015.

[15] D. Barker. *CDMSlite R2 NuMI Cut*. SuperCDMS Internal note, Run 133-135 Analysis. 2015.

[16] R. Bunker. *Initial Study of R133 Glitch Events*. SuperCDMS Internal note, Run 133-135 Analysis. 2012.

[17] Sunil Ramanlal Golwala. "Exclusion limits on the WIMP nucleon elastic scattering cross-section from the Cryogenic Dark Matter Search". PhD thesis. UC, Berkeley, 2000.

[18] *Summary of First iZIP Low Threshold Analysis*. SuperCDMS Internal note.

[19] D.G. Michael, P. Adamson, T. Alexopoulos, et al. "The magnetized steel and scintillator calorimeters of the MINOS experiment". *Nuclear Instruments and Methods in Physics Research Section A: Accelerators, Spectrometers, Detectors and Associated Equipment* 596.2 (2008), 190–228.

[20] P. Adamson, K. Anderson, M. Andrews, et al. "The NuMI neutrino beam". *Nuclear Instruments and Methods in Physics Research Section A: Accelerators, Spectrometers, Detectors and Associated Equipment* 806 (2016), 279–306.

[21] Elias Lopez Asamar. *Time blocks for r133 data blinding*. SuperCDMS internal note.

[22] W. Rau. *New Position Estimators based on 2-template quantities*. SuperCDMS Internal note, Run 133-135 Analysis. 2015.

[23] A.J. Anderson, L. Hsu, and B. Serfass. *Estimation of quality cut efficiencies from template-based pulse simulation*. SuperCDMS internal note. 2013.

[24] J. A. BEARDEN and A. F. BURR. "Reevaluation of X-Ray Atomic Energy Levels". *Rev. Mod. Phys.* 39 (1 1967), 125–142.

[25] D'Ann Rebekah Barker. "SuperCDMS Background Models for Low-Mass Dark Matter Searches". PhD thesis. Minnesota U., 2018.

[26] William Alexander Page. "Searching for Low-Mass Dark Matter with SuperCDMS Soudan Detectors". PhD thesis. British Columbia U., 2019.

[27] M.B. Chadwick, M. Herman, P. Obložinský, et al. "ENDF/B-VII.1 Nuclear Data for Science and Technology: Cross Sections, Covariances, Fission Product Yields and Decay Data". *Nuclear Data Sheets* 112.12 (2011). Special Issue on ENDF/B-VII.1 Library, 2887–2996.

[28] E. Fascione. *Maximum Likelihood Analysis - Finalized Version*. SuperCDMS internal note. 2019.

[29] Sudip Poudel. *LIPs Vertical Intensity Limits*. SuperCDMS internal note. 2020.

[30] Samir Banik. *CDMSLITE RUN 2A DATA SPECTRUM FOR THE LIPS ANALYSIS*. SuperCDMS internal note. 2020.

[31] M. Mori, Y. Oyama, A. Suzuki, et al. *Phys. Rev. D* 43 (9 1991), 2843–2846.

[32] M. Mori, Y. Oyama, A. Suzuki, et al. "Search for fractionally charged particles in Kamiokande II". *Phys. Rev. D* 43 (9 1991), 2843–2846.

[33] M. Ambrosio, R. Antolini, G. Auriemma, et al. *Phys. Rev. D* 62 (5 2000), 052003.

[34] R. Agnese, A. J. Anderson, D. Balakishiyeva, et al. *Phys. Rev. Lett.* 114 (11 2015), 111302.

[35] S. I. Alvis, I. J. Arnquist, F. T. Avignone, et al. *Phys. Rev. Lett.* 120 (21 2018), 211804.

[36] L. Singh, J. W. Chen, H. C. Chi, et al. "Constraints on millicharged particles with low-threshold germanium detectors at Kuo-Sheng Reactor Neutrino Laboratory". *Phys. Rev. D* 99 (3 2019), 032009.

[37] I. Alkhatib et al. "Constraints on Lightly Ionizing Particles from CDMSlite" (Nov. 2020). arXiv: 2011.09183 [hep-ex].

Appendix 4.A Simulation of flux for intensity limit calculation

The intensity limit calculation assumes an isotropic flux of LIPs or a flux with $\cos^2\theta$ angular distribution of the incident particles. The simulation of the fluxes and their verification are discussed below.

4.A.1 Simulation

The isotropic and $\cos^2\theta$ flux are simulated with GEANT4. In the simulation, LIPs are thrown (# of events = 10^9) from the outer cylindrical surface (see Fig. 4.1) enclosing the detector.

As the top and side surface has different orientation and surface area, the fraction of events generated at the two surfaces will be different. The general formula to determine the number of hit-points on a surface, for a flux Φ, is given by

$$N = \int \int \Phi \, \mathrm{d}S_n \mathrm{d}\omega, \tag{4.1}$$

where $\mathrm{d}S_n$ is the area component along the direction of incidence, $\mathrm{d}\omega$ is the solid angle. If N_1 and N_2 are the number of events to be generated on the top and side surface respectively for the flux Φ, the fraction of events on the top surface will be-

$$p = \frac{N_1}{N_1 + N_2} \tag{4.2}$$

and the same on the side surface will be equal to (1-p). We assume no LIPs entering the detector from beneath the earth. So no particles are shot from the bottom surface of the cylinder. The number N for a horizontal surface with surface area A using Eqn. 4.1 is given by -

$$\begin{aligned} N &= \int_0^{\pi/2} \Phi \, A \cos\theta \times 2\pi \sin\theta \mathrm{d}\theta \\ &= \int_0^{\pi/2} \Phi_0 \times A \cos\theta \times 2\pi \sin\theta \mathrm{d}\theta = \pi \Phi_0 A, \text{ when } \Phi = \Phi_0 \text{ (isotropic)} \\ &\text{or} \\ &= \int_0^{\pi/2} \Phi_0 \cos^2\theta \times A \cos\theta \times 2\pi \sin\theta \mathrm{d}\theta = \frac{\pi}{2} \Phi_0 A, \text{ when } \Phi = \Phi_0 \cos^2\theta \end{aligned} \tag{4.3}$$

The same for a vertical surface is given by-

$$\begin{aligned} N &= \int_{\theta=0}^{\pi/2}\int_{\phi=-\pi/2}^{+\pi/2} \Phi \times A \sin\theta\cos\phi \times \sin\theta \mathrm{d}\theta\mathrm{d}\phi \\ &= \int_{\theta=0}^{\pi/2}\int_{\phi=-\pi/2}^{+\pi/2} \Phi_0 \times A \sin\theta\cos\phi \times \sin\theta \mathrm{d}\theta\mathrm{d}\phi, \text{ when } \Phi = \Phi_0 \text{ (isotropic)} \\ &= \int_{\theta=0}^{\pi/2} \Phi_0 \times 2A \sin\theta \times \sin\theta \mathrm{d}\theta = \frac{\pi}{2}\Phi_0 A \end{aligned} \tag{4.4}$$

or

$$\begin{aligned} &= \int_{\theta=0}^{\pi/2}\int_{\phi=-\pi/2}^{+\pi/2} \Phi_0\cos^2\theta \times A \sin\theta\cos\phi \times \sin\theta \mathrm{d}\theta\mathrm{d}\phi, \text{ when } \Phi = \Phi_0\cos^2\theta \\ &= \int_{\theta=0}^{\pi/2} \Phi_0\cos^2\theta \times 2A \sin\theta \times \sin\theta \mathrm{d}\theta = \frac{\pi}{8}\Phi_0 A \end{aligned}$$

Eqn. 4.3 and Eqn. 4.4 can be used for any horizontal and vertical surface with surface area A. The equations when used for the top and side surface of the cylinder, they give N_1 and N_1 for isotropic ($\cos^2\theta$) flux to be equal to $\Phi_0\pi^2R^2$ ($\Phi_0\pi^2R^2/2$) and $\Phi_0\pi^2RH$ ($\Phi_0\pi^2RH/4$), respectively. Here R and H are the radius and height of the cylindrical surface enclosing the detector. Therefore, the fraction of events to be sampled on the top surface for isotropic ($\cos^2\theta$) flux is given by p = R/(R+H) (= 2R/(H+2R)) and the same for the side surface is 1-p.

As the particles incident on the detector, the positions and directions are recorded. The distributions of number of particle-hits as a function of θ on the top and side surface of the detector are given by the following equations.

Top surface:

$$\begin{aligned} \frac{\mathrm{d}N}{\mathrm{d}\theta} &= \Phi_0 \times \pi r^2 \cos\theta \times 2\pi \sin\theta; \text{ [for isotropic flux]} \\ &\text{or} \\ &= \Phi_0\cos^2\theta \times \pi r^2 \cos\theta \times 2\pi \sin\theta; \text{ [for } \Phi_0\cos^2\theta \text{ flux]} \end{aligned} \tag{4.5}$$

Surface	Analytic calculation	Simulation
Top	603,171	603,360
Side	396,823	396,638

Table 4.1: Comparison of expected number of hits on the detector-surfaces with simulation results for isotropic flux.

Side surface:

$$\frac{\mathrm{d}N}{\mathrm{d}\theta} = \Phi_0 \times 2rh \sin\theta \times 2\pi \sin\theta; \text{ [for isotropic flux]}$$
$$\text{or} \tag{4.6}$$
$$= \Phi_0 \cos^2\theta \times 2rh \sin\theta \times 2\pi \sin\theta; \text{ [for } \Phi_0 \cos^2\theta \text{ flux]}$$

Φ_0 can be determined by solving Eqn. 4.1 which normalizes the flux. If N is the number of particles shot from the cylindrical surface, $\Phi_0 = N/\pi^2(RH + R^2)$ for an isotropic flux, and $\Phi_0 = 4N/\pi^2(RH + 2R^2)$ for a $\cos^2\theta$ flux.

4.A.2 Results and verification

The distribution of hits on the top surface and the side surface, for both isotropic and $\cos^2\theta$ flux, are shown in Fig. 4.1 (a–d). The figures show that the distribution of hits on all surfaces of the detector are uniform for both isotropic and $\cos^2\theta$ flux i.e the density of hits are position-independent.

The fraction of hits on the top (or on the side) surface is different for the isotropic and the $\cos^2\theta$ case. Table 4.1 shows the comparison of number of hits on the surfaces expected from analytic calculation and simulation for a isotropic flux; the same for the $\cos^2\theta$ flux is shown in Table 4.2.

The hits expected on the top surface is 60.317 % for an isotropic flux and 75.247 % for a $\cos^2\theta$ flux. The fraction of hits we get from simulation are 60.336 % and 75.248 % for

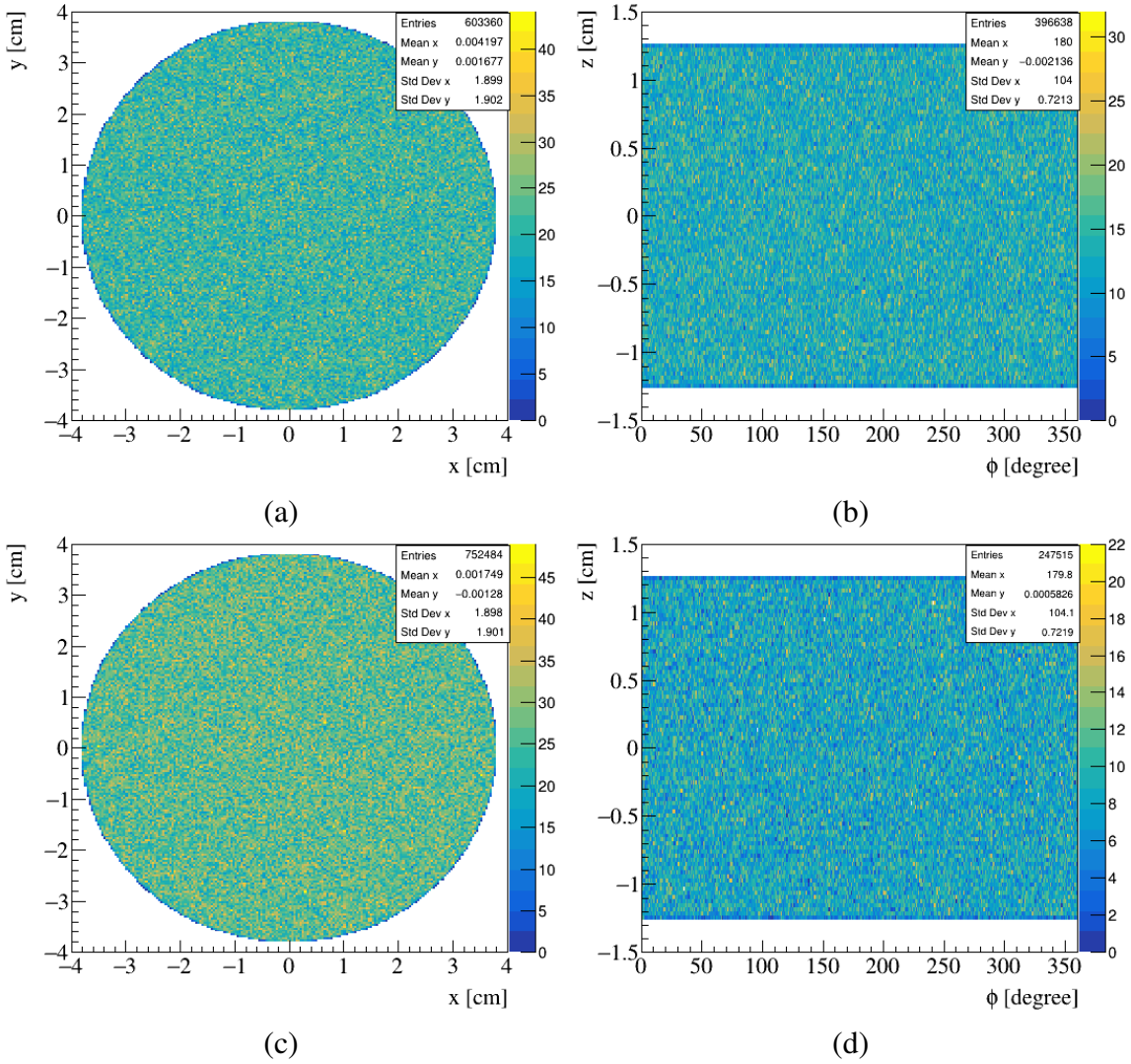

Figure 4.1: (a) Distribution of (x,y) cordinates as the particles enter the top surface for an isotropic flux. (b) Distribution of (z,ϕ) cordinates as the particles enter the side surface for an isotropic flux. (c) Distribution of (x,y) cordinates as the particles enter the top surface for a $\cos^2\theta$ flux. (d) Distribution of (z,ϕ) cordinates as the particles enter the side surface for a $\cos^2\theta$ flux. $\phi = \tan^{-1}(y/x)$, is the azimuthal coordinate of positions on the detector surface. For clarity, the hit distributions are plotted for 10^6 simulated events.

Surface	Analytic calculation	Simulation
Top	752,471	752,484
Side	247,523	247,515

Table 4.2: Comparison of expected number of hits on the detector-surfaces with simulation results for $\cos^2\theta$ flux.

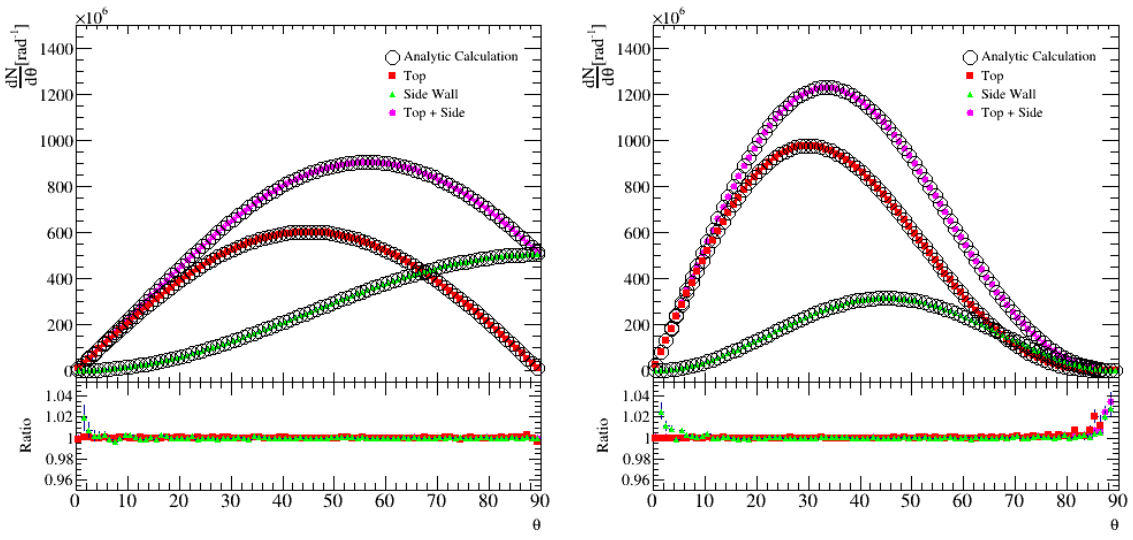

(a) (b)

Figure 4.2: (a) Number of hits as a function of incident θ for an isotropic flux. (b) Number of hits as a function of incident θ for a $\cos^2\theta$ flux. The open markers represent the results from the analytic calculation; the red and green markers show the results from simulation for top and side surface, respectively.

isotropic and $\cos^2\theta$ flux, respectively.

The number of particles entering the detector at different angles are also calculated. Figure 4.2 (a) and Figure 4.2 (b) shows the distribution of number of particles entering the detector at different angles of incidence for an isotropic flux and for a $\cos^2\theta$ flux, respectively. It can be seen that the results from simulation agrees with analytic calculations. The difference between the two is within 4 %.

Appendix 4.B Methods for calculation of straggling function of energy loss

This section discusses the different approaches which apeared in literature to calculate Probability Distribution Function (PDF) of energy loss. This is based on the section "Methods for obtaining straggling function" from the paper "Straggling in thin silicon detectors" by Hans Bichsel. An overview of different methods appeared in literature to calculate distribution of energy loss (referred to as "straggling function" in the paper) is given below.

Energy loss of charged particle as they pass through a medium is described by cross-section of energy loss in the medium. There are several methods to calculate probability distribution of energy loss from cross-sections. The methods, in order of appearance in literature, are the following :

1. Use of moments,
2. Mixed-method calculation,
3. Laplace transformation calculations,
4. Convolution calculations,
5. Monte Carlo calculations.

The folowing sections give some basic introduction to each methods.

4.B.1 Use of moments

Bohr introduced this method. It is assumed that the straggling of energy for a relatively thick absorber should be described by a Gaussian function with 1) mean energy loss,

$< \Delta >= tM_1$, where t is the absorber thickness and M1 is the first order moment of cross-section and 2) standard daviation σ given by $\sigma^2 = tM_2$; where M_2 is the second order moment of cross-section. A third moment M_3 was later used to obtain the asymmetry in distribution

4.B.2 Mixed-method calculation

Mulitple Mixed-method calculations over the years are used. One of the earlier ones was by Williams (1929). He used Gaussian function to approximate the stragling function for the collissons with enegy loss $E < E_1$ and convoluted it with another function for larger energy losses ($E \geq E_1$).

4.B.3 Laplace transformation calculations

In this method a equation describing the change in straggling function f(E) for small increament of the absorber thickness is derived. The equation is then solved with Laplace transformation to find f(E). Landau (Landau, L., 1944,J. Phys. (Moscow) VIII, 20) first used this method to calculate straggling function.

4.B.4 Convolution calculations

There are two components of the convolution calculations : 1) Cross-section of energy loss, $\sigma(E)$, in a single interaction 2) A Poisson distribution for number of interactions (n) :

$$P(n) = \frac{m^n e^{-m}}{n!}, \tag{4.7}$$

where m = average number of collisions = tM_0. The formula to calculate the straggling function is given by

$$\begin{aligned} f(t,E) &= \Sigma_{n=0}^{\infty} P(n)\sigma(E)^{*n} \\ &= \Sigma_{n=0}^{\infty} \frac{m^n e^{-m}}{n!}\sigma(E)^{*n} \end{aligned} \tag{4.8}$$

The method is discussed in Bichsel's paper. Allison and Cobb (W. W. M. Allison, J. H. Cobb, Annual Review of Nuclear and Particle Science 30, 253 (1980)) showed agreement between convolution-calulated energy loss distributins of pions and electron in 1.5 cm of argon / 7 % of CH_4.

4.B.5 Monte Carlo calculations

In this method, the passage of each particle through the detector is followed from one collision to the next. The distance traveled between collisions as well as the energy loss E in the collision is determined with random numbers, and the individual energy losses are added up to the total energy loss of the particle. The calculation is repeated for N particles, and a function f(E) is thus generated.

Monte Carlo, over the years, have been used in several experiments. Specific examples of PAI model being used in Monte Carlo can be found in M. Brigida, et al., Nucl. Instr. and Meth. A 533 (2004) 322 for silicon strip detectors and in Geant4 simulation package - Nuclear Instruments and Methods in Physics Research A 453 (2000) 597-605 for materials with atomic number between 1 to 100.

Chapter 5

Simulation of neutron backgrounds at JUSL

In any rare-event search experiments, including direct detection of dark matter, the understanding of backgrounds is crucial. Neutrons easily mimic dark matter signals and as a result, impact the sensitivity of dark matter search experiments. Therefore, the estimation of neutron background is an important component of the experiment. The amount of backgrounds could be very specific to the site chosen for the experiment, and also to the experimental configuration. This chapter presents a comprehensive study on the estimation of neutron background for a proposed India-based dark matter search experiment at Jaduguda Underground Science Laboratory (JUSL). The impact of the background on sensitivity is also estimated.

The chapter is organized as follows. Section 5.1 introduces the JUSL experiment; Section 5.2 outlines the sources of neutron backgrounds, Section 5.3 describes the simulation of these backgrounds and the results, and Section 5.4 discusses shielding configurations to reduce the backgrounds. Finally, in Section 5.5 the sensitivity under the assumption that

the neutrons are the only background in the experiment is estimated.

5.1 Jaduguda Underground Science Laboratory

A dark matter search experiment is propsed to be set up at a future facility of the India-based Neutrino Observatory (INO) [1]. The Dark Matter search at INO is commonly referred to as DINO. This will be a direct detection experiment with aims to search dark matter interactions in a crystalline detector medium. The possible detector materials likely to be explored in the experiment are inorganic scintillators like Cesium Iodide (CsI) and Gadolinium Galium Aluminium Garnet ($Gd_3Ga_3Al_2O_{12}$). A dark matter interaction in these crystals is expected to produce scintillations and phonons which will be measured in their respective sensors [2]. Both CsI and $Gd_3Ga_3Al_2O_{12}$ manifest good light yield of around 50 photons keV^{-1} [3, 4] which makes them suitable for low energy measurement in the detector.

The first phase of the DINO experiment involves understanding the background at a specific site and exploring the feasibility of dark matter search. To begin with, a small underground laboratory (approximately 5 m $\times$ 5 m $\times$ 2.2 m), named as Jaduguda Underground Science Laboratory (JUSL), is built at a depth of 555 m (~1600 mwe vertical rock overburden) in an existing mine of Uranium Corporation of India Limited (UCIL). The mine is located at Jaduguda in the state of Jharkhand, India. Figure 5.1 shows a picture of the experimenetal cavern at Jaduguda. The cavern is under a hill; the elevation map of the area around the laboratory is shown in Fig. 5.2. The location of the cavern is shown by a black dot in the figure. It is at a longitude of ~86.35 ^{o}E and latitude of ~22.65 ^{o}N.

Figure 5.1: The Jaduguda UCIL mine site. The experiment is proposed to happen inside this cavern.

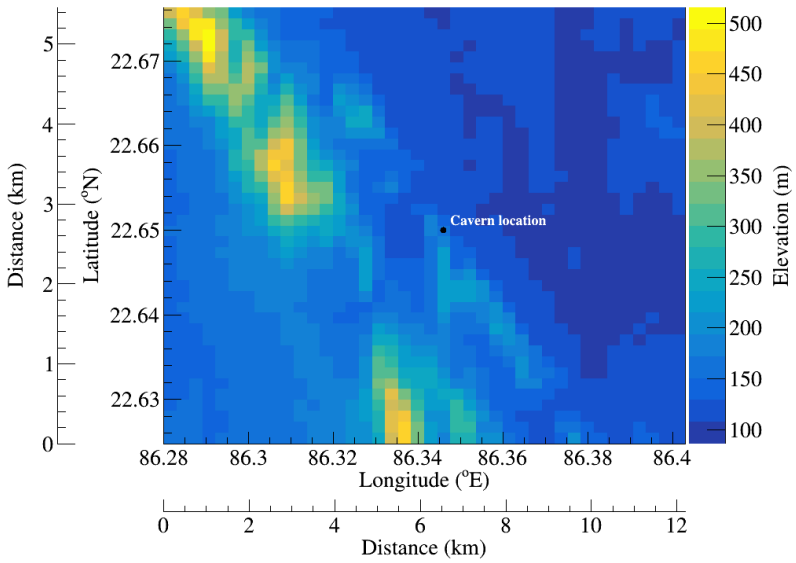

Figure 5.2: The elevation map of the area around JUSL [5]. The elevations at different longitudes (shown in the x-axis) and latitudes (shown in the x-axis) are shown by a color map with the axis shown on the right side of the figure. The longitudes and latitudes are also translated to distances and are shown in respective parallel axes. The black dot in the figure shows the location of the Jaduguda cavern.

5.2 Sources of neutron backgrounds

Neutrons are expected from two major sources: 1) radioactvity from the rock overburden and the shielding used in the experiment, and 2) interaction of cosmic ray particles with the rock and shielding material resulting in the production of neutrons [6, 7]. They are commonly referred to as radiogenic and cosmogenic neutrons, respectively.

5.2.1 Radiogenic neutrons

The radiogenic neutrons are primarily produced from two processes:

1. (α, n) **reaction:** The uranium and thorium traces present in the Jaduguda rock emits alpha particles. The interactions of these alpha particles with light nuclei cause the production of neutrons.

2. **Spontaneous fission:** Neutrons are also produced from the spontaneous fission of uranium and thorium isotopes.

5.2.2 Cosmogenic neutrons

Cosmogenic neutrons are produced primarily in cosmic muon induced interactions inside rock and shielding materials. Cosmic ray muons are produced at the upper atmosphere from interactions of primary cosmic rays with atmospheric nuclei. They are the most abundant charged particles at sea level with an average energy of 4 GeV and intensity $\sim$1 $cm^{-2}min^{-1}$. Muons produce neutrons through the following four processes.

1. Interaction with nuclei producing nuclear disintegration

2. Muon capture by nucleus followed by neutron emission

3. Neutron production by hadron from muon generated showers

4. Neutron production by gammas from muon generated electromagnetic showers

5.3 Estimation of neutron flux

5.3.1 Physics list

The neutron background is estimated using GEANT4 [8] (version: 10.02) based simulations. The reference physics list "`Shielding`" [9] is used. `Shielding` is based on `FTFP_BERT` physics list and `G4RadioactiveDecayPhysics`. `FTFP_BERT` is a recommended physics list for high energy physics applications, and `G4RadioactiveDecayPhysics` is used along with `FTFP_BERT` to handle various decay processes. The `Shielding` physics list uses high precision neutron model `NeutronHP` for simulation of low-energy neutron interactions. All together makes `Shielding` suitable for underground physics applications including the simulation study presented in this chapter.

In simulations, some electromagnetic processes require a threshold namely the "production cut" below which no secondaries will be produced [10]. The production cut prevents infrared divergence in the secondary productions; the default cut value of 0.7 mm is set for gammas and e^-/e^+.

5.3.2 Simulation of radiogenic neutrons

Simulation of radiogenic neutron flux involves multiple steps as summarized in Fig. 5.3 and also outlined here. This is followed by a detailed discussion on each component of the simulation.

- Neutron production from (α,n) and spontaneous fission depends on the composition of rock which comprises of radioactive elements like uranium and thorium, and

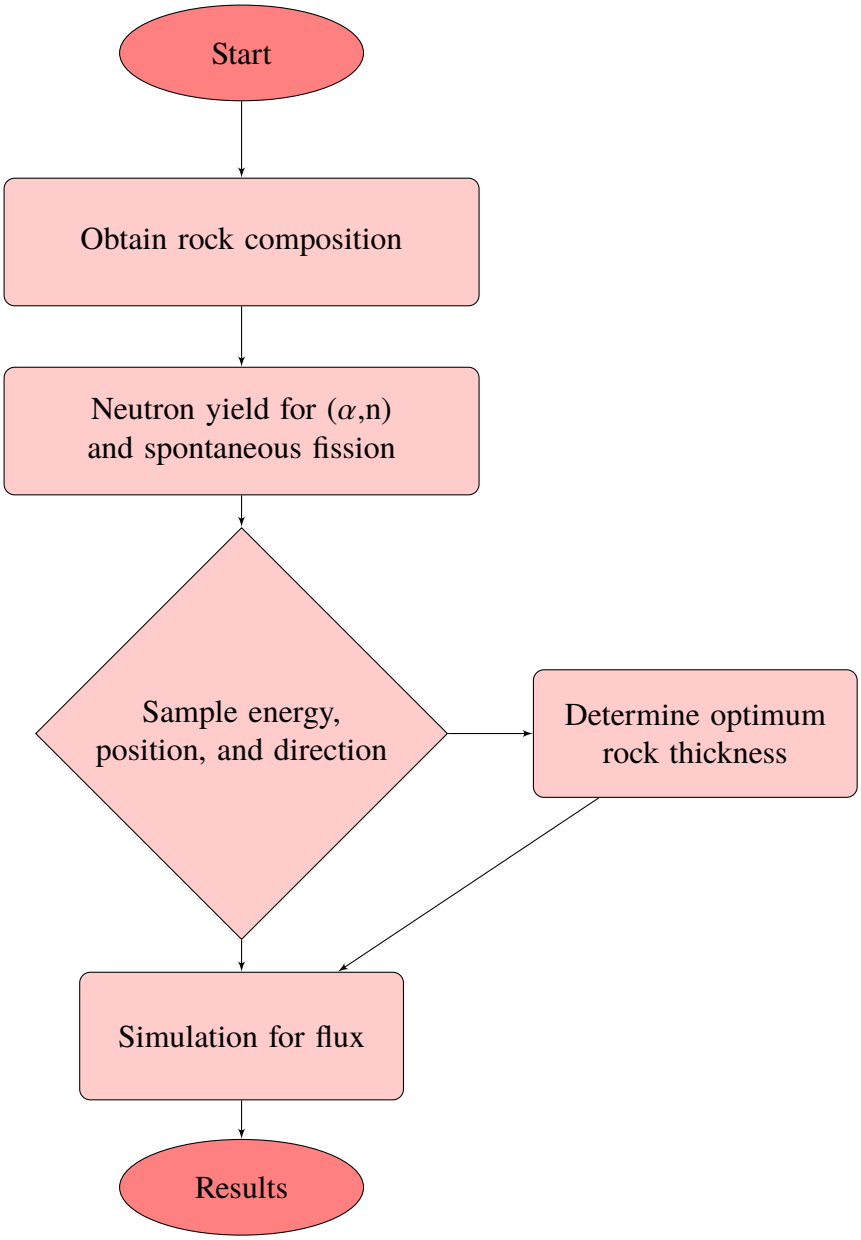

Figure 5.3: A flow diagram describing the methodology of radiogenic neutron flux calculation.

various other elements like Si, Al, O, etc. The elemental composition of the rock around JUSL is first obtained.

- The (α,n) and spontaneous-fission neutron yield and energy spectrum are caculated for the rock composition around JUSL. Here, the yield indicates the number of neutrons produced per gram of rock in a year from these two processes.
- Neutrons that are produced very far away may not reach the experimental cavern and therefore will have negligible contribution to the neutron flux. We consider only a "optimum thickness" of the rock around the JUSL cavern for the calculation of flux. This thickness is decided by studying the transmission of neutrons at various thicknesses of the rock. The rock thickness beyond which less than 0.5 % neutrons are transmitted is considered as the optimum thickness for the flux calculation.
- Neutrons reaching the experimental cavern are recorded and the number of neutrons incident per unit area per unit time is calculated as the flux.

Rock composition

Rock samples from various places around the laboratory cavern were analyzed for elemental / oxide contents by three methods: 1) Radiometric analysis, 2) Wet chemical analysis and 3) Inductively coupled plasma - optical emission spectroscopy (ICP-OES) analysis [5]. The composition of the rock as obtained from these analyses are shown in Table 5.1. The Jaduguda rock contains 8 ppm of uranium, 16 ppm of thorium along with other major components such as oxygen, silicon, and aluminum with the concentration of 47.8 %, 31.0 %, and 9.6 %, respectively [5].

Systematic uncertainties: The methods listed above to obtain the rock composition are associated with some systematic uncertainties. The radiometric measurement involves

Element	Conc (%)	Element	Conc (%)
U	0.0008	Na	1.2
Th	0.0016	K	2.2
^{40}K	0.00034	Ti	0.34
Si	31.0	P	0.079
O	47.8	Mn	0.023
Al	9.6	Mo	0.002
Fe	3.8	H	0.028
Ca	1.3	S	0.3
Mg	0.83	Others	< 1.5

Table 5.1: The composition of Jaduguda rock as obtained by wet-chemical, radiometric and ICP-OES analyses [5, 11].

quantitative gamma ray spectrometric analysis using a Thallium activated Sodium Iodide detector and has a systematic uncertainty of ~5-8 % due to the energy resolution and efficiency. In the wet chemical analysis, the oxide contents of the powdered rock samples were obtained by gravimetric analysis with an uncertainty of ~5-10 %. And, the ICP-OES method has an instrumental accuracy of 1 ppm. Based on the three analysis procedures, the uncertainties due to measurement methods alone were found to be ~10-15 %. Due to the variation among the rock samples and the results obtained by the three methods, the uncertainties in the elemental concentrations are effectively considered as ~15 % for all the elements, which is a conservative estimate, but combines the systematic uncertainties due to rock composition as well as the measurement procedures followed.

Neutron yield

Neutrons are produced via (α, n) reactions and spontaneous fission, as described in Section 5.2.1, from the uranium and thorium traces present in Jaduguda rock. However, all isotopes of uranium and thorium do not contribute significantly to the neutron yield. Isotopes of an element with large natural abundance and small half-lives are expected to

contribute dominantly to the yield. Table 5.2 shows the natural abundance and half-lives for α-decay and spontaneous fission of some isotopes of uranium and thorium. ^{238}U with the natural abundance of 99.27 % is the most prevalent isotope of uranium, therefore is considered in the yield estimation due to both (α, n) and spontaneous fission. On the other hand, ^{232}Th with the natural abundance of 99.98 % is considered for the (α, n) yield estimation, but not in the spontaneous fission for having a very large spontaneous-fission half-life.

Nucleus	Abundance [%]	α-decay half-life [Y]	SF half-life [Y]	Ref.
^{238}U	99.27	4.47×10^9	8.04×10^{15}	[12, 13]
^{235}U	0.72	7.04×10^8	1.8×10^{17}	[12, 14]
^{234}U	0.005	2.46×10^5	1.6×10^{16}	[14, 15]
^{232}Th	99.98	1.41×10^{10}	$> 10^{20}$	[12, 16]
^{230}Th	0.02	7.54×10^4	$> 1.5 \times 10^{17}$	[15, 16]

Table 5.2: The abundance and half-lives of uranium and thorium isotopes.

The ^{238}U and ^{232}Th isotopes have a long decay series as shown in Fig. 5.4; they undergo many α- and β-decays till the stable isotope of lead is reached. These decays are also accompanied by emission of γs. The α-particles created throughout the decays series participate in (α, n) reactions where they interact with the surrounding materials producing neutrons. In the decay series of ^{238}U, eight α-particles are emitted till the stable ^{206}Pb is reached. Similarly, six α-particles are emitted in the decay series of ^{232}Th. The neutron yield from (α, n) reactions is calculated using the program[1] developed by the authors of Ref. [17], where the rock composition shown in Table 5.1 is utilized. The yields for (α, n) reactions in the rock from ^{238}U and ^{232}Th are found to be 6.77 ± 1.12 yr^{-1}g^{-1} and 5.33 ± 0.90 yr^{-1}g^{-1}, respectively.

Systematic uncertainties: The uncertainty in the yields are estimated by varying the

[1]The program is available at http://neutronyield.usd.edu/.

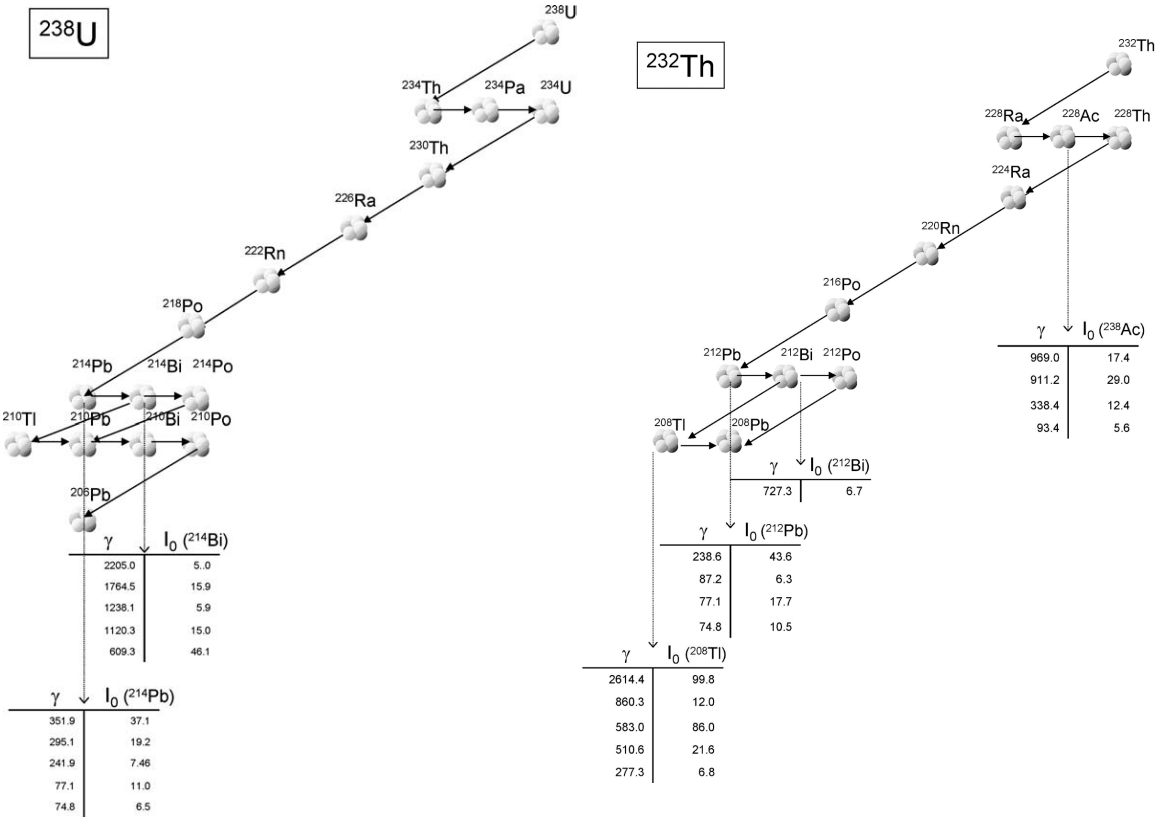

Figure 5.4: The decay series of ^{238}U and ^{232}Th [18]. The beta decays are shown by right arrows (→) and the alpha decays by the slanted downward arrows (↙). The high intensity (≥5 %) photons from a given decay are also shown, with energies in keV.

concentration of the important constituents in the rock i.e Si, O, U and Th by 15 %. The energy spectrum of (α, n)-reaction-produced neutrons in 1 g of Jaduguda rock is shown by the blue curve in Fig. 5.5. It is found that the neutrons from (α, n) reactions have energies up to 12 MeV.

Neutron yield due to spontaneous fission is obtained using the Watt function [19]. The Watt function is primarily used to explain fission due to thermal neutrons in ^{235}U [19]. But it holds good for spontaneous fission of other heavy nuclei as well. The Watt function is given as

$$W(a, b, E') = a\sqrt{\frac{4a}{\pi b}} \exp\left(-\frac{b}{4a} - aE'\right) \sinh(\sqrt{bE'}), \tag{5.1}$$

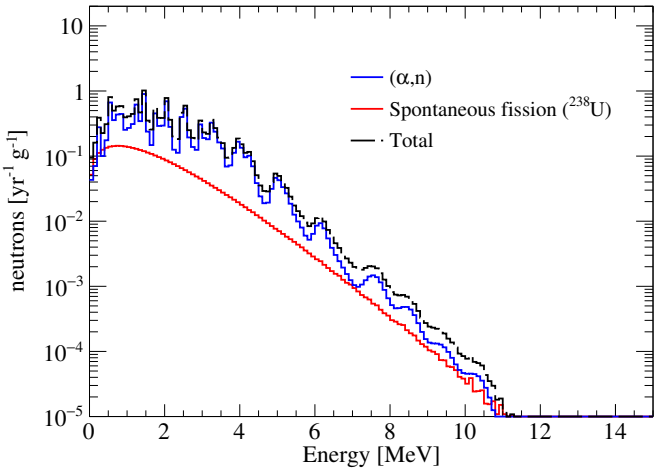

Figure 5.5: Energy distribution of neutrons produced per gram of Jaduguda rock in one year due to (α, n) reactions and ^{238}U spontaneous fission [5].

where $a = 1.54245$ MeV^{-1} and $b = 6.81057$ MeV^{-1} are constants (for ^{238}U) and E' is the secondary neutron energy [20]. The neutron yield due to spontaneous fission of ^{238}U in the rock, considering the neutron multiplicity ($\bar{\nu}$) for spontaneous fission of 2.01 [20], is found to be 3.43 ± 0.52 yr^{-1}g^{-1}.

Systematic uncertainty: The systematic uncertainty in the yield is due to the 15 % uncertainty in the concentration of ^{238}U. The energy spectrum of the spontaneous-fission-produced neutrons in 1 g of Jaduguda rock is shown by the red curve in Fig. 5.5.

The neutrons produced, from (α, n) reactions and spontaneous fission, with the energy distribution shown in Fig. 5.5 are propagated through the rock till they reach the experimental lab. Neutrons that are produced a few meters away from the rock-laboratory boundary, do not contribute to the neutron flux in the lab. The transmission of radiogenic neutrons through the rock for its different thicknesses is studied whereby an optimum thickness to be considered for the simulation to calculate flux is determined. The following section discusses the calculation of neutron transmission through Jaduguda rock.

Transmission of radiogenic neutrons through rock

To calculate the neutron transmission, a rock slab with a surface area of 1 m^2 and thickness of t m, where t is a variable, is defined in a GEANT4 simulation setup. Figure 5.6 shows a schematic diagram of the rock slab. The rock composition given in Table 5.1 is used to define the material of the slab. The 'primary' positions of the neutrons are sampled on the top surface in a 0.5 m × 0.5 m square area as shown by the white region in Fig. 5.6, and the primary directions of the particles are vertically downward, along the negative Z-axis direction. The energy of the neutrons is sampled from the distribution shown in Fig. 5.5.

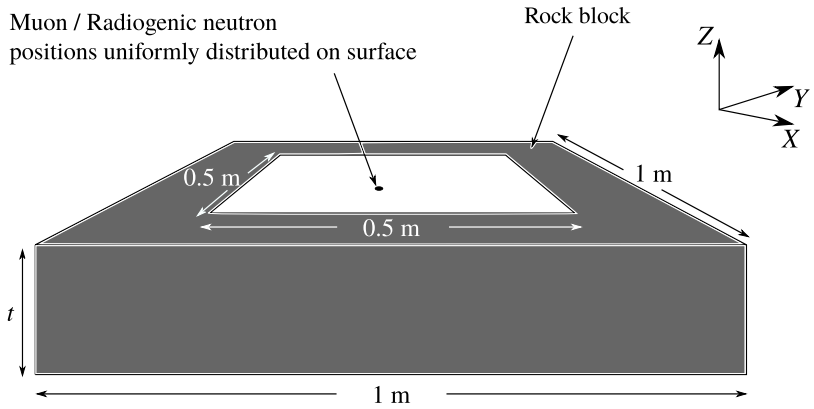

Figure 5.6: The rock slab model used in GEANT4 to calculate the transmission probability of neutrons [5]. The thickness t of the rock is varied and the length and breadth are fixed to 1 m.

After defining all the components for the simulation, neutron transmission is studied for various thicknesses of the rock. As neutrons propagate, they lose energy and get absorbed or scatter off. Neutrons coming out of the other side of the rock are recorded. The neutron transmission probability which is the ratio of the number of the number of neutrons coming out of the other side to the number of incident neutrons is calculated. This quantity, as a function of rock thickness, is shown in Figure 5.7. It can be seen that the neutron transmission decreases with thickness. Above a thickness of 1 m, the number of neutrons

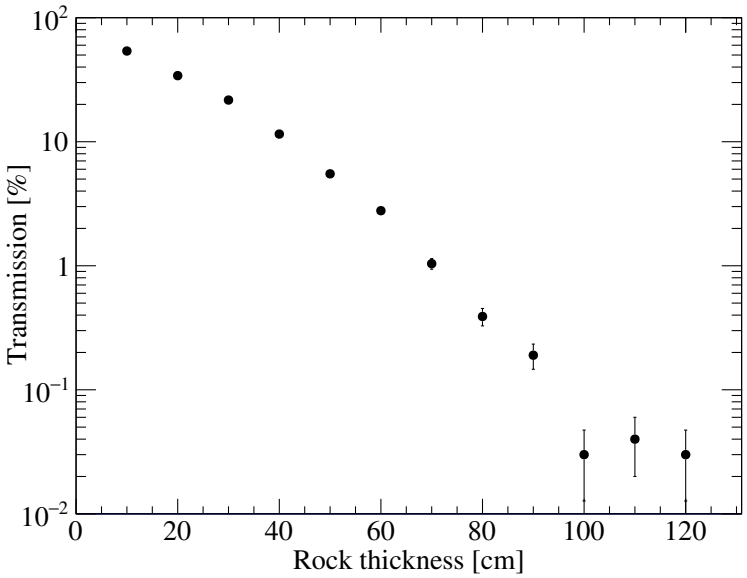

Figure 5.7: Radiogenic neutron transmission probability as a function of rock thickness [5]. The number of events generated for each thickness shown in the figure is 10^5.

that can traverse through the rock is less than 0.5 %. This suggests that the rock layer of 1 m thickness surrounding the laboratory cavern acts as an active material contributing to the radiogenic neutron flux. This thickness is considered in the simulation for radiogenic neutron-flux estimation.

Flux of radiogenic neutrons at JUSL

To estimate the radiogenic neutron flux, we first define the geometry which consists of an experimental lab and the surrounding rock. The experimental lab is defined in the shape of a cube with sides of 4 m; the cube is surrounded by 2 m thick rock from all sides. Figure 5.8 shows the schematic diagram of this geometry. The cubical lab region is named "Inner Cavern" and the rock surrounding the Inner Cavern is named "Outer Cavern". The "Outer Cavern" is divided into two parts (shaded by dark-grey and black region in Fig. 5.8) with each having the thickness of 1 m. The inner dark-grey region is the active material of the

rock determined in the previous section that contributes to the radiogenic neutron flux at JUSL.

Neutrons are thrown isotropically from the 1 m thick dark-grey region of the Outer Cavern in the simulation. The energy of the neutrons are sampled from the distribution shown in Fig. 5.5. Some neutrons propagate through the rock and some of them reach the experimental setup. These neutrons while propagating through rock can further produce neutrons.

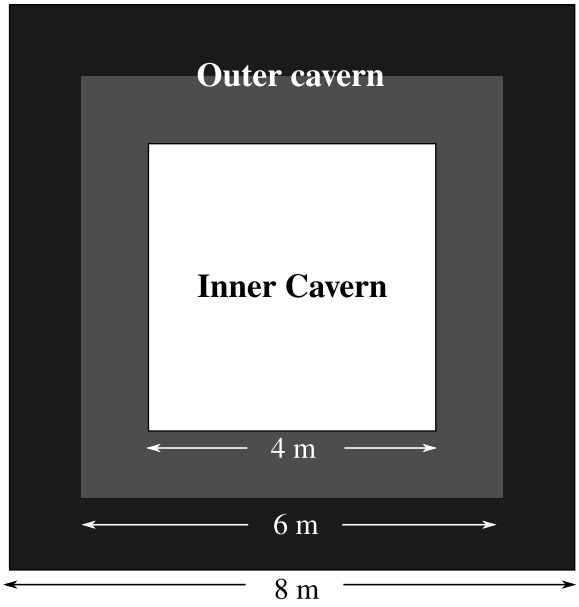

Figure 5.8: The side view schematic of the cavern as implemented in GEANT4 to calculate the radiogenic neutron flux [5].

Neutrons reaching the Inner Cavern, excluding those back-scattered from the matter in the cavern, are recorded. The flux of radiogenic neutrons reaching the laboratory as a function of energy is shown in Fig. 5.9. The total neutron flux above 100 keV energy is $1.12\,(\pm 0.13)\,\times 10^{-5}\,\mathrm{cm}^{-2}\,\mathrm{s}^{-1}$ (mean energy of 1.34 MeV) and above 1 MeV energy is $5.75\,(\pm 0.69)\times 10^{-6}\,\mathrm{cm}^{-2}\,\mathrm{s}^{-1}$ (mean energy of 2.18 MeV). The uncertainty shown in the parentheses include both statistical and systematic uncertainties. The systematic

uncertainties are calculated by propagating the uncertainty on elemental composition and density of the rock; the combined systematic uncertainty is around 10%.

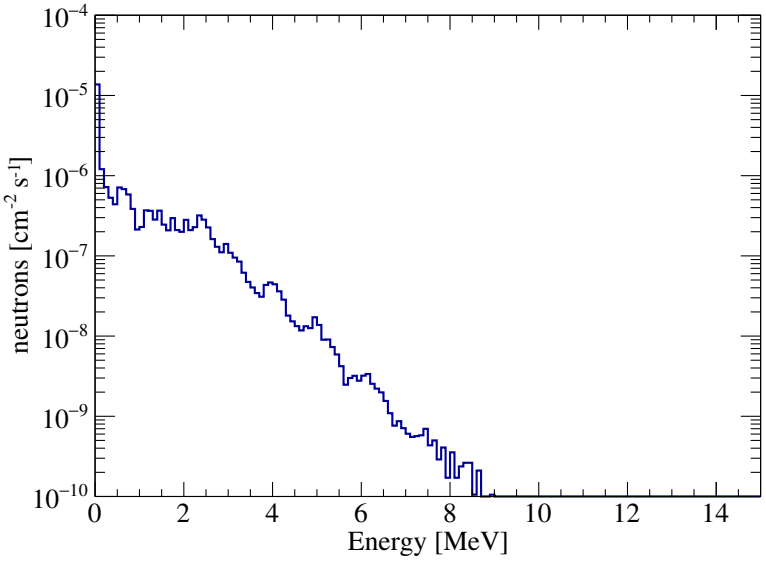

Figure 5.9: Flux of radiogenic neutrons reaching laboratory as a function of energy (Bin width = 0.1 MeV) [5].

Comparison with previous measurement at INO

There is an earlier study of radiogenic neutron flux estimation for INO at Bodi West Hills (BWH), Madurai, India [21]. The radiogenic flux estimated at JUSL is compared with the same at BWH. Figure 5.10 shows the comparison of the energy distribution of neutrons at the respective caverns. The total radiogenic flux at JUSL is $\sim 2.49\times10^{-05}$cm^{-2}s^{-1} and the same at BWH is $\sim 2.76\times10^{-06}$cm^{-2}s^{-1}. The larger flux at JUSL could be due to the fact that the rock has greater urnanium and thorium content at JUSL. The rock at JUSL has 8000 ppb of ^{238}U and 16000 ppb of ^{232}Th whereas the rock at BWH has 60 ppb of ^{238}U and 224 ppb of ^{232}Th.

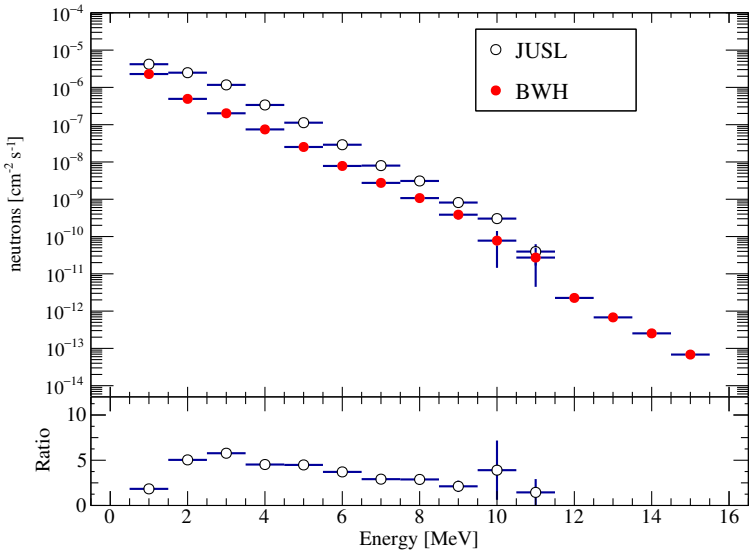

Figure 5.10: Comparison of energy distribution (bin width = 1 MeV) of radiogenic neutrons at JUSL and BWH.

5.3.3 Simulation of cosmogenic neutrons

The simulation to estimate cosmogenic neutron flux involves multiple steps. The steps of the simulation are shown in Fig. 5.11. This is followed by a detailed discussions on all aspects of the simulation and results. The simulation steps are as follows.

- In the simulation, muons are tracked from the JUSL hill surface till they reach the cavern. Therefore, the foremost step is to know the hill profile at Jaduguda. The hill profile comprising the information of latitude, longitude, and elevation of the Jaduguda area is obtained from Google Earth Pro [22]. The elevation map of the area around the laboratory is shown in Fig. 5.2.

- Energy and angular distribution of muons at the hill-surface level is generated using Gaisser's formula [23, 24] (see equation 5.2 of this chapter).

- Jaduguda mine has a 555 m rock overburden. Muons with small energies are

not expected to traverse this depth. The minimum energy required to reach the experimental cavern is determined by studying the maximum distance muon traverses through Jaduguda rock at different energies.

- Muon interactions in the rock can cause deviation from a straightline trajectory. The maximum lateral displacements of muons at different energies are calculated to determine a "solid-angle acceptance" for the muon trajectories. If the direction of a muon at the hill's surface does not fall within this solid-angle acceptance, the particle has a negligible possibility to reach the experimental cavern. Such muons are not tracked in the simulation to save simulation time and resources.

- The neutrons that are produced very far away, because of the many interactions with the rock-material along the way, are not expected to reach the Jaduguda lab. The transmission of neutrons through rock of different thicknesses are studied to find a "optimum thickness" to be considered for the tracking of neutrons.

- Muons are tracked from the Jaduguda hill-surface and the neutrons are tracked from the sites of their prodution, if produced within the optimum rock thickness (measured from the boundary of the experimental lab), till they reach the experimental lab. The muons and neutrons reaching the lab are recorded and the number of them that are incident per unit area per unit time is calculated as flux.

Cosmic muon event generation

At the begining of an event, it is required to provide the position, direction and energy of muon at the hill surface as inputs to the simulation. The primary positions are sampled uniformly on the hill surface within a circular boundary (see Fig. 5.12) of 1.5 km radius. The latitude, longitude, and elevation information of the Jaduguda area are obtained using

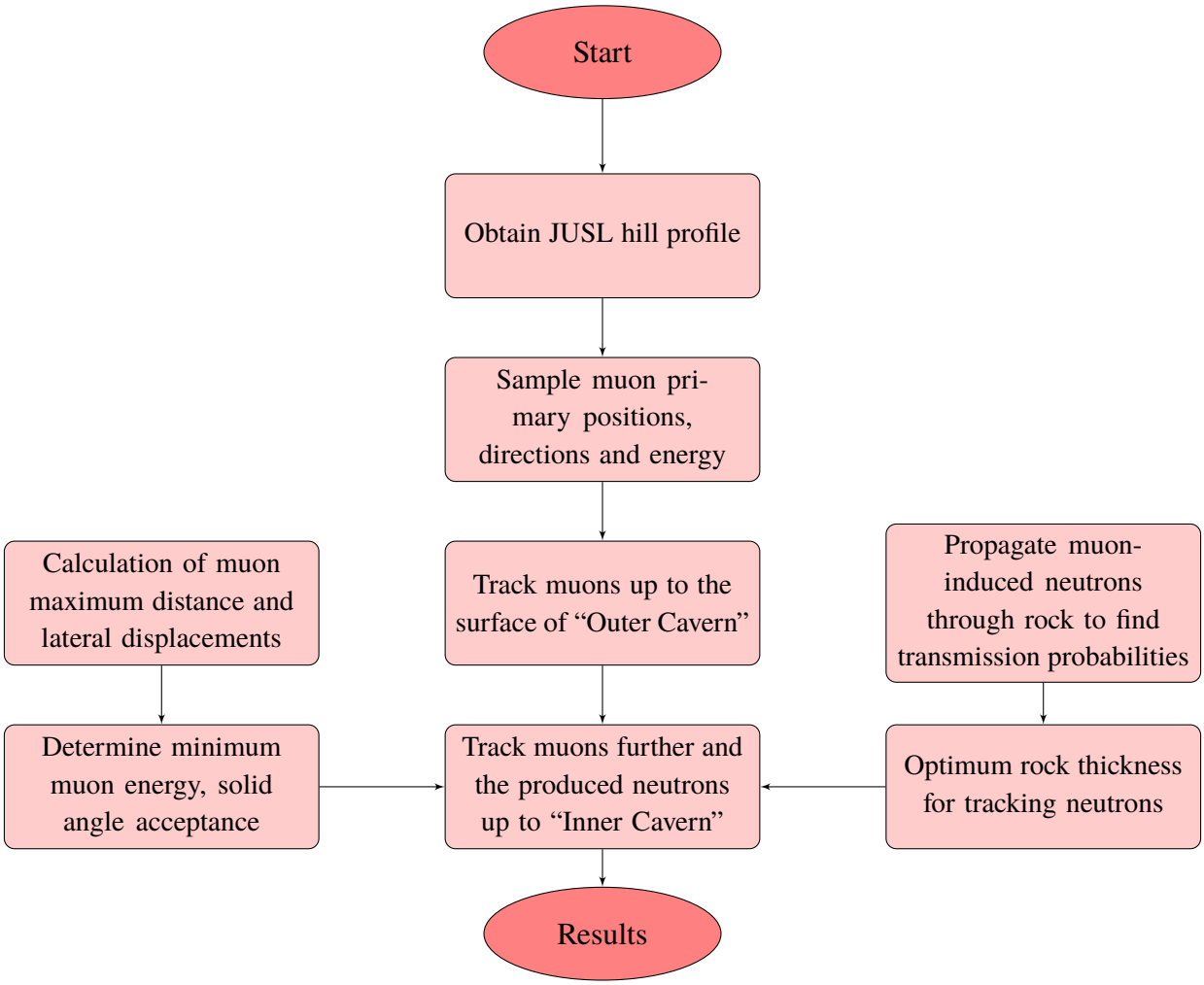

Figure 5.11: A flow diagram describing the methodology of cosmogenic neutron flux calculation.

Google Earth Pro [22]. The altitude dependence of muon flux is ignored. The topological profile is shown in Fig. 5.2. The energy and incident angle are sampled from the Gaisser's formula [23, 24].

Gaisser's parameterization describes the energy and angular distribution of muons on the ground surface under the assumption that the decay of muons is negligible and the curvature of the earth can be neglected (zenith angle $\theta_z < 70^o$). The flux of muons at the earth's surface as per Gaisser's parameterization is given by

$$\frac{\mathrm{d}^2 N_\mu}{\mathrm{d}E_\mu \mathrm{d}\Omega} \approx \frac{0.14 E_\mu^{-2,7}}{\mathrm{cm}^2\,\mathrm{s}\,\mathrm{sr}\,\mathrm{GeV}} \times \left[\frac{1}{1 + \frac{1.1 E_\mu \cos\theta_z}{\epsilon_\pi}} + \frac{\eta}{1 + \frac{1.1 E_\mu \cos\theta_z}{\epsilon_K}} \right], \tag{5.2}$$

where θ_z is the zenith angle, E_μ is the energy of the muon, N_μ is the number of muons, Ω is the solid angle, $\epsilon_\pi = 115$ GeV, $\epsilon_K = 850$ GeV and $\eta = 0.054$.

Muons with energies between 300 GeV and 15 TeV are considered in the simulation. The lower bound of this energy range is determined from a simulation study (described in the next section) on the maximum distances muons travel through Jaduguda rock at different energy of the particle. The contribution of very high energy (above few ~TeVs) muons to the flux is very small; the highest muon energy of 15 TeV is considered in the simulation. Both μ^+ and μ^- events are generated. Muons impinging on the surface at $\theta_z < 70^\circ$ are considered, and the azimuthal angle ϕ is sampled from uniform distribution between 0 and 2π.

Muon lateral displacement and maximum distance

With start-point positions obtained from hill profile and energy and direction information from Gaisser's formula, one can in principle simulate muons and the produced particles from muon interactions with the rock. However, simulation of all possible trajectories

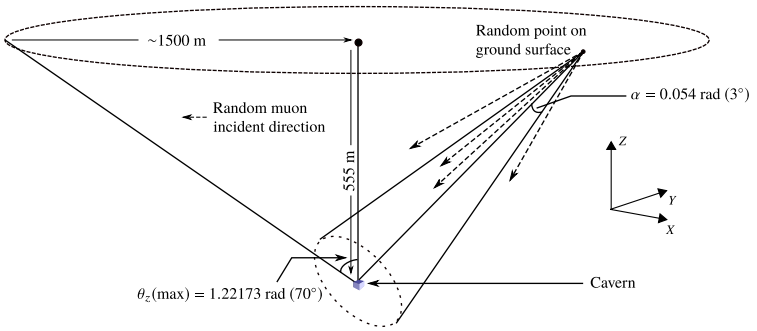

Figure 5.12: Schematic diagram describing the methodology of calculating muon flux at the cavern [5].

originating from the hill-surface, where most of them are not expected to reach the cavern, is time-consuming and computationally expensive. A simulation strategy is developed using the muon lateral-displacements and maximum traveled distances in the rock to counter this difficulty and is discussed in this section.

To reach the cavern from the surface, cosmic muons have to be quite energetic. Moreover, muons interact with the earth/rock and undergo scattering. Their initial direction of propagation is altered and their expected position at a depth is displaced. By calculating the maximum distance traversed by muons of a given energy, we can estimate the minimum energy required by muons to reach the cavern. Muons with different fixed energies were made to pass through a cube of rock of side 6 km along the $-Z$ direction. The maximum distance traversed and lateral displacement were calculated. The results are shown in Fig. 5.13(a-d). It can be noted from Fig. 5.13(a) and 5.13(b) that the average lateral displacement saturates to $\sim$ 2.3 m, but the maximum lateral displacement can be as high as 30 m. Therefore, muons with the incident direction within a cone having an axis as the line connecting the point of incidence to the center of the cavern and radius of 30 m (cone opening angle $\alpha \sim 3.1°$; this also translates to the solid angle of 0.003π sr) are simulated. In other words, muons with incident directions lying within the solid angle of 0.003π sr are

accepted for tracking (see Fig. 5.12) in the simulation. The other muons are not simulated and are counted as incident on the hill surface but not reaching the cavern. Fig. 5.13(c) and 5.13(d) show that the minimum energy required for muons so that they can reach the cavern (depth 555 m) is around 300 GeV. Therefore, we do not consider cosmic muons of energy less than 300 GeV in our simulation.

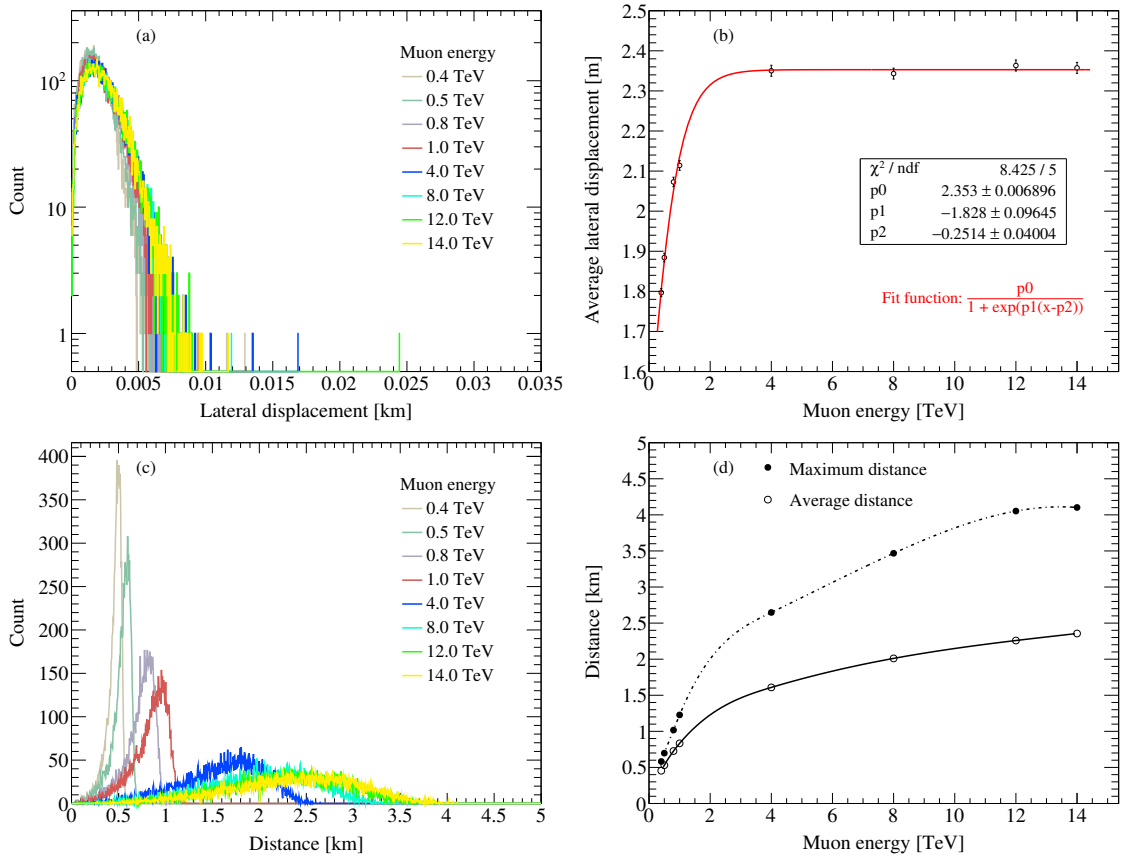

Figure 5.13: (a) Lateral displacement distribution of muons from their initial direction of propagation in the rock [5]. (b) Average lateral displacement as a function of muon energy [5]. (c) Distribution of distance traversed in the rock by muons of different incident energies [5]. (d) Maximum and average distance traversed by muons as a function of energy [5].

Calculation of muon flux at the cavern

Cosmic muon events, following the strategy devised in the previous section, are generated at the surface of the hill and then the muons are tracked till they reach the surface of the "Outer cavern" (see Fig. 5.8 for "Outer cavern"). Muons along the way interact with the rock and produces neutrons. However, the neutrons produced only within a finite element of the rock are tracked as will be discussed in the next section of this chapter. The position, direction and energy of the muons as they enter the Outer cavern are recorded. The energy

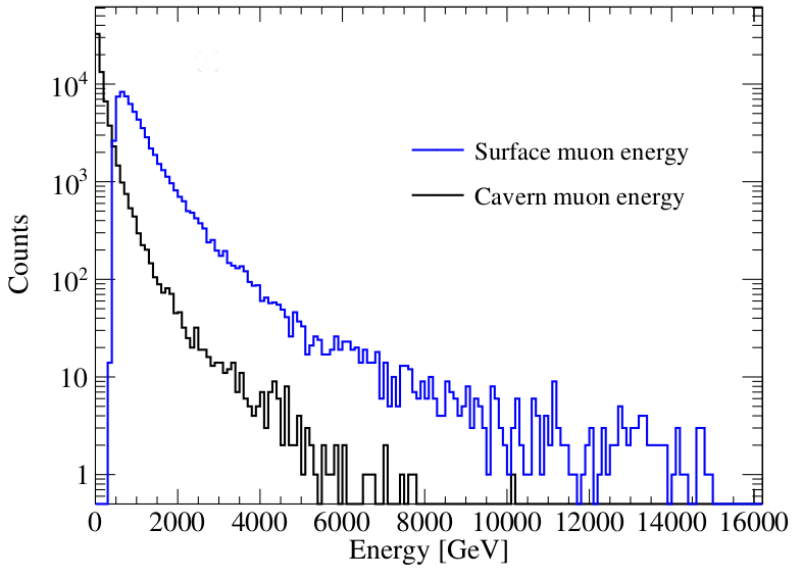

Figure 5.14: Energy distribution (bin width = 100 GeV) of muons at the surface and after reaching the cavern [5].

distribution of muons as they reach the cavern surface compared to the distribution at the hill surface is shown in Fig. 5.14.

It is found that the flux of muons on the top surface of the outer cavern is $4.49(\pm 0.25) \times 10^{-7}\,\mathrm{cm}^{-2}\,\mathrm{s}^{-1}$. The density of the rock ($2.89\,\mathrm{g/cm}^3$) was varied by ~2 % to see the change in the muon flux at the cavern. The flux was observed to change by about 5.5 %. This has

been considered as the systematic uncertainty on the flux.

Transmission of cosmogenic neutrons through rock

The neutrons produced from muon interaction gets attenuated in the rock similar to the case of radiogenic neutrons. Therefore, only a rock element with finite size will contribute to the flux of cosmogenic neutron in the laboratory. A study similar to that described in Section 5.3.2 is performed for finding the rock thickness to be considered for simulating the muon-induced neutron flux in the experimental hall.

The rock geometry shown in Fig. 5.6 is used for the simulation. The energy distribution of muons at the surface of the outer cavern shown in Fig. 5.14 (black histogram) is used. Muons are propagated from random positions on a plane of dimension (0.5 m $\times$ 0.5 m) (Fig. 5.6) through the rock in the $-Z$ direction. The muon interactions with rock generate neutrons. The neutrons coming out on the other side of the rock are recorded. The simulation is repeated for different rock thicknesses (t = 10 cm, 25 cm, 50 cm, 75 cm, 100 cm, 150 cm, 200 cm, 250 cm, 325 cm and 400 cm).

The number of neutrons produced (N_{prod}) and the number of neutrons exiting (N_{out}) from the other side of the rock as a function of its thickness is given in Fig. 5.15 (a). As the rock thickness increases, N_{prod} also increases due to the increase in the probability of interaction. Whereas, N_{out} first increases with thickness and then saturates at a thickness of ~200 cm. The ratio of the number of neutrons coming out on the other side of the rock to the number of neutrons produced in the rock ($N_{\text{out}}/N_{\text{prod}}$), as a function of rock thickness is shown in Fig. 5.15(b). As the rock thickness increases the ratio decreases, and it reduces to 0.07 for a rock of thickness 200 cm.

Neutron energy spectra at production and after transmission through the rock of thickness 200 cm are shown in Fig. 5.15(c). The production rate of neutrons for 200 cm rock

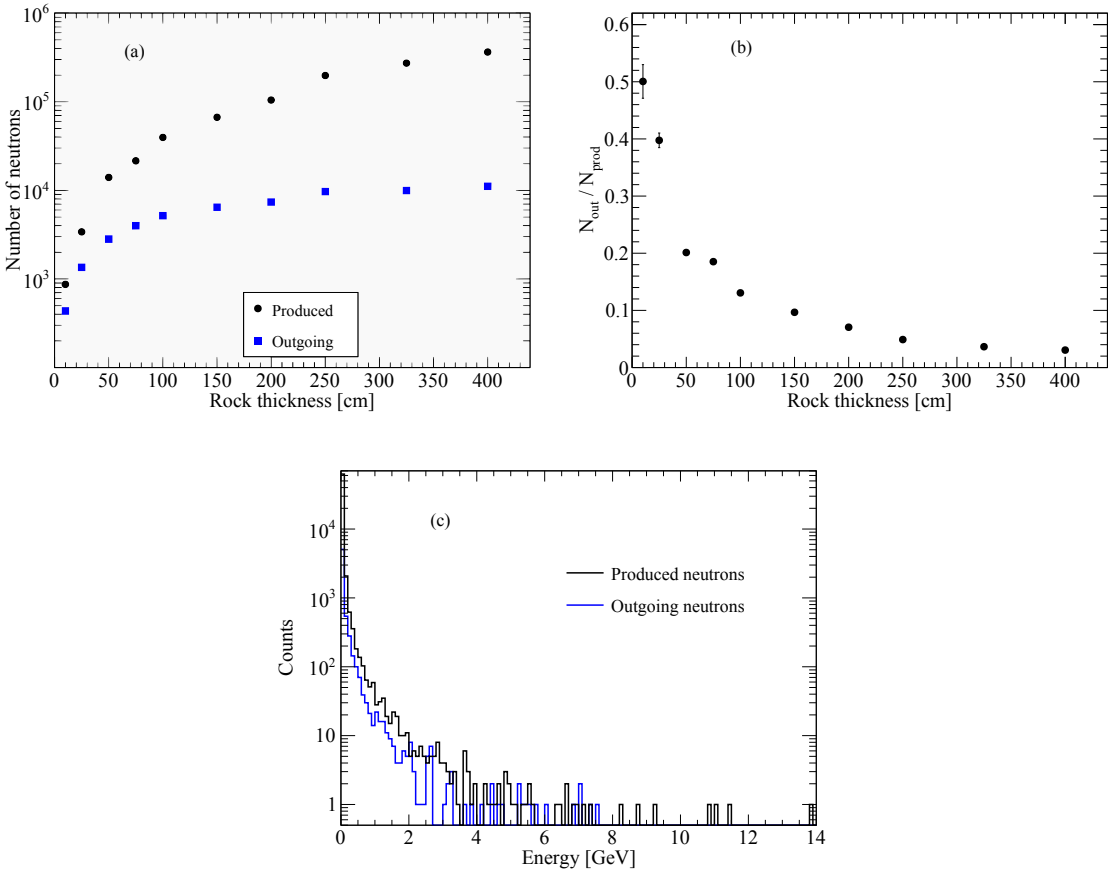

Figure 5.15: (a) Neutron produced from muon interaction and the neutrons coming out on other side of the rock as a function of rock thickness considered in the simulations [5]. (b) Ratio of outgoing neutrons to the produced neutrons in the rock as a function of rock thickness [5]. (c) The energy spectra of produced neutrons (bin width = 100 MeV) and outgoing neutrons [5].

thickness is around 0.1 neutron/muon.

Flux of muon induced neutrons at JUSL

To estimate the cosmogenic neutron background at the JUSL, the muon flux obtained at the surface of the outer cavern is used. The muon events are re-sampled from different positions on the five surfaces of the 2 m thick rock around the cavern as shown in Fig. 5.16

(front and back surfaces are not shown in the figure). Muons are allowed to propagate through the rock and reach the cavern. There are no muons propagating from the bottom side. While going through the rock, they generate neutrons and other shower particles like hadrons, gamma, and electrons which then enter the laboratory. Some of the neutrons get absorbed in the rock itself.

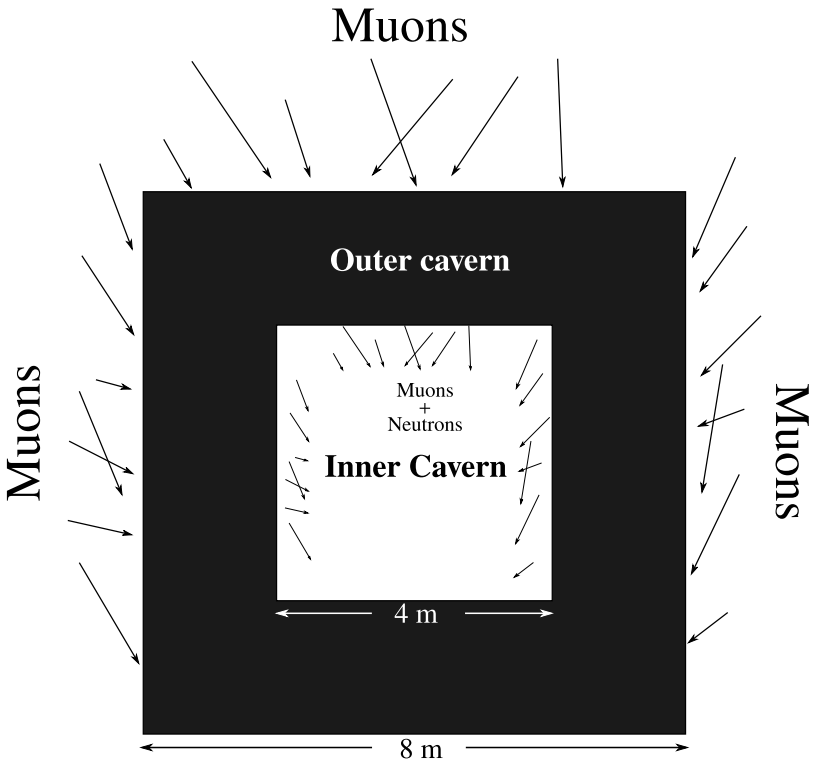

Figure 5.16: Schematic diagram of the geometry used for simulation [5]. The white region, labeled as Inner Cavern, is the laboratory. The rock surrounding the laboratory region is shown in black.

The flux of neutrons reaching the cavern is shown in Fig. 5.17. It can be seen that the neutrons produced in rock have energies up to 10s of GeVs. The muon induced neutron flux in the cavern is found to be $0.93(\pm 0.05) \times 10^{-8}\,\mathrm{cm}^{-2}\ \mathrm{s}^{-1}$ with no energy threshold and $7.25(\pm 0.40) \times 10^{-9}\,\mathrm{cm}^{-2}\ \mathrm{s}^{-1}$ above 1 MeV. The systematic uncertainty, which is around 5.5 %, is due to the variation of the rock density.

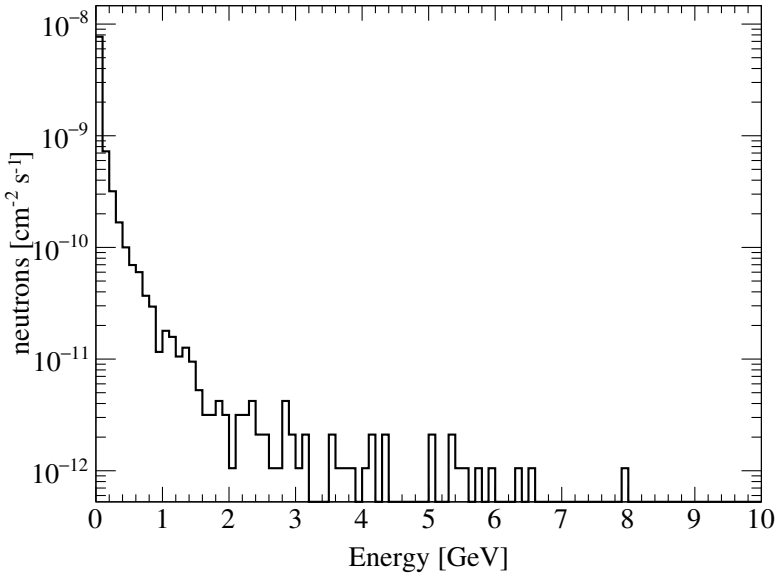

Figure 5.17: The flux of muon induced neutrons (bin width = 100 MeV) in the Inner cavern [5].

5.3.4 Total neutron flux at JUSL

The radiogenic and the cosmogenic neutron flux, plotted as a function of energy, reaching the Jaduguda laboratory is shown in Fig. 5.18. The figure shows that for energies less than ~10 MeV, neutrons flux from radiogenic neutrons is around 3 orders of magnitude greater than the muon-induced neutron flux. However, above 10 MeV energy, only muon-induced neutrons contribute to the spectrum.

For neutrons above 1 MeV energy, the flux of radiogenic neutrons is 5.75 (±0.69) × 10^{-6} cm^{-2} s^{-1}, whereas the flux of neutrons produced by muon interaction in the rock is 7.25 (±0.40) × 10^{-9} cm^{-2}s^{-1}. Therefore, the total neutron flux reaching the cavern/laboratory above 1 MeV energy threshold is 5.76 (±0.69) × 10^{-6} cm^{-2}s^{-1}. The uncertainties on radiogenic and cosmogenic neutron flux are added in quadrature to find the uncertainties on the total flux. The flux values are comparable with neutron flux estimates

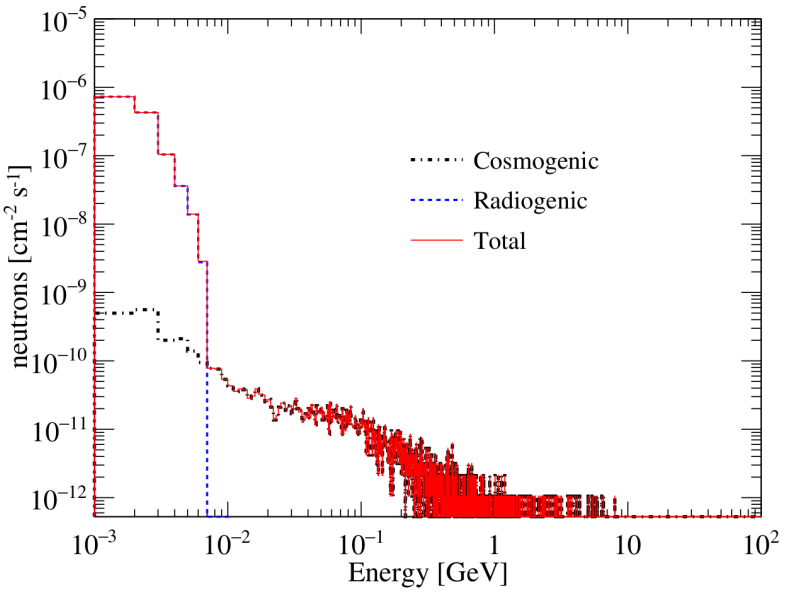

Figure 5.18: Total neutron flux (bin width = 1 MeV) due to radiogenic and cosmogenic sources expected at the cavern shown as a function of energy [5].

at Boulby and WIPP salt mines [25, 26].

5.4 Shielding combinations to reduce neutron flux

The neutron background calculated in the previous section can be reduced with shielding. Experiments typically use layers of active and passive shields to suppress various backgrounds that can produce events in the detector. Active shielding can veto muons and associated neutrons. Passive shielding systems consist of lead (Pb) or iron (Fe) for shielding gammas, hydrocarbons for moderating neutrons, and copper for attenuation of gammas.

To find the optimal shielding setup for the reduction of neutron backgrounds, various combinations of Pb and Polypropylene layers are probed in simulation. For simplicity, each layer is assumed to have the shape of a rectangular slab with 1 m $\times$ 1 m surface area;

the thickness of the layers are varied in the simulation. Figure 5.19 shows a schematic diagram (side view) of the shielding layers. There is an air gap of 1 cm between each layer. Neutrons are thrown perpendicularly to the shielding layers.

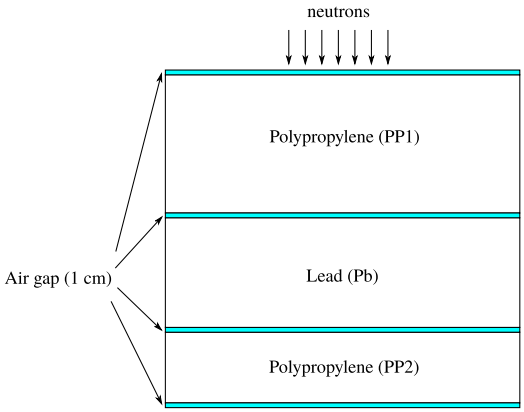

Figure 5.19: Rectangular shielding layers used for simulation [5]. The thicknesses of Pb and PP2 are varied.

5.4.1 Reduction of radiogenic neutron flux

Radiogenic neutrons with the energy distribution shown in Fig. 5.9 are passed through the shielding layers of Fig. 5.19. It is found from the simulation that almost all the radiogenic neutrons are stopped by a 40 cm thick polypropylene layer; the amount of neutrons that reaches the Pb surface is negligible. In other words, the radiogenic neutrons can be shielded using only a polypropylene layer of 40 cm thickness.

5.4.2 Reduction of muon induced neutron flux

The effect of the shielding to reduce the muon induced neutron flux is also studied. The muon induced neutrons with the energy distribution shown in Fig. 5.17 are passed through the shielding layers. The thickness of the first polypropylene layer is fixed to 40 cm, but

the thicknesses of the other two layers (Pb and another polypropylene layer) are varied. Neutrons crossing the boundary of each layer are recorded.

The first polypropylene layer stops about 47 % of the incident cosmogenic neutrons. The neutrons that escape the polypropylene layer reach the subsequent layer of lead. It is observed that a large number of neutrons are produced in lead from interactions initiated by incoming neutrons. However, lead is useful to shield gammas and therefore is part of any shielding configuration. A second polypropylene layer (PP2) is kept after lead to attenuate the neutrons produced in the lead layer. Table 5.3 shows the results from various shielding configurations (labeled as CFG-1, CFG-2,...). It is found that CFG-4 provides the best neutron reduction.

Table 5.3: Different shielding configurations and their effectiveness [5]. Uncertainties shown are statistical only.

Configuration	Thicknesses of different shielding layers (cm)			Transmission (%)
	PP1	Pb	PP2	
CFG-1	40	–	–	52.31 ± 0.72
CFG-2	40	30	–	136.3 ± 1.2
CFG-3	40	30	10	32.52 ± 0.57
CFG-4	40	30	20	10.44 ± 0.32
CFG-5	40	25	20	12.36 ± 0.35

It should be also noted that the simulations performed with the shielding layers do not consider neutrons produced from muon interactions in the layers. If these neutrons are also taken into account, CFG-4 may not be the best configuration. The lower the thickness of lead, the lower is the number of muon-induced neutrons. Since we do not have a proper idea of the gamma background yet at the experimental site, a conservative choice of 30 cm thickness for lead is made. With more information from background measurements, the configuration can be better optimized using materials with atomic numbers (Z) lower than

lead.

Neutrons, gamma, muons, and electrons are the major backgrounds in a typical experimental setup. Muons and neutrons can also interact with the detector/shielding materials to produce more neutrons. We investigate the effect of shielding and calculate neutron flux at a detector using a simple geometry. The shielding design is based on the dimensions of shielding materials obtained from CFG-4 shown in Table 5.3. The geometry of the rectangular rock element and the experimental setup is given in Figure 5.20. The experimental setup consists of a cylindrical CsI crystal with a radius of 2.2 cm and a height of 4 cm. Surrounding the crystal there are cylindrical layers of covering and shielding materials with various thicknesses: Teflon (0.05 cm), copper (0.6 cm), polypropylene (20 cm, PP2), Pb (30 cm), polypropylene (40 cm, PP1). There is a rock block with a thickness of 200 cm surrounding this experimental set up with $\sim$ 100 cm of an air gap between them. It has been tested that the detector and shielding does not alter the muon flux inside the cavern significantly.

Muons are re-sampled uniformly on the five faces of the outer cavern as shown in Figure 5.20. The incident muons and muon induced neutrons are tracked through the successive layers of shielding. Neutrons produced in each layer of shielding are recorded. Neutrons are produced from both muon-initiated interactions and neutron interactions. The neutron rate in each layer is calculated. Here, the neutron rate in a layer is defined as the number of neutrons that will be seen in unit volume (in cm^3) of the layer in unit time (in second) where these neutrons include those produced in the same layer and those coming from adjacent layers. Table 5.4 shows the rates in different shielding layers.

Only a fraction of neutrons produced in each layer reach the next layer of the shielding. Others either get absorbed or scatter off. The neutrons which get reflected back from a layer (i) can be absorbed by the previous layer (ii) get transmitted out of the setup or (iii) get

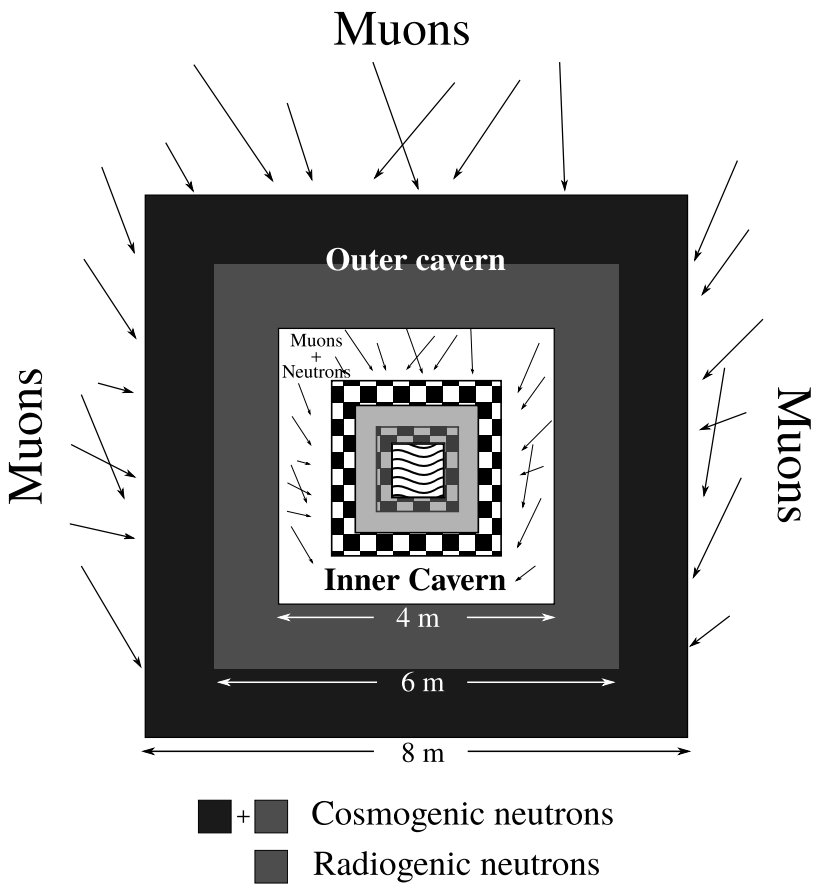

Figure 5.20: Schematic diagram of geometry used for simulation [5]. The crystal, teflon and copper layers are shown together with wave pattern, PP2 is the black and light gray checkered region, Pb is the light grey region and PP1 is the black and white checkered region. The radiogenic neutrons that reach the experimental cavern originate mainly from the dark grey rectangular region (thickness 1 m), and the cosmogenic neutrons from both the dark grey rectangular region and the black region (combined thickness 2 m).

reflected back again to the same layer. These effects are taken into consideration to avoid multiple counting. Neutrons reaching each layer of the detector include neutrons produced in all previous layers. For instance, neutrons reaching the copper layer include neutrons produced in rock, polypropylene and lead.

The current of cosmogenic neutrons, which is defined as the number of neutrons crossing per cm^2 of the top surface of a layer per unit second, is estimated for different layers. It

Table 5.4: The rate of neutrons (see defintion in text) in different layers [5]. This rate includes neutrons from muon interactions, neutrons from other layers and within. Uncertainties shown are statistical only.

Material	Neutron rate ($cm^{-3}\ s^{-1}$)
PP1	$2.05(\pm0.04) \times 10^{-10}$
Pb	$1.72(\pm0.01) \times 10^{-8}$
PP2	$6.64(\pm0.06) \times 10^{-10}$

is calculated with the number of simulated events equivalent to 20 physical days. The neutron current as a function of energy is shown in Fig. 5.21 and the total neutron current (integrated over energy) that reaches the top surface of each layer of the experimental setup is shown in Table 5.5. The table also shows the mean energies of neutrons crossing each layer.

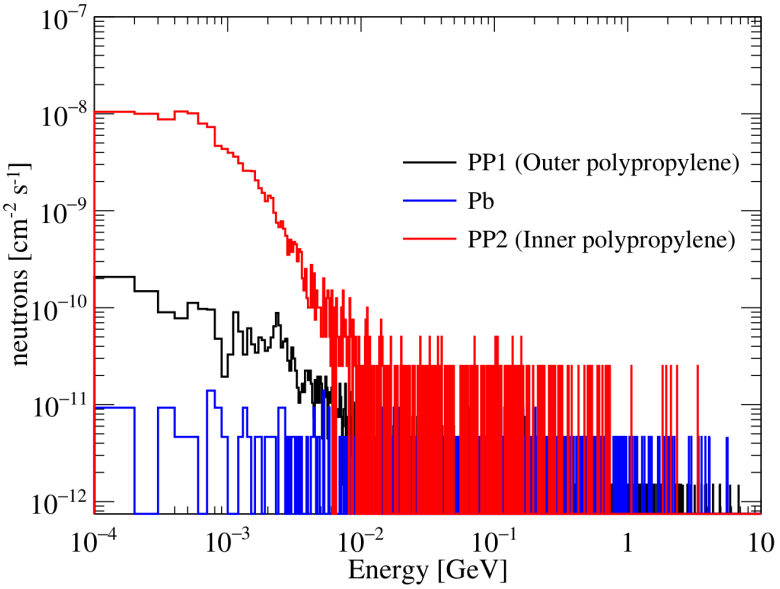

Figure 5.21: Comparison of energy dependence of neutron current (energy bin-width = 100 keV) at surfaces of different layers of the experimental setup [5].

The increase in neutron current at the boundary of PP2 is due to the production of new neutrons in the Pb layer. The increase in the mean energy of neutrons at the Cu layer can

Material	$E^{\text{mean}}_{\text{neutron}}$ (MeV)	Current ($\text{cm}^{-2}\,\text{s}^{-1}$)
PP1	81	$8.19(\pm0.11) \times 10^{-9}$
Pb	280	$3.04(\pm0.12) \times 10^{-9}$
PP2	8	$1.44(\pm0.02) \times 10^{-7}$
Cu	19	$7.44(\pm3.72) \times 10^{-8}$
CsI	9	$6.15(\pm4.35) \times 10^{-8}$

Table 5.5: The mean energy (second column) and current (third column) of neutrons at the top surface of each layer (first column) [5]. Uncertainties shown are statistical only.

be due to the absorption of lower energy neutrons by PP2. The mean scattering length of neutrons is smaller in hydrogen compared to other materials like C, Pb, or Fe for neutron energies less than ~10 MeV. Whereas for higher neutron energies, the mean scattering length increases compared to other materials [27]. Hence, the higher energy neutrons cannot be moderated easily using hydrogen-based shielding material.

5.5 Sensitivity estimates

The dark matter search at JUSL will be through the direct detection of WIMP interactions with detector nuclei [28]. The sensitivity of the experiment is estimated for the neutron background present at Jaduguda lab where it is assumed that neutron-induced events are indistinguishable from WIMP events. For the sensitivity calculation, the formalism suggested in Ref. [29], and used in KIMS [30] DM search is used.

5.5.1 Mathematical framework

The sensitivity is calculated as the 90 % confidence upper limit [31] on the interaction cross-section of dark matter with the detector nucleus. However, experiments do not directly measure the cross-section; they measure the rate of events, which is proportional to the cross-section, in the detector. The upper limit on the WIMP event rate at different

mass gives a corresponding limit on the cross-section.

Considering a dark matter halo model with a Maxwellian velocity distribution as described in Ref. [29], the total WIMP event-rate in the recoil energy range between E_{R_1} and E_{R_2} is given by [30]

$$\begin{aligned} R(v_E, v_{\rm esc}) &= \frac{k_0}{k_1}\int_{E_{R_1}}^{E_{R_2}} dE_R \left\{ c_1 \frac{R_0}{E_0 r} e^{-c_2 E_R/E_0 r} - \frac{R_0}{E_0 r} e^{-v_{\rm esc}^2/v_0^2} \right\}, \\ R_0 &= 5.47 \left(\frac{\mathrm{GeV}/c^2}{m_\chi}\right)\left(\frac{\mathrm{GeV}/c^2}{m_t}\right)\left(\frac{\sigma_0}{\mathrm{pb}}\right)\left(\frac{\rho_\chi}{\mathrm{GeV}/c^2/\mathrm{cm}^3}\right)\left(\frac{v_0}{\mathrm{km/s}}\right), \\ E_0 &= \frac{1}{2} m_\chi v_0^2, \quad r = \frac{4 m_\chi m_t}{(m_\chi + m_t)^2}, \end{aligned} \tag{5.3}$$

where m_χ is the dark matter mass, m_t is the mass of a target nucleus, $\rho_\chi = 0.3$ GeV cm^{-3} is the local dark matter density, $v_0 = 220$ km s^{-1} is the Maxwell velocity parameter in WIMP kinetic-energy $E_0 = \frac{1}{2} m_\chi v_0^2$, $v_{\rm esc} = 650$ km s^{-1} is the local galactic escape velocity of WIMP, $k_0/k_1 \approx 1$ and c_1, c_2 are constants which depend on the Earth (target) velocity v_E, relative to the dark matter distribution as discussed in Ref. [29]. σ_0 is the WIMP-nucleus 'zero momentum transfer' cross-section, and R_0 is the total event rate (in kg^{-1}day^{-1}) for $v_E = 0$, and $v_{\rm esc} = \infty$. Experiments report limit on WIMP-nucleon cross-section which is related to σ_0 by the following formula.

$$\sigma_{W-n} = \sigma_0 \frac{\mu_n^2}{\mu_A^2} \frac{C_n}{C_A}, \tag{5.4}$$

where $\mu_{n,A}$ are the reduced masses of WIMP-nucleon and WIMP-target nucleus of mass number A, and $C_A/C_n = A^2$. If the detector consists of multiple nuclei (e.g CsI), the WIMP-nucleon cross-section for the invidual nuclei are combined together. For a CsI detector, this is given by the following expression.

$$\frac{1}{\sigma} = \frac{1}{\sigma_{Cs}} + \frac{1}{\sigma_I}, \tag{5.5}$$

where σ_{Cs} and σ_I are the WIMP-nucleon cross-section for Cs and I respectively.

5.5.2 Results

The total number of nuclear recoil events due to neutrons within the energy range 8 – 60 keV in the CsI crystal is estimated to be ~6 $kg^{-1}year^{-1}$ (corresponds to a 90% Poisson CL of 12 $kg^{-1}year^{-1}$) from the simulation. The events are from the interactions of cosmogenic neutrons in the detector as radiogenic neutrons are completely stopped by the shielding (see Section 5.4.1). The nuclear recoil energy scale is converted into the electron equivalent energy scale using the quenching factors for CsI crystals reported in Ref. [32]; this turns out to be ~1.5 to 6.5 keV.

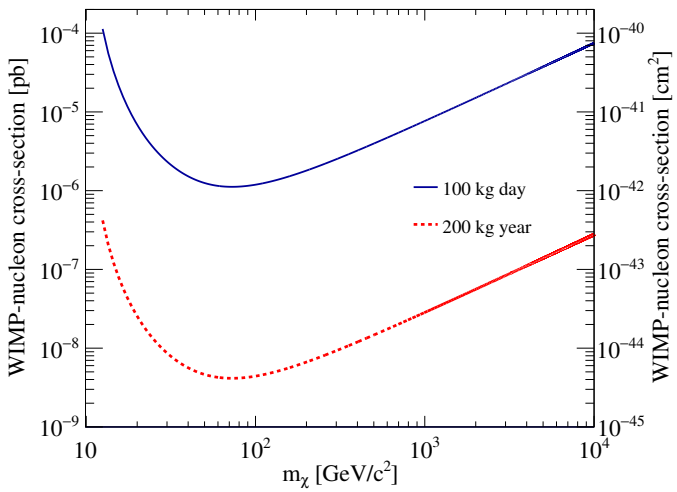

Figure 5.22: Sensitivity of a CsI based detector at JUSL [5]. Blue line shows the sensitivity for a 100 kg day exposure (272 g detector for 1 year) and the red line shows the sensitivity for 200 kg year exposure (200 kg detector for 1 year).

The estimated sensitivity of a CsI based direct dark matter search experiment at JUSL, neglecting the background contribution from gamma and α particles, is shown in Figure 5.22. The blue line in the figure corresponds to the sensitivity with a 272 g detector running for 1 year and the red dotted line corresponds to a 200 kg detector running for 1 year assuming the same level of background in both cases. Sensitivity estimates in the

present study only assume background events from neutrons; this leads to an optimistic estimate of the sensitivity. A more realistic calculation will require consideration of other backgrounds, which are not calculated in this study, along with neutrons. The parameters such as the quenching factors etc. have been assumed to be similar to that of KIMS. A better estimate of the sensitivity will be obtained if all the detector parameters are measured and understood specifically for DINO. Setting up a direct dark matter search experiment at JUSL could be feasible.

5.6 Conclusion

The neutron flux of cosmogenic and radiogenic origin is estimated at Jaduguda for a proposed dark matter search experiment in India. A study has also been performed to find the optimal shielding combination for the effective reduction of these neutron backgrounds. This is followed by an estimation of the sensitivity of a CsI based dark matter search experiment with a typical shielding setup and under the assumption of a neutron only background.

The radiogenic neutrons are produced from (α, n) reactions and spontaneous fission. The neutron yield due to (α, n) reactions from the surrounding rock materials has been obtained as $6.77 \pm 1.12\,\mathrm{yr}^{-1}\,\mathrm{g}^{-1}$ of rock from the ^{238}U decay chain and $5.33 \pm 0.90\,\mathrm{yr}^{-1}\,\mathrm{g}^{-1}$ of rock from the ^{232}Th decay chain [5]. The yield due to spontaneous fission of ^{238}U is obtained as $3.43 \pm 0.52\,\mathrm{yr}^{-1}\,\mathrm{g}^{-1}$ [5]; the contribution of neutrons due to spontaneous fission of other heavy isotopes of U and Th are negligible. The flux of radiogenic neutrons reaching the inner cavern is obtained as $1.12(\pm 0.13) \times 10^{-5}\,\mathrm{cm}^{-2}\,\mathrm{s}^{-1}$ above 100 keV energy threshold with a mean energy of 1.34 MeV and $5.75(\pm 0.69) \times 10^{-6}\,\mathrm{cm}^{-2}\,\mathrm{s}^{-1}$ above 1 MeV energy threshold with a mean energy of 2.18 MeV [5].

Cosmic muon events are generated on the surface using Gaisser's parametrization and are made to propagate through the rock material. The muon flux at the outer cavern is found to be nearly $4.49(\pm0.25) \times 10^{-7}$ cm^{-2} s^{-1} with an average energy of about 200 GeV [5]. It is observed that less than 7 % of the generated cosmogenic neutrons pass through the rock thickness above 2 m. The muons reaching the outer cavern, along with the neutrons produced from muon interactions, are propagated through another 2 m thick rock to obtain the muon and muon-induced neutron flux at the cavern. The muon flux at the inner cavern is obtained to be $4.45(\pm0.24)\times10^{-7}$ cm^{-2} s^{-1} [5]. Muon induced neutron flux from rock in the inner cavern is found to be $0.93(\pm0.05) \times 10^{-8}$ cm^{-2}s^{-1} without any energy threshold and $7.25(\pm0.40) \times 10^{-9}$ cm^{-2} s^{-1} above 1 MeV [5]. Our estimated values of neutron and muon fluxes are comparable with calculations for dark matter experiments in the Boulby mine [25]. The measured value of muon flux at the WIPP salt mine which is at a similar depth ($\sim$ 1580 m.w.e) is 4.77×10^{-7} cm^{-2} s^{-1} [26]. Our estimation of muon-induced neutron flux is comparable with their calculation (1.6×10^{-8} cm^{-2} s^{-1}) reported in the same paper.

The total neutron flux (above 1 MeV energy threshold) reaching the Inner cavern/laboratory from both radiogenic and muon induced reactions in rock is found to be $5.76(\pm0.69)\times 10^{-6}$ cm^{-2} s^{-1} mostly dominated by radiogenic neutrons [5]. The effectiveness of different shielding materials has been investigated. Neutrons produced from muon and neutron interaction with the shielding materials, which consists of a Polypropylene layer + a Pb layer + another Polypropylene layer from the outside towards the experimental setup, also contribute to the neutron flux at the detector. A high number of neutrons are produced in Pb.

Radiogenic neutrons are easily stopped by the 40 cm thick polypropylene layer. Cosmogenic neutrons can penetrate the shielding and reach the detector. Moreover, muons

generate neutrons while traversing through the shielding. Muon and neutron fluxes have been estimated at various layers of shielding. Since the neutron production rate is high in Pb, a second layer of polypropylene is needed for effective shielding of these neutrons. Using the CFG-4 shielding configuration, the flux of muon-induced neutron at the detector is found to be $6.15(\pm 4.35) \times 10^{-8}$ cm^{-2} s^{-1} [5]. The CFG-4 configuration is not the best shielding combination and an optimized shielding configuration will be determined by using input from background measurements.

The sensitivity of a CsI based WIMP dark matter search experiment at the Jaduguda mine has been estimated. The neutrons coming from the cavern as well as those generated from within the shielding materials are considered in the calculation. However, other backgrounds such as gammas, electrons, and α-particles are not considered. Also, the background from contamination in the detector materials will have a contribution to the measured recoil energy spectrum in a real experiment but not considered here. Given all these considerations, the sensitivity results are found to be optimistic, but still indicate that a direct WIMP dark matter search experiment could be feasible at JUSL.

Bibliography

[1] A. Kumar, A. M. Vinod Kumar, Abhik Jash, et al. "Invited review: Physics potential of the ICAL detector at the India-based Neutrino Observatory (INO)". *Pramana* 88.5 (2017), 79.

[2] S. Saha. *Detectors and Detection Techniques for Dark Matter Search Experiments*. Conference on Advanced Detectors for Nuclear, High Energy and Astroparticle Physics Experiments (ANDHEAP). 2017.

[3] Ling Han, Brian W. Miller, H. Bradford Barber, et al. "A New Columnar CsI(Tl) Scintillator for iQID detectors". *Proceedings of SPIE–the International Society for Optical Engineering*. 9214, 92140D. 2014.

[4] Mohit Tyagi, Fang Meng, Merry Koschan, et al. "Effect of codoping on scintillation and optical properties of a Ce-doped $Gd_3Ga_3Al_2O_{12}$ scintillator". *Journal of Physics D: Applied Physics* 46.47 (2013), 475302.

[5] S. Banik, V. K. S. Kashyap, S. Ghosh, et al. "Simulation of neutron background for a dark matter search experiment at JUSL". *JINST* 16.06 (2021), P06022.

[6] Mark David Pepin. "Low-Mass Dark Matter Search Results and Radiogenic Backgrounds for the Cryogenic Dark Matter Search". PhD thesis. Minnesota U., 2016.

[7] D'Ann Rebekah Barker. "SuperCDMS Background Models for Low-Mass Dark Matter Searches". PhD thesis. Minnesota U., 2018.

[8] S. Agostinelli, J. Allison, K. Amako, et al. "Geant4 - a simulation toolkit". *Nuclear Instruments and Methods in Physics Research Section A: Accelerators, Spectrometers, Detectors and Associated Equipment* 506.3 (2003), 250 –303.

[9] http://www.slac.stanford.edu/comp/physics/geant4/slac_physics_lists/shielding/physlistdoc.html.

[10] *GEANT4 Physics Reference Manual, Release 10.4*. https://indico.cern.ch/event/679723/contributions/2792554/attachments/1559217/2454299/PhysicsReferenceManual.pdf.

[11] *Jaduguda rock analysis results*. Atomic Minerals Directorate for Exploration and Research, India (Private communication.)

[12] Emilio Segrè. "Spontaneous Fission". *Phys. Rev.* 86 (1 1952), 21–28.

[13] A. H. Jaffey, K. F. Flynn, L. E. Glendenin, et al. "Precision Measurement of Half-Lives and Specific Activities of ^{235}U and ^{238}U". *Phys. Rev. C* 4 (5 1971), 1889–1906.

[14] N. E. Holden. *The Uranium Half-lives: A Critical Review*. National Nuclear Data Center. Brookhaven National Laboratory, 1981.

[15] A. Ghiorso, G. H. Higgins, A. E. Larsh, et al. "Spontaneous Fission of U^{234}, Pu^{236}, Cm^{240}, and Cm^{244}". *Phys. Rev.* 87 (1 1952), 163–164.

[16] G. Audi, O. Bersillon, J. Blachot, et al. "The Nubase evaluation of nuclear and decay properties". *Nuclear Physics A* 729.1 (2003). The 2003 NUBASE and Atomic Mass Evaluations, 3 –128.

[17] D.-M. Mei, C. Zhang, and A. Hime. "Evaluation of (α,n) induced neutrons as a background for dark matter experiments". *Nuclear Instruments and Methods in Physics Research Section A: Accelerators, Spectrometers, Detectors and Associated Equipment* 606.3 (2009). http://neutronyield.usd.edu/, 651 –660.

[18] Joseph A. Formaggio and C.J. Martoff. "BACKGROUNDS TO SENSITIVE EXPERIMENTS UNDERGROUND". *Annual Review of Nuclear and Particle Science* 54.1 (2004), 361–412. eprint: https://doi.org/10.1146/annurev.nucl.54.070103.181248.

[19] B. E. Watt. "Energy Spectrum of Neutrons from Thermal Fission of U^{235}". *Phys. Rev.* 87 (6 1952), 1037–1041.

[20] Jérôme M. Verbeke, Chris Hagmann, and Doug Wright. *Simulation of Neutron and Gamma Ray Emission from Fission and Photofission*. Tech. rep. UCRL-AR-228518. Lawrence Livermore National Laboratory, 2014.

[21] N. Dokania, V. Singh, S. Mathimalar, et al. "Estimation of low energy neutron flux (En$\leqslant$ 15 MeV) in India-based Neutrino Observatory cavern using Monte Carlo techniques". *Journal of Instrumentation* 10.12 (2015), T12005–T12005.

[22] https://www.google.com/intl/en_in/earth/versions/#earth-pro.

[23] Thomas K. Gaisser, Ralph Engel, and Elisa Resconi. *Cosmic Rays and Particle Physics: 2nd Edition*. Cambridge University Press, June 2016.

[24] M. Tanabashi, K. Hagiwara, K. Hikasa, et al. "Review of Particle Physics". *Phys. Rev. D* 98 (3 2018), 030001.

[25] M.J. Carson, J.C. Davies, E. Daw, et al. "Neutron background in large-scale xenon detectors for dark matter searches". *Astroparticle Physics* 21.6 (2004), 667 –687.

[26] E.-I. Esch, T.J Bowles, A. Hime, et al. "The cosmic ray muon flux at WIPP". *Nuclear Instruments and Methods in Physics Research Section A: Accelerators, Spectrometers, Detectors and Associated Equipment* 538.1 (2005), 516 –525.

[27] C. Bungau, B. Camanzi, J. Champer, et al. "Monte Carlo studies of combined shielding and veto techniques for neutron background reduction in underground dark matter experiments based on liquid noble gas targets". *Astroparticle Physics* 23.1 (2005), 97 –115.

[28] Edward Witten. “Dyons of Charge e theta/2 pi”. *Phys. Lett. B* 86 (1979), 283–287.

[29] J.D. Lewin and P.F. Smith. “Review of mathematics, numerical factors, and corrections for dark matter experiments based on elastic nuclear recoil”. *Astroparticle Physics* 6.1 (1996), 87 –112.

[30] H.S. Lee, H. Bhang, J.H. Choi, et al. “First limit on WIMP cross section with low background CsI(Tl) crystal detector”. *Physics Letters B* 633.2 (2006), 201 –208.

[31] M. Tanabashi et al. “Review of Particle Physics”. *Phys. Rev. D* 98.3 (2018), 030001.

[32] H. Park, D.H. Choi, J.M. Choi, et al. “Neutron beam test of CsI crystal for dark matter search”. *Nuclear Instruments and Methods in Physics Research Section A: Accelerators, Spectrometers, Detectors and Associated Equipment* 491.3 (2002), 460 –469.

Chapter 6

Conclusion

The thesis consists of two major topics: a) search for Lightly Ionizing Particles (LIPs) in SuperCDMS, and b) simulation of neutron backgrounds for a proposed dark matter search experiment at Jaduguda Underground Science Laboratory (JUSL).

LIPs are fractionally charged particles and they lose energy at a rate that is much slower than any known minimum ionizing particles such as the cosmic muons. Since these particles leave only a tiny amount of energy ($\langle \mathrm{d}E/\mathrm{d}x \rangle \sim 1\,\mathrm{eV\,g^{-1}cm^2}$ for minimum-ionizing LIPs with charge $e/1000$) as they pass through a detector, the experiments that can measure very small energy depositions are sensitive to LIPs search. The CDMSlite mode of operating SuperCDMS detectors provides the experiment a sensitivity to search for LIPs with very small fractional charges. The data taken in CDMSlite mode during February through July 2014 is used in the LIP-search analysis. In the analysis presented in this thesis, cosmogenic LIPs with charges below $e/100$, masses between $5\,\mathrm{MeV}/c^2$ and $100\,\mathrm{TeV}/c^2$, and incident $\beta\gamma$ between 0.1 and 10^6 are explored.

A framework within the GEANT4 simulation setup is developed in this thesis to perform simulations of LIPs for any experimental geometry and typical detector materials. The

GEANT4 simulation package is widely used in many experiments starting from low energy nuclear physics to high energy particle physics experiments, but the package traditionally does not come with definitions of fractionally charged particles. The work presented in this thesis provides definitions of positively and negatively charged LIP in a GEANT4 simulation setup. A set of physics processes and models encapsulated in a "physics list" are validated. The list includes two sets of ionization models as IonizationA and IonizationB, and models for bremsstrahlung and pair-production energy losses. The "Barkas effect" that differentiates between a positively and negatively charged particle via stopping-power measurements at small velocities ($\beta\gamma < 0.1$) is included in the IonizationA model. IonizationB, on the other hand, produces atomic shell peaks in the distributions of energy deposition. The atomic shell peaks are important features expected in the energy-deposition distributions of LIPs with small fractional charges and the peaks get smeared by many interactions in the detector for large charges or small velocities of LIPs. Consequently, IonizationB model developed in this thesis work can be used for small fractional charges whereas both IonizationA and IonizationB are suitable for large fractional charges or small velocities of LIPs. The framework developed in this thesis thus provides a useful tool to perform simulation of energy loss in any experimental geometry, and for range of detector materials with choices for processes and models. The simulation framework is made publicly available on `GitHub` to use it in any experiment. There is also plan to include this in the official GEANT4 toolkit for it to be released with the GEANT4 package in the future.

The upper limits on intensity of LIPs are calculated with the data taken in CDMSlite, where energy depositions in the detector between 0.1 and 2.0 keV_{ee} are considered. The limit calculation uses signal energy-deposition distributions calculated with the simulation framework developed in the thesis. A large region of the parameter space of LIPs is excluded in the analysis. The analysis sets the strongest limits on LIPs with charges $\leq e/160$ as

well as the minimum intensity of $1.36 \times 10^{-7}\text{cm}^{-2}\text{s}^{-1}\text{sr}^{-1}$ at charge $e/160$. This analysis is also the first to compute intensity limits for charges smaller than $e/(3 \times 10^5)$. The limits are independent of mass for the range of masses (5 MeV/c^2–100 TeV/c^2) considered. The constraints set in the analysis are the first to cover a wide range of velocities of LIPs in terms of $\beta\gamma$ between 0.1 and 10^6. A nonrelativistic FCP has been proposed to explain the annual modulation signal of dark matter observed by the DAMA/LIBRA and CoGeNT detectors. The analysis presented in the thesis is a significant step towards searching for dark matter with fractional charges since the first limit on non-relativistic LIPs with $\beta\gamma$ values as small as 0.1 is computed in the analysis.

The limits calculated in the thesis use the optimum interval method, and consequently, the results are conservative. With a better understanding of backgrounds, and using statistical techniques like the maximum likelihood method, more stringent limits can be calculated as well as the discovery potential can be enhanced in future analyses. In SuperCDMS SNOLAB with detectors of thickness 3.3 cm, as opposed to 2.5 cm thick detectors in Soudan, the sensitivity for LIPs search will be improved. Besides, SNOLAB will have smaller thresholds of energy depositions providing a better sensitivity for small fractional charges.

The second part of the thesis discusses the simulation of neutron backgrounds for a proposed direct-detection dark matter search experiment at JUSL. The feasibility of performing a dark matter search at JUSL is also studied by estimating the sensitivity as a function of dark matter mass using the estimated neutron backgrounds. Neutron backgrounds at Jaduguda could be of radiogenic and cosmogenic origin. Radiogenic neutrons are primarily produced from (α,n) reactions and spontaneous fission, while cosmogenic neutrons are from interactions of cosmic muons with the cavern-rock and shielding materials.

Neutron production in the rock requires determining the composition of rock around JUSL. Rock samples from various places around the laboratory cavern were analyzed for elemental / oxide contents by 1) Radiometric analysis, 2) Wet chemical analysis, and 3) Inductively coupled plasma - optical emission spectroscopy (ICP-OES) analysis. The Jaduguda rock is found to contain 8 ppm of uranium, 16 ppm of thorium along with other major components such as oxygen, silicon, and aluminum with the concentration of 47.8 %, 31.0 %, and 9.6 % respectively. ^{238}U and ^{232}Th isotopes have a long decay series; they undergo many α- and β-decays till the stable isotope of lead is reached. The α-particles created throughout the decay series participate in (α, n) reactions where they interact with light elements in the rock producing neutrons. The neutron yield from (α, n) reactions is calculated using the program developed by D.-M. Mei et al, where the rock composition around JUSL is utilized. The yields for (α, n) reactions in the rock from ^{238}U and ^{232}Th are found to be 6.77 ± 1.12 $\mathrm{yr^{-1}g^{-1}}$ and 5.33 ± 0.90 $\mathrm{yr^{-1}g^{-1}}$ respectively. Neutron yield due to spontaneous fission is obtained using the Watt function. The neutron yield due to spontaneous fission of ^{238}U in the rock is found to be 3.43 ± 0.52 $\mathrm{yr^{-1}g^{-1}}$. The neutrons produced from (α, n) reactions and spontaneous fission are propagated through the rock. Neutrons that are produced a few meters away from the rock-laboratory boundary, do not contribute to the neutron flux in the lab. The neutron transmission decreases with thickness. Above a thickness of 1 m, the number of neutrons that can traverse through the rock is less than 0.5 %. This suggests that the rock layer of 1 m thickness surrounding the laboratory cavern acts as an active material contributing to the radiogenic neutron flux. This thickness is considered in the simulation of radiogenic neutron-flux estimation. The flux of radiogenic neutrons reaching the inner cavern is obtained to be $1.12(\pm 0.13) \times 10^{-5}\,\mathrm{cm^{-2}\,s^{-1}}$ above neutron energy of 100 keV and $5.75(\pm 0.69) \times 10^{-6}\,\mathrm{cm^{-2}\,s^{-1}}$ above 1 MeV energy.

Estimating the cosmogenic neutron flux requires two major inputs to the simulation: a)

the Jaduguda hill-profile, and b) muon energy and angular distributions. The hill profile comprising the information of latitude, longitude, and elevation of the Jaduguda area is obtained using Google Earth Pro. Energy and angular distribution of muons at the hill-surface level is generated using Gaisser's formula. With start-point positions obtained from hill profile and energy and direction information from Gaisser's formula, one can in principle simulate muon trajectories and the produced particles from muon interactions with the rock. However, simulation of all possible trajectories originating from the hill-surface, where most of them are not expected to reach the cavern, is time-consuming and computationally expensive. A simulation strategy is developed using the muon lateral-displacements and maximum traveled distances in the rock to counter this difficulty. The following strategy has been adopted. Muon lateral displacement calculated at different energy of the particle is found to be as high as 30 m; muons with incident directions within a cone having an axis as the line connecting the point of incidence to the center of the cavern and radius 30 m are simulated. Also, from the calculation of maximum distance traveled by muons at different energies, it is found that the muons are required to have at least 300 GeV energy to reach the cavern; muons above this energy are therefore only considered in the simulation. The muon flux at the cavern from the simulation is found to be $4.45\,(\pm 0.24)\times 10^{-7}\mathrm{cm}^{-2}\mathrm{s}^{-1}$. It is also noted from the simulation that only about 7% of neutrons can transmit through a rock of thickness 2 m; neutrons that are produced beyond this thickness do not contribute significantly to the neutron flux at the cavern and are not tracked in the simulation. The cosmogenic neutron flux at the cavern is found to be $0.93\,(\pm 0.05)\times 10^{-8}\mathrm{cm}^{-2}\mathrm{s}^{-1}$. The muon and neutron fluxes estimated at the Jaduguda experimental cavern are found to be comparable with measurements and estimates done at similar depths by other experiments. The muon flux estimated at the JUSL: $4.45\,(\pm 0.24)\times 10^{-7}\mathrm{cm}^{-2}\mathrm{s}^{-1}$, is comparable to the muon flux measured at the WIPP

salt mine (∼1580 m.w.e depth), which is around $4.77 \times 10^{-7} \mathrm{cm}^{-2}\mathrm{s}^{-1}$. The muon-induced neutron flux at JUSL is also comparable to the calculated value of $1.6 \times 10^{-8} \mathrm{cm}^{-2}\mathrm{s}^{-1}$ at the WIPP salt mine.

The total neutron flux (above 1 MeV energy threshold) reaching the laboratory from both radiogenic and muon induced reactions in rock is found to be $5.76\,(\pm 0.69) \times 10^{-6}\,\mathrm{cm}^{-2}\,\mathrm{s}^{-1}$ which is mostly dominated by radiogenic neutrons.

Neutron backgrounds could be moderated/shielded by using shielding layers around the detector. The effectiveness of different shielding combinations is also studied. The shielding layers considered for this purpose are a polypropylene layer, a lead layer, and another polypropylene layer from the outside towards the experimental setup. A 40 cm thick polypropylene layer shields almost all radiogenic neutrons. However, this thickness of polypropylene is not sufficient to stop cosmogenic neutrons; approximately 47 % of the cosmogenic neutrons could be stopped by this layer. After the first polypropylene layer, a lead layer with a thickness of 30 cm to shield gammas and another polypropylene layer with a thickness of 20 cm are used to shield most of the cosmogenic neutrons. However, muons generate neutrons while traversing through the shielding layers. Muon and neutron fluxes are estimated at various layers of the shielding. Since the neutron production rate in lead is high, the second layer of polypropylene is beneficial for the effective shielding of these neutrons. Using the above-mentioned shielding configuration, the flux of muon-induced neutron at the detector is found to be $6.15(\pm 4.35) \times 10^{-8}\ \mathrm{cm}^{-2}\,\mathrm{s}^{-1}$. This shielding configuration can be optimized and improved using input from background measurements in the future. The future optimization of shielding would also include radiogenic neutron yield from contamination in shielding materials.

The sensitivity of a CsI based WIMP dark matter search experiment at the Jaduguda mine has been estimated considering a neutron only background. The sensitivity is esti-

mated as the upper limit on the spin independent WIMP-nucleon interaction cross-section as a function of WIMP mass, in the mass range 10 GeV/c^2–10 TeV/c^2. Neutrons coming from the cavern as well as those generated from within the shielding materials are considered in the calculation. The lowest sensitivity obtained is $\sim 10^{-42}$ cm^2 at the WIMP mass of $\sim$50 GeV/c^2. A more realistic estimation of sensitivity will be performed considering neutrons as well as other backgrounds in the future. The consideration of other backgrounds will lead to less restrictive limits on cross-section. The results in this thesis indicate that a direct WIMP dark matter search experiment could be feasible at JUSL.